Permittivity and Conductivity Imaging in Electrical Capacitance Tomography

Zhang, Maomao

Award date:
2016

Awarding institution:
University of Bath

Permittivity and Conductivity Imaging in Electrical Capacitance Tomography

By

Maomao Zhang

BEng, MSc

The thesis submitted for the degree of

Doctor of Philosophy

in

The Department of
Electronic and Electrical Engineering
University of Bath

December 2015

Signature:…… Date:……

Abstract

Electrical capacitance tomography (ECT) is a technology that images the dielectric permittivity distribution of materials under test. ECT has been used as a tool for process monitoring in particular for two-phase flow measurement. These applications mainly focus on the dielectric samples, whose conductivity is negligibly small. This thesis studies ECT imaging with conductivity considerations. The conductive materials will affect the capacitance measurements and introduce difficulties in the ECT image reconstruction. This thesis presents solutions based on ECT to image material of different values of conductivity in different practical process or monitoring scenarios: the conductivity within materials under test is considered to be higher than $\sigma \approx 10^6$ S/m, or less than 10 S/m. This work consists of the following innovative steps. (i) Through an ECT monitoring, floating (*i.e.*, electrically non-grounded) metallic samples are imaged as dielectric illusions and the analysis of capacitance measurements over the conductors is delivered. (ii) Magnetic induction tomography (MIT) is firstly used for locating grounded metallic samples, thereafter as an assistant method to guide ECT to image the dielectric components. (iii) In low conductivity case MIT, as an indicator of conductive material again, helps ECT to solve multiphase flow problems. (iv) The multi-frequency complex ECT measurement provides a potential method to improve the ECT imaging ability for both conductive and dielectric materials. The first three ideas have been testified by both simulated and experimental results, while the fourth part is simulation-based results only on current stage.

Acknowledgements

Firstly, I would like to express my deepest gratitude to my dear supervisor and kind friend, Dr Manuchehr Soleimani for his invaluable guidance and encouragement. My research life during PhD course would not be colourful and passionate without his expertise and experience. I am sincerely grateful to be one member of his research team, where I was not only strongly linked with many interesting research topics but also work as an independent researcher focusing on my own interest.

Secondly, I am indebted to University of Bath and Chinese Scholarship Council, who jointly provide financial support for my research.

I would like to thank my previous colleague Dr. Lu Ma for sharing her knowledge and advices. I am also thankful to Dr Yaoyuan Xu from Hebei University of Technology and Dr. Thomas Wondrak from HZDR for their assistance on exploring new applications. And I would like to express my sincere appreciation to my dear friends in Bath, including Mr Zhongjian Liu, Dr. Ran Li, Miss Jiangning Gao, Dr. Jingzhe Wu, Dr. Lin Zhou Mr Zhengyu Zhang, Mr Huiming Zhang, Miss Jing Hu and Mr Tony Jones for their support.

In addition, I would also like to thank the SETsquared Partnership, who provide invaluable courses and a journey to innovative my mind. Special thanks to Dr Ali Hadavizadeh for his patient guidance.

Last but not the least, I would like to take this opportunity to express my ultimate gratitude to my parents, thanks for understanding and support my career choice. I am sincerely grateful to my lovely lady, Miss Ying Liu, who gives infinite encouragement and support.

Contents

List of Figures

List of Tables

Chapter 1 Introduction

1.1 Background

Electrical tomography is a technique using electrical measurements at electrodes or coils on the periphery of a target region to visualize the distribution of passive electromagnetic properties within this region. Currently electrical tomography includes three types of techniques: electrical impedance tomography (EIT), magnetic inductance tomography (MIT) and electrical capacitance tomography (ECT).

EIT uses multiple sensor electrodes to contact the sample under test directly, and measure the impedance over each pair of electrodes. After that, the measurements are computed to obtain an image of conductivity change [1]. EIT is the most developed modality with the longest history among these three tomographic techniques. It has medical applications [2-5], such as breast cancer detection [6],lung air and liquid volumes [7, 8], etc. And EIT has been introduced into industrial process engineering [9], for mapping the concentration and velocity distributions multi-phase flows [10-12]. In most applications of EIT, only the real part of impedance measurement is used, *i.e.*, the resistance information, thus the conductivity distribution is reconstructed, and this is called electrical resistance tomography (ERT).

MIT, also known as mutual inductance tomography or electromagnetic induction tomography (EMT), is the most recent and least developed electrical tomography modality. The measurements of MIT are taken on the pairs of coils around the sample, by dropping fixed voltage over one coil and measure the induced voltage on the others. MIT aims to

visualized the distribution of passive electromagnetic properties: permittivity or conductivity [13], but in current stage, most application of MIT is focused on conductivity imaging. MIT has been applied to medical imaging [14-17], in addition, the industrial applications of MIT include non- destructive evaluations (NDE) for pipeline [18], and flow measurement [19, 20].

ECT is a non-invasive and non-intrusive technology that can be used for contactless monitor on industry process or defect detections on pipeline [21-28]. The aim of ECT is to calculate and visualize the unknown permittivity distribution via measuring capacitances between pairs of peripheral electrodes around samples. The samples under test of ECT are normally dielectric or negligibly lowly conductive, since the conductivity affect's the measuring of ECT and leads to the failure of imaging [29, 30]. Current applications of ECT include monitoring two-phase flow, such as gas-solid flows in pneumatic conveyors and gas-oil in oil pipeline [31-33] or the plastic pipeline wall defect detection [21].

Table 1.1: Electrical tomographic techniques.

Techniques	**EIT**	**MIT**	**ECT**
Sensors	Electrodes	Coils	Electrodes
Measurement	Impedance	Inductance	Capacitance
Conductive contact	Yes	No	No
Property to be imaged	σ	σ, ε, μ*	ε

* MIT is able to image all the three passive electromagnetic property, however the current stage of MIT research or applications are generally focusing on conductivity and permeability imaging.

Besides these three types of electrical tomography, a new method called Capacitively Coupled Electrical Resistance Tomography (CCERT) is introduced by Baoliang *et al.* [34-36]. Traditional electrodes of ERT or EIT need to inject electric current to sample under test through a conductive medium, therefore a direct contact on the medium is in need. However, the electrodes in direct contact with liquid may result in corrosion, which will

decrease the measurement accuracy and increase cost in replacing electrodes; to install EIT sensor, the pipe in use has to be drilled or even changed with a new piece of pipe with electrode mounted inside, which will decrease the strength of the pipeline and increase the installation cost. CCERT uses voltage source to measure the impedance between the electrodes on external surface. Without a conductive path, it still can image the conductivity distribution with the complex-value measurement.

1.2 Aim and Objectives

The main objective of the research is to study ECT as a non-invasive and non-destructive imaging technology for multi-phase flows, *i.e*. gas-oil-water. The general application of ECT is to detect the dielectric permittivity change under test. Compared with the successful application of ECT on gas-oil pipeline inspection [33], the water flow normally has conductivity and high permittivity. Before our study, Yi Li *et al*. has done some research on gas-oil-water [37]. They only focused on the permittivity change on the water-in-liquid ratio, but when the oil and water are not well mixed or water in liquid ratio is high, the conductivity of the water will disable the traditional ECT. Therefore, we are going to extend application of ECT to detecting the conductivity change. In our first year study, three main research aims are listed below.

At first the research interest is about imaging a combination of separate highly conductive inclusions and dielectric inclusions, such as the reinforced concrete consisting of conductive rebar and dielectric concrete. At beginning, MIT is introduced to detect the location of the conductors existing in the sensor area. Subsequently, this location information is fed to ECT for improving the forward model. And ECT inspects the permittivity changes in the rest-sensing region excluding conductors identified by MIT.

Secondly we are aiming to study the influence of low conductivity in ECT. In our experiments, saline water is chosen as lowly conductive background and empty bottles or plastic bar is chosen as a non-conductive/dielectric content. Since water has the inherence of high permittivity, the capacitance measurement from the current sensor with large electrodes is saturated. A new sensor with smaller electrodes is built for the following test. In general most forward model of ECT is only based on permittivity for dielectric inspection, which is less computationally prohibitive. In our case, a complex model is built for the conductivity study on ECT.

The third aim is to integrate the ECT and MIT for low conductivity applications. The material with low conductivity is normally the human tissue in medical application or the water in oil pipelines in industry application. Thus a contactless tomography system is going to be built. If the issues about conductivity in ECT test can be solved in our second aim, ECT will collaborate with MIT to solve the problem of both conductivity and permittivity distribution. And finally at least with simulation studies we will investigate how a multi-frequency complex admittance based ECT device might be able to image both electrical conductivity and dielectric permittivity. Although, there are various classes of ECT devices that are able to image conductivity contrast, we are aiming to investigate this in a systematic manner.

1.3 Outlines of Thesis

The chapters of this thesis are organised as below.

Chapter 2 starts to demonstrate ECT and MIT measurement systems. These systems mentioned are used for the following experiments through this thesis. The ECT system is a

commercial product and the two types of MIT system are designed by our research group in the Engineering Tomography Laboratory (ETL) in University of Bath.

Chapter 3 explains the basic mathematical forward model and reconstruction techniques of ECT and the equations of sensitivity matrix of MIT as well. This part is not innovative from the author of this thesis, since most methods has already been well studied in past decades. A clear introduction about the mathematics in electrical tomography problems would help to understand this hard problem.

Chapter 4 is the initial test of ECT on complex material, *i.e.*, both conductive and dielectric. We start from the case of floating conductor in ECT. From an analytical 2-dimensional results, a piece of floating metal behaves as an illusion of high permittivity in capacitance measurement. Then ECT experiments are carried out to prove this idea.

Since the 2-dimensional analytical results in **Chapter 4** imply that the ECT is not able to image the grounded conductor, in **Chapter 5** the grounded conductor in ECT is studied. By introducing MIT, a hybrid solution of this two modality is proposed to solve the severe distortion in electric field by grounded metal. Multiple sets of simulations and experiments are included in this chapter to testify the feasibility.

In **Chapter 6**, application area of dual modality is extended from high conductivity to low conductivity, where the problems always exist in multiphase flow measurement. The problems of three-phase imaging, *i.e.*, water-gas-oil, is divided into two cases: air-background and water-background. The capability of the dual-modality on these two cases are addressed, and a potentially better solution about increasing signal frequency in capacitance measurement is raised at the end of this chapter. And this simulation of capacitance measurements over increasing conductivity leads to the ideas which starts to

focus on the imaging ability of ECT over conductivity.

Chapter 7 presents a simulation study on ECT using complex-value model and measurement. With the complex-value model, ECT has the similar function to image the conductivity distribution as EIT does. The distribution of both conductivity and permittivity can be reconstructed simultaneously. The future capability of complex-value ECT is demonstrated.

Chapter 8 summaries the contribution of the thesis, demonstrates the limitations of current work and discuss the direction of future development.

Chapter 2 ECT and MIT Systems

An ECT system usually consists of three parts as shown in **Figure 2.1(a)**: a sensor made of electrode array, a capacitance measurement unit (CMU) and a reconstruction-computing unit. A MIT system usually consists of 4 parts as shown in **Figure 2.1(b)**: a sensor made of coil array, a switching circuit, data acquisition circuit and a host computer.

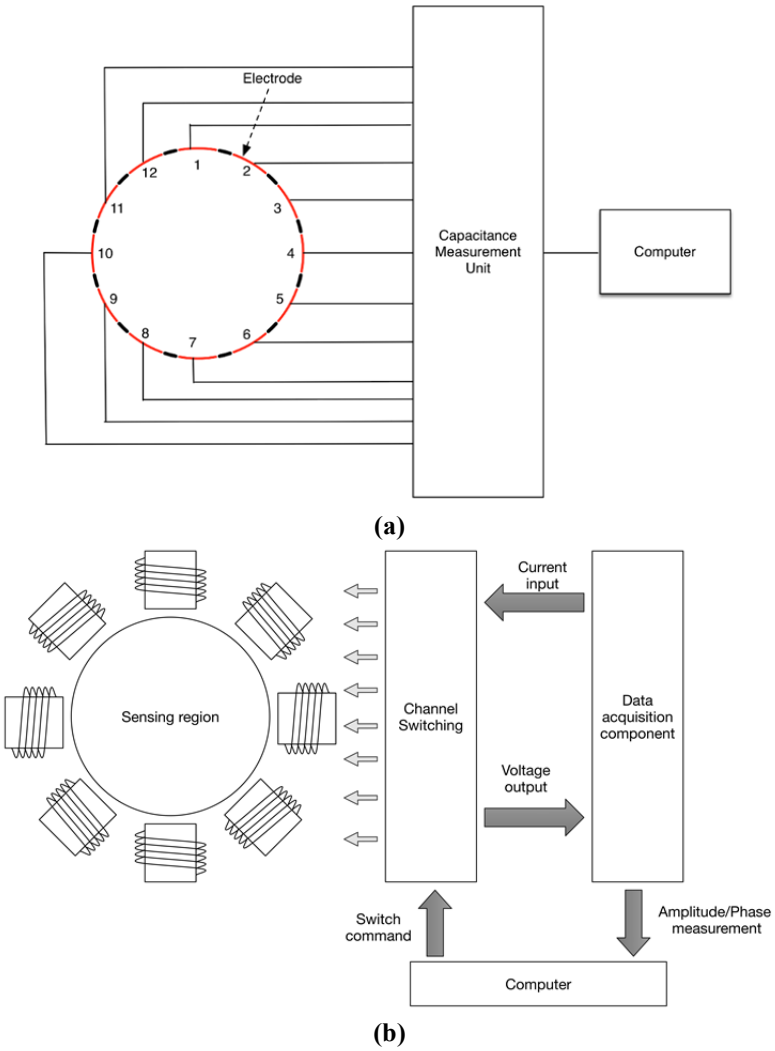

Figure 2.1: Basic modules of **(a)** a 12-electrodes ECT system; **(b)** an 8-coils MIT system.

For ECT, the capacitance measurement unit picks up every pair of electrodes and measures capacitance between them, then transfers data into a computer for image reconstruction. In this chapter, sensors of different structures and a measurement unit will be introduced. The function of a computer in our ECT system is to build the models for forward problem and to complete the algorithms for inverse problem or reconstruction, which will be elaborated in **Chapter 3**. For MIT, to measure the inductance between a pair of coils, the switching circuit choose one of the coils as a transmitter (which injected with alternative current from signal generator) and another coil as a receiver (the induced voltage between whose two terminals is measured by the acquisition circuit). The switching pattern and the measurements are generated and obtained by the computer.

2.1 Capacitance Measurement Unit

Namely, the function of a capacitance measurement unit is to acquire capacitance data from a sensor and transmit the data to a computer in digital form. There are mainly two types of analogue capacitance measurement circuits: AC-based and charge/discharge. The charge/discharge circuit was first introduced by Huang *et al.* [38, 39]. Then the AC-based system is designed and developed by Yang *et al.* [40-43], and this design has the advantage of low cost and wide measurement range. And a digital ECT system has also been designed by Cui *et al*.[44]. The measurement unit in our laboratory is PTL 300E [45], which provides maximum 24 channels for capacitance measurements. The capacitance measurement circuit of this unit is driven by a square wave at 1.2 MHz .This CMU is designed for low permittivity sample, so the effective range of capacitance measurement is from 0.1 fF to 2.0 pF. For a high permittivity sample, such as water ($\varepsilon_r = 80$), this system would saturates due to the upper limit of measurement.

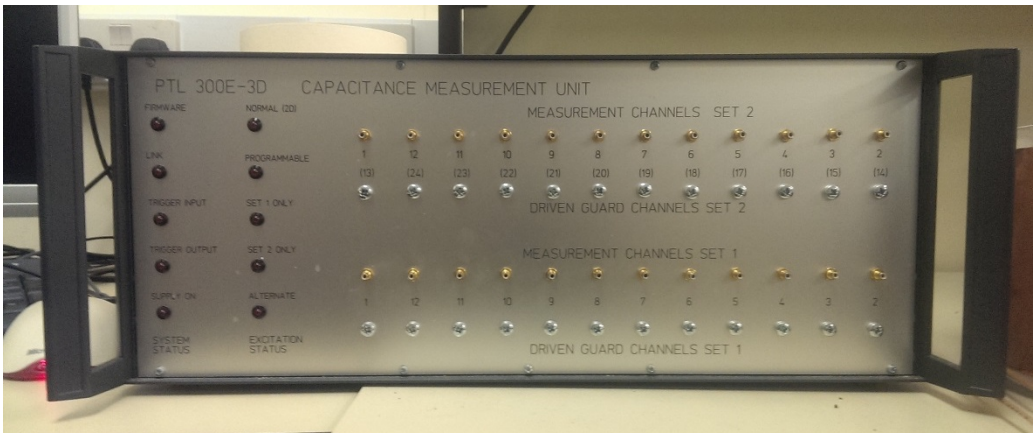

Figure 2.2: PTL 300E capacitance measurement unit in our laboratory.

During capacitance metering, only one of the electrodes is powered by exciting voltage while the rest of the electrodes are set to zero volts. So for a 6-electrode sensor, the frames of capacitance measurement are listed as below. The number means the serial number of each electrode. The first line indicates that only the electrode 1 is excited and the capacitance is measured between 1 and the rest. The following lines represents that each electrode is energized sequentially.

1-2, 1-3, 1-4, 1-5, 1-6

2-3, 2-4, 2-5, 2-6

3-4, 3-5, 3-6

4-5, 4-6

5-6

All of the capacitance measurement is shown in a webpage on the computer connected to

the CMU. Then the data of the webpage will be acquired by Matlab for following reconstructions.

2.2 MIT Measurement System

MK-I and MK-II MIT measurement systems are classified as amplitude-based measurement and phase difference measurement [13] for highly conductive materials ($\sigma > 10^4$ S/m and lowly conductive samples ($\sigma < 10$ S/m) respectively.

The MK-I system consists of a digital function generator, an ADG406 multiplexer, and a NI6295 data acquisition, the detailed design can be found in [46, 47]. This system is designed for the non-destructive evaluation (NDE), where eddy current in highly conductive material causes high induced magnetic fields and the amplitude of the voltage over a coil of receiver is measured. The applications in **Chapter 5** is based on this system.

For low conductivity samples, where the amplitude of measurable voltage over the receiving coil is very small. The MK-II system is designed for the phase change between the transmitting input and the receiving output. It consists of a fully differential amplifier THS4500 for coils of the transmitter, a low-noise, high-speed amplifier THS4275 for coils of the receivers, and three National Instrument based sub-devices for data acquisition, which are a NI5781 for the signal generation, a NI2953 for the multi-channel switching process and a NI7951 FlexRIO board for accelerating the data acquisition process [48, 49]. The applications in **Chapter 6** is based on this system

2.3 Summary

Both ECT and MIT systems capture the multiple electrical measurements between each pair of terminals (*i.e.*, electrodes for ECT or coils for MIT) in turn and transfer the data to the host PC for analysis and reconstruction. The nature of these measurements is the impedance or admittance between each pair of terminals, this leads to an impedance analyser based measurement system for general applications of either ECT or MIT could be designed.

Chapter 3 Models and Algorithms

For ECT, both the forward and inverse problems must be solved to obtain an image of permittivity distribution.

In the forward problem, the finite element method (FEM) is implemented. The geometry and boundary conditions are set up for FEM to generate the distribution of electric potential. Then the relationship between measurements change and permittivity change distribution is generated, which is called Sensitivity Matrix. In the inverse problem, due to the singularity of the sensitivity matrix, the inverse matrix does not exist. Therefore many kinds of algorithms are used to reach an approximation of the inverse matrix for sensitivity matrix. Then the tomogram will be reconstructed.

3.1 Forward Problem

In the forward problem, the potential distribution and electric charges at the electrodes can be found with the assistance of the known permittivity distribution and measurement signal (the voltage of the excited electrode). In ECT, the samples in sensing area, including the medium between the samples and the sensor, are essentially non-conductive: existence of conductive elements can be negligible ($\sigma(x, y) \approx 0$).

From Maxwell's equations [50], the relationship between electrical field $E(x, y)$and electric potential $u(x, y)$ are in the following way within the region of $x \in \Omega \subset \mathbb{R}^3$, where Ω is the whole imaging domain.

$$\boldsymbol{E}(x,y) = -\nabla u(x,y) \tag{3.1}$$

where ∇ is the gradient operator. Since no free charges exist inside the domain, the divergence of electric displacement field is zero (Gauss' Law):

$$\nabla \cdot \boldsymbol{D}(x,y) = 0 \tag{3.2}$$

Combining the equation **(3.1)** and $\boldsymbol{D}(x,y) = \varepsilon(x,y)\boldsymbol{E}(x,y)$, the equation **(3.2)** can be expressed as:

$$\nabla \cdot \varepsilon(x,y)\nabla u(x,y) = 0 \tag{3.3}$$

The boundaries of the whole ECT sensor can be divided in to several components:

Symbols	Denotations
$\boldsymbol{\partial\Omega}$	**The boundaries of domain**
$\boldsymbol{\partial\Omega_{shield}}$	**The electrically grounded shield**
$\boldsymbol{e_l}$	**The surface of *l*th electrod**
$\boldsymbol{e_{ex}}$	**The surface of excited electrode**

Therefore the boundary conditions for equation **(3.3)** are set as:

$$u(x,y) = 0 \qquad x,y \in \partial\Omega_{shield} \bigcup_{l=1}^{N_e} e_l \backslash e_{ex} \tag{3.4}$$

$$u(x,y) = V \qquad x,y \in e_{ex} \tag{3.5}$$

$$\varepsilon(x,y)\frac{\partial u(x,y)}{\partial \boldsymbol{v}} = 0 \qquad x,y \in \partial\Omega \backslash \left\{\partial\Omega_{shield} \bigcup_{l=1}^{N_e} e_l\right\} \tag{3.6}$$

The equation **(3.4)** indicates that the potential on the unexcited electrodes and electrically grounded shield is zero. The equation **(3.5)** is valid at the surface of excitation boundary. On the surface of a boundary, $\nabla u(x,y)$ can be written as $\partial u(x,y)/\partial \boldsymbol{v}$, which is derivative of the electrical potential in the direction of the unit normal vector $\boldsymbol{v}$ away from the electrode surface. The equation **(3.6)** shows the non-conductive boundaries with no fixed voltage, and the electric displacement field is zero at the direction of the unit vertical vector of the boundaries.

From the Gauss's law of electric displacement field, the relationship between the total electrical charges q_l on the lth electrode is expressed as:

$$q_l = \int_{e_l} \boldsymbol{D}(x,y) \cdot d\boldsymbol{S} \tag{3.7}$$

The derivative form of electrical potential in equation **(3.3**) is applied in the equation **(3.7)** as:

$$q_l = -\int_{e_l} \varepsilon(x,y)\nabla u(x,y)\, d\boldsymbol{S} = -\int_{e_l} \varepsilon(x,y)\frac{\partial u(x,y)}{\partial \boldsymbol{v}} dS \qquad \textbf{(3.8)}$$

For the computer based algorithms, the continuous and nonlinear inherence of distribution of electrical potential and permittivity is solved with the help of the finite element method (FEM). In our ECT forward modelling we use a piecewise constant permittivity. The permittivity and electric field is constant within each element (pixel).

The shape function $\phi_i(x,y)$ would be used to discretize permittivity distribution:

$$u(x,y) \approx u_1 \cdot \phi_1(x,y) + u_2 \cdot \phi_2(x,y) + \cdots + u_n \cdot \phi_n(x,y) \qquad \textbf{(3.9)}$$

$$u(x,y) \approx \sum_{i=1}^{N} u_i \varphi_i(x,y) \qquad \textbf{(3.10)}$$

where N is the number of discretized nodes. Above shows a smooth varying permittivity for each element [51]. Therefore the equation q_l is expressed as the distribution of the discretized permittivity.

$$q_l(\varepsilon) = q_l(\varepsilon_1, \varepsilon_2, \cdots \varepsilon_n) \qquad \textbf{(3.11)}$$

The FEM is about to solve the equation below:

$$Au = B \tag{3.12}$$

where A is the stiffness matrix or FEM matrix, u is the solution of voltage potential distribution and B is a matrix that contains boundary conditions.

The potential distribution is obtained. In the cases that the sensor is fully filled with air and the wooden bar stands in the centre of sensing area, the potential distribution difference is indicated in below.

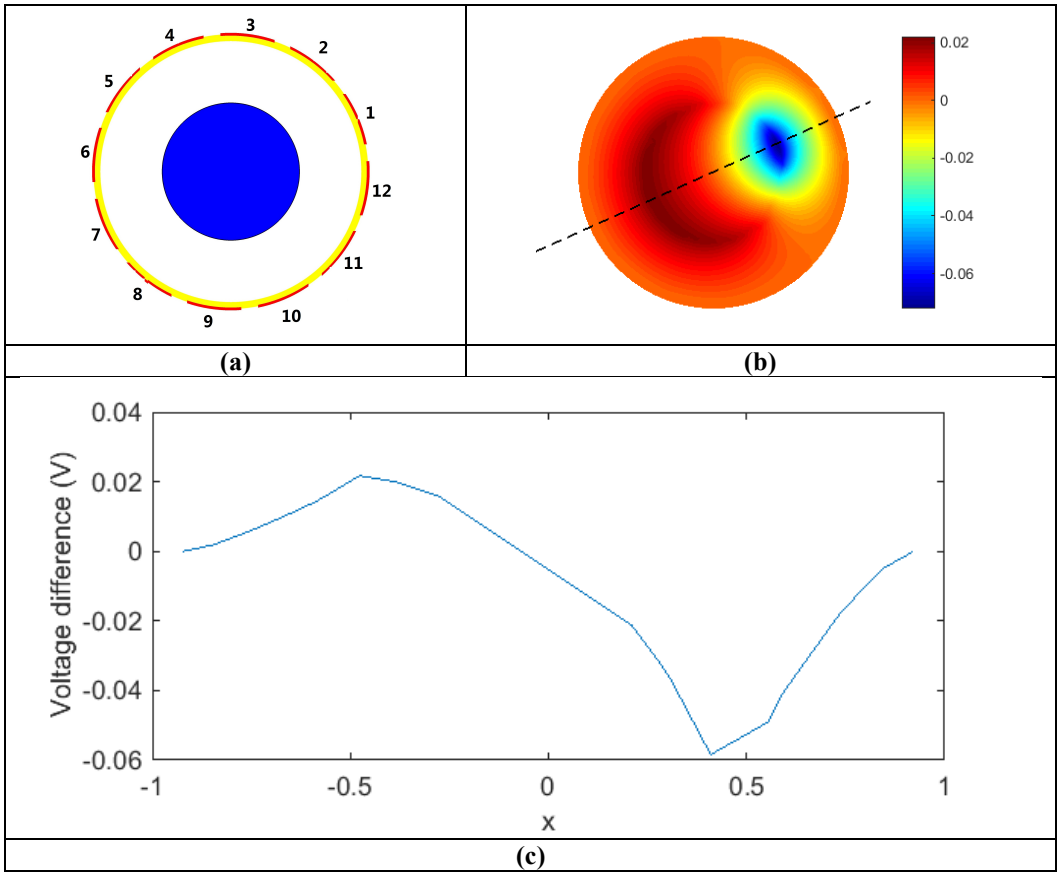

Figure 3.1: (a) a wooden round bar in centre; **(b)** The difference in potential distributions between air and a wooden bar, when an electrode (number 1) is excited.; **(c)** The potential difference plot in one dimension along the dashed line in figure 3.1(b).

The curve in **Figure 3.1(c)** shows that voltage difference changes on various speed along the dashed line. The distortion happens in electrical field when introduce an inclusion of difference permittivity into the sensing region. And this is also soft-field feature of ECT.

3.2 Inverse Problem

The permittivity distribution will be solved in the inverse problem. The difference imaging is used to solve the nonlinear problem [52]. At a linearization point, $\varepsilon_{lin} = \begin{bmatrix} \varepsilon_1^{lin} \\ \varepsilon_2^{lin} \\ \varepsilon_3^{lin} \\ \vdots \\ \varepsilon_n^{lin} \end{bmatrix}$, the Taylor series expansion is implemented to the equation **(3.11)**.

$$q_l(\varepsilon) = q_l\left(\varepsilon_1^{lin}, \varepsilon_2^{lin}, \varepsilon_3^{lin} \cdots \varepsilon_n^{lin}\right)$$

$$\text{(First order)} \quad + \frac{\partial q_l(\varepsilon)}{\partial \varepsilon_1}\left(\varepsilon_1 - \varepsilon_1^{lin}\right) + \frac{\partial q_l(\varepsilon)}{\partial \varepsilon_2}\left(\varepsilon_2 - \varepsilon_2^{lin}\right) + \cdots + \frac{\partial q_l(\varepsilon)}{\partial \varepsilon_n}\left(\varepsilon_n - \varepsilon_n^{lin}\right)$$

$$\text{(Second order)} \quad + \frac{1}{2!}\sum_{i=1}^{n}\sum_{j=1}^{n}\frac{\partial^2 q_l(\varepsilon)}{\partial \varepsilon_i \partial \varepsilon_j}\left(\varepsilon_i - \varepsilon_i^{lin}\right)\left(\varepsilon_j - \varepsilon_j^{lin}\right)$$

$$\text{(To infinite order)} \quad + \cdots\cdots\cdots \qquad \textbf{(3.13)}$$

By omitting the higher order of derivatives, the equation is rewritten as:

$$q_l(\varepsilon) \approx \quad q_l\left(\varepsilon_1^{lin}, \varepsilon_2^{lin}, \varepsilon_3^{lin} \cdots \varepsilon_n^{lin}\right) + \frac{\partial q_l(\varepsilon)}{\partial \varepsilon_1}\left(\varepsilon_1 - \varepsilon_1^{lin}\right) + \frac{\partial q_l(\varepsilon)}{\partial \varepsilon_2}\left(\varepsilon_2 - \varepsilon_2^{lin}\right) + \cdots$$

$$+ \frac{\partial q_l(\varepsilon)}{\partial \varepsilon_n}\left(\varepsilon_n - \varepsilon_n^{lin}\right) \tag{3.14}$$

Therefore, for the lth measurement, the change in charges on the specified electrode can be written as:

$$q_l(\varepsilon) - q_l\left(\varepsilon^{lin}\right) = \begin{bmatrix} \frac{\partial q_l(\varepsilon)}{\partial \varepsilon_1} & \frac{\partial q_l(\varepsilon)}{\partial \varepsilon_2} & \cdots & \frac{\partial q_l(\varepsilon)}{\partial \varepsilon_n} \end{bmatrix}_{1*n} * \begin{bmatrix} \varepsilon_1 - \varepsilon_1^{lin} \\ \varepsilon_2 - \varepsilon_2^{lin} \\ \vdots \\ \varepsilon_n - \varepsilon_n^{lin} \end{bmatrix}_{n*1} \tag{3.15}$$

Set the charge difference as $\Delta q_l = q_l(\varepsilon) - q_l\left(\varepsilon^{lin}\right)$, and apply this equation to all m measurements, the Jacobian matrix or sensitivity map can be generated as:

$$\begin{bmatrix} \Delta q_1 \\ \Delta q_2 \\ \vdots \\ \Delta q_m \end{bmatrix}_{m*1} = \begin{bmatrix} \frac{\partial q_1(\varepsilon)}{\partial \varepsilon_1} & \frac{\partial q_1(\varepsilon)}{\partial \varepsilon_2} & \cdots & \frac{\partial q_1(\varepsilon)}{\partial \varepsilon_n} \\ \frac{\partial q_2(\varepsilon)}{\partial \varepsilon_1} & \vdots & \vdots & \frac{\partial q_l(\varepsilon)}{\partial \varepsilon_n} \\ \vdots & \vdots & \vdots & \vdots \\ \frac{\partial q_m(\varepsilon)}{\partial \varepsilon_1} & \frac{\partial q_m(\varepsilon)}{\partial \varepsilon_2} & \cdots & \frac{\partial q_m(\varepsilon)}{\partial \varepsilon_n} \end{bmatrix}_{m*n} * \begin{bmatrix} \varepsilon_1 - \varepsilon_1^{lin} \\ \varepsilon_2 - \varepsilon_2^{lin} \\ \vdots \\ \varepsilon_n - \varepsilon_n^{lin} \end{bmatrix}_{n*1} \tag{3.16}$$

The $m * n$ matrix in the equation **(3.16)**, is the Jacobian matrix. The capacitance measurement $C = \frac{Q}{V}$ is proportional to the charge, therefore the equation can be rewritten

as [53]:

$$\begin{bmatrix} \Delta C_{11} \\ \vdots \\ \Delta C_{m1} \end{bmatrix} = \begin{bmatrix} s_{11} & \cdots & s_{1n} \\ \vdots & & \vdots \\ s_{m1} & \cdots & s_{mn} \end{bmatrix} \times \begin{bmatrix} \Delta \varepsilon_{11} \\ \vdots \\ \Delta \varepsilon_{n1} \end{bmatrix} \quad \textbf{(3.17)}$$

where $s_{ij} = \frac{\partial C_i}{\partial \varepsilon_j}$, a normalised form of equation is commonly used [22]:

$$\Delta C = S\Delta\varepsilon \quad \textbf{(3.18)}$$

where ΔC is the vector of the change in capacitance measurements; S is the Jacobian matrix of capacitance change with respect to normalised permittivity, *i.e*. the transducer sensitivity, and $\Delta\varepsilon$ is the vector of permittivity distribution change [54, 55].

The sensitivity map can be calculated using an efficient formulation based on calculated fields from excitation and sensing electrodes [51, 55].

$$\frac{\partial C_{pq}}{\partial \mathcal{E}} = -\int_{\Omega} \nabla u_p \cdot \nabla u_q dS \quad \textbf{(3.19)}$$

where u_p and u_q are potential over region Ω when electrodes p and electrode q are excitation electrodes respectively.

The sensitivity map, S, is the connection between the change of the measurement and the change of electrical passive parameters (μ, σ and ε), so the reconstruction is based on this

map. This sensitivity equation has been studied in [56, 57], and it is generated from the equation below for both two tomograms.

$$\int_{\Gamma} \delta \boldsymbol{E}_1 \times \boldsymbol{H}_2 \cdot \boldsymbol{n}\, d\,\Gamma = \int_{\Omega} \left[-i\omega\delta\mu \boldsymbol{H}_1 \cdot \boldsymbol{H}_2 + (\delta\sigma + i\omega\delta\varepsilon)\boldsymbol{E}_1 \cdot \boldsymbol{E}_2\right] d\Omega \qquad \textbf{(3.20)}$$

Equation **(3.20)** provides a general form of sensitivity analysis that applies to ERT, ECT and MIT where $\boldsymbol{E}_1$ and $\boldsymbol{H}_1$ are electric and magnetic field with excitation number 1 (electrode or coil) and $\boldsymbol{E}_2$ and $\boldsymbol{H}_2$ are electric and magnetic field with excitation number 2 (electrode or coil). This formulation allows a change in boundary data (surface components and their surface integrals) to a change in material properties approximated by the volume integral of internal fields.

To solve the forward problem of MIT, finding the magnetic vector potential A is the key. There are many FEM based formulations can be used to solve the A field, such as (**A**, **A-V**) and (**A**, **A**) formulation. In this study, we adopted a (A, A) formulation using edge based FEM [58, 59].

$$\nabla \times \left(\left(\frac{1}{\mu} \right) \nabla \times \boldsymbol{A} \right) + j\omega\sigma \boldsymbol{A} = \boldsymbol{J}_s \qquad \textbf{(3.21)}$$

where σ is conductivity, ω is angular frequency of the excitation current, μ is permeability, and current density J_s can be prescribed by magnetic vector potential from the Biot-Savart Law. If the total current in the excitation coil was I_0 the sensitivity of the induced voltage to the conductivity change can be written as:

$$\frac{\partial V_{mn}}{\partial \sigma_k} = -\omega^2 \frac{\int_{\Omega_k} \boldsymbol{A}_m \cdot \boldsymbol{A}_n dv}{I_0} \quad \textbf{(3.22)}$$

where V_{mn} is the measured voltage, σ_k is the conductivity of pixel k, Ω_k is the volume of the perturbation (pixel k), $\boldsymbol{A}_m$ and $\boldsymbol{A}_n$ are respectively solutions of the forward problem when excitation coil (m) is excited by I_0 and sensing coil (n) is excited with unit current.

The solution is not unique, because the number of m, the number of capacitance measurement, is usually much smaller compared with the number of n, the number of pixels [60]. Therefore the inverse matrix of sensitivity map does not exist. To solve the problems of ECT or MIT reconstruction, many algorithms have been used to approach the real permittivity distribution. And these algorithms can be concluded into two categories: Non-iterative algorithms and Iterative algorithms.

3.2.1 Non-iterative Algorithms

3.2.1.1 Linear Back-Projection (LBP)

From equation **(3.18)** the permittivity distribution g can be found easily:

$$\Delta\varepsilon = S^{-1}\Delta C \quad \textbf{(3.23)}$$

Usually there is no direct inverse matrix of S, due to inequality between the number of capacitance measurements and the number of pixels. Therefore the result of permittivity cannot be deduced from equation **(3.23)** directly. Linear back-projection is introduced by

Xie *et al*. to reach an approximation solution [22]

$$\Delta\hat{\varepsilon} = S^T \Delta C \tag{3.24}$$

where, to some extent, S^T represents an inverse role of S, and generated $\Delta\hat{\varepsilon}$ provides an estimation for $\Delta\varepsilon$. Mathematically, the LBP algorithm is not accurate to provide a solution for the ill-posed problem, but a qualitative result can be yielded to obtain general view about the permittivity distribution. With the advantages of fast process and simplicity, the LBP algorithm is still widely used. If quantitative information is desired, the following algorithms should be used.

3.2.1.2 Tikhonov Regularization

Tikhonov Regularization is the most commonly used method for ill-posed problems[61] and it has been applied to ECT [25, 62, 63]. Both sides of equation **(3.18)** are multiplied by S^T,

$$S^T \Delta C = S^T S \Delta\varepsilon \tag{3.25}$$

If $S^T S$ is invertible, the equation **(3.25)** would become:

$$\Delta\varepsilon = (S^T S)^{-1} S^T \Delta C \tag{3.26}$$

However, $S^T S$ is a square matrix but still a singular matrix in most cases, so the Tikhonov

regularization factor α is introduced to make the matrix invertible [64]. The result is:

$$\Delta\hat{\varepsilon} = (S^T S + \alpha I)^{-1} S^T \Delta C \tag{3.27}$$

where I is an identity matrix.

Another way of Tikhonov regularization is to obtain $\Delta\varepsilon$ when the square error f is minimized [64].

$$f = \frac{1}{2}(\|S\Delta\varepsilon - \Delta C\|^2 + \alpha\|L(\Delta\varepsilon - \Delta\varepsilon_0)\|^2) \tag{3.28}$$

where $\Delta\varepsilon_0$ is the estimated solution of permittivity change from the same reference point as $\Delta\varepsilon$ that is based on prior information, L is the regularization matrix that acts as a filter that can suppress the high-frequency noises [65].

And the smallest value of f is obtained when both $\|S\Delta\varepsilon - \Delta C\|$ and $\|L(\Delta\varepsilon - \Delta\varepsilon_0)\|$ reach the minimum. This indicates that the difference between the values of estimated capacitance change ($S\Delta\varepsilon$) and measured capacitance change (ΔC) is minimized at the same time as the calculated permittivity distribution ($\Delta\varepsilon$) is close to the estimated result ($\Delta\varepsilon_0$) . The accuracy of Tikhonov algorithm depends on regularization factor μ. It is usually achieved by experiments [66].

3.2.2 Iterative Algorithm

Iterative algorithm is introduced since, the non-linear relationship between capacitance

measurements and permittivity distribution cannot be completely or accurately described by any single-step algorithms.

For iterative algorithms, the key method is to use multiple steps to approach the approximate solution iteratively. The iteration equation between the objective parameters in ECT is normally deduced in the following format:

$$\varepsilon_{k+1} = \varepsilon_k + G_k \tag{3.29}$$

Where ε_k and ε_{k+1} are the k th and $(k+1)$ th approximation to the real permittivity distribution, ε, (*Note: ε is not the change in permittivity*) and G_k is the iteration term upgrading with the number of iterations. Beware of the difference between that In ECT, G_k is an equation containing the discrepancy between the calculated capacitance in each iteration C_k and the measurement C (*Note: is not the change between measurements*) [66].

3.2.2.1 Iterative Tikhonov algorithm

The equation **(3.24)** can be written as:

$$C_{cal} = f(\varepsilon) \tag{3.30}$$

C_{cal} is the calculated capacitance. And the solution is derived by minimizing the square error between the measured capacitances C_0 and C_{cal} [67]:

$$e = \frac{1}{2}\|C_{cal} - C_0\|^2 = \frac{1}{2}[f(\varepsilon) - C_0]^T[f(\varepsilon) - C_0] \quad \textbf{(3.31)}$$

To obtain at least a local minima of e, we find extreme value when the differential of e over g equals zero.

$$e' = \frac{\partial e}{\partial \varepsilon} = [f'(\varepsilon)]^T[f(\varepsilon) - C_0] = 0 \quad \textbf{(3.32)}$$

The entries of $f'(\varepsilon)$ is $f_i'(\varepsilon_j) = \frac{\partial f_i}{\partial \varepsilon_j}$. Recall the definition of Jacobian matrix at the beginning of section 3.2, therefore $f'(g)$ is the Jacobian matrix. Use a Taylor series expansion of equation **(3.32)** around an arbitrary point $\varepsilon = \varepsilon_k$, and neglect the higher-order terms [68, 69]. The linear terms are kept.

$$\Delta\varepsilon_k = -\{[f'(\varepsilon_k)]^T f'(\varepsilon_k)\}^{-1}[f'(\varepsilon_k)]^T[f(\varepsilon_k) - C_0] \quad \textbf{(3.33)}$$

$$\Delta\varepsilon_k = \varepsilon_{k+1} - \varepsilon_k \quad \textbf{(3.34)}$$

Combine equation (3.33) and (3.34) and obtain a simplified iterative equation:

$$\varepsilon_{k+1} = \varepsilon_k - [S_k^T S_k]^{-1} S_k^T (C_k - C_0) \quad \textbf{(3.35)}$$

where $S_k = f'(\varepsilon_k)$ is the Jacobian matrix and $C_k = f(\varepsilon_k)$ is the capacitance.

The inverse matrix of $S_k^T S_k$ cannot be found, because it is not a non-singular matrix. Similar to Tikhonov regularization equation **(3.26)**, therefore, a regularization factor γ is added, and the equation **(3.35)** is modified:

$$\varepsilon_{k+1} = \varepsilon_k - [S_k^T S_k + \gamma I]^{-1} S_k^T (C_k - C_0)] \quad \textbf{(3.36)}$$

Usually in every iteration step, C_k will be updated by finite element method (FEM) and the new permittivity distribution $\bar{\varepsilon}_k$ from the last iteration:

$$C_k = fem(\bar{\varepsilon}_k) \quad \textbf{(3.37)}$$

And the sensitivity map S_k is updated as well, which is governed by equation **(3.19)**.

3.2.2.2 Landweber's Iteration

Basic deduction of iteration [60]: An initial value, A_0, is approximated to S^{-1}. Then a residual matrix is made:

$$R = 1 - A_0 S \quad \textbf{(3.38)}$$

$$\Rightarrow S^{-1} = (1 - R)^{-1} A_0 \quad \textbf{(3.39)}$$

Expand the term of $(1 - R)^{-1}$ at $R = 0$ in Taylor series:

$$S^{-1} = (1 + R + R^2 + \cdots + R^k + \cdots)A_0 \quad \textbf{(3.40)}$$

Define that

$$A_k = (1 + R + R^2 + \cdots + R^{k-1})A_0 \quad \textbf{(3.41)}$$

which is the kth approximation to S^{-1}.

Then change between the (k+1)th approximation of permittivity distribution $\bar{\varepsilon}_{k+1}$, and the reference point $\bar{\varepsilon}_{ref}$, is determined by the (k+1)th approximation of S^{-1}that is A_{k+1}.

$$\bar{\varepsilon}_{k+1} - \bar{\varepsilon}_{ref} = A_{k+1}\Delta C \quad \textbf{(3.42)}$$

Expanding $A_{k+1}\lambda$ by equation **(3.41)**,

$$\bar{\varepsilon}_{k+1} - \bar{\varepsilon}_{ref} = \bar{\varepsilon}_k - \bar{\varepsilon}_{ref} + R^k A_0 \Delta C \quad \textbf{(3.43)}$$

Combine equation **(3.38)**, **(3.41)**, we can get that:

$$R^k A_0 = A_0(1 - SA_k) \quad \textbf{(3.44)}$$

And substituting the term in equation **(3.43)** with equation **(3.44)** gives

$$\bar{\varepsilon}_{k+1} = \bar{\varepsilon}_k + A_0(\Delta C - SA_k\Delta C) \quad \textbf{(3.45)}$$

This equation provides a basic clue for iterative algorithms.

Landweber's iteration is an algorithm to solve ill-posed linear inverse problems. An initial approximation is given by S^T multiplied by a factor α, so substitute $A_0 = \alpha S^T$ into equation **(3.45)**.

$$\bar{\varepsilon}_{k+1} = \bar{\varepsilon}_k + \alpha S^T(\Delta C - SA_k\Delta C) \quad \textbf{(3.46)}$$

Then this iteration start with an initialized $\bar{\varepsilon}_0$, the initial value is controlled by the pre-known knowledge about the sensing area and the rate of converging is controlled by the factor α. The expansion of Taylor series in equation **(3.40)** is completed under the condition on norm of the residual matrix:

$$\|R\|_2 = \|1 - A_0S\|_2 < 1 \quad \textbf{(3.47)}$$

According to equation **(3.46)**, this condition limits the range of the factor α.

$$\|\alpha S^T S\|_2 < 2 \quad \textbf{(3.48)}$$

From [60], a suitable value of gain factor α is estimated to be :

$$\alpha = 2/\epsilon_{Max} \tag{3.49}$$

where ϵ_{Max} is the maximum eigenvalue of matrix $S^T S$.

FEM is used in this algorithm as well, and it is substituted in to equation **(3.46)**:

$$\bar{\varepsilon}_{k+1} = \bar{\varepsilon}_k + \alpha S^T(\Delta C - fem(\bar{\varepsilon}_k) + C_{ref}) \tag{3.50}$$

3.3 Summary

By solving the forward and inverse problems in ECT, the permittivity distribution is derived. As an inverse problem solver, the different algorithms are chosen for appropriate applications. FEM plays a significant role in both problems, especially for iterative algorithms where the calculated capacitances $fem(\bar{g}_k)$ implemented.

Brief overview of the inversion methods in chapter enables selection of a suitable reconstruction algorithm. In following chapters single step Tikhonov regularisation algorithm as a robust and simple algorithm, was employed for range of new conductivity based ECT and hybrid MIT-ECT combinations. Both forward model and sensitivity matrix are extended to complex permittivity values, which enables analysis of ECT in conductive medium.

Chapter 4 ECT for Floating Metal

4.1 Introduction

ECT is a non-invasive method which produces tomograms of permittivity distributions by using capacitance measurements of material under test [66, 70]. Generally, ECT is considered as a suitable imaging tool for dielectric materials. In many application areas the material under test may not be a purely dielectric, but contains conductive specimen, whose electromagnetic property is different from dielectric. In the case of having a metallic sample in ECT sensor, it will bring a equipotential body in the area and make the ECT problem extreme nonlinear.

For grounded metal in known location, Ville Rimpiläinen *et al*. set the boundary condition of metal to zero voltage to solve the problem of grounded conductor shaft in a mixer [53]. For the grounded metal of unknown location, Maomao Zhang *et al*. introduce MIT to find the location of metal and image the dielectric contrast in the remaining area in the sensor [71]. On the other hand, for the floating metal, the conducting surface is equipotential but not in the voltage of zero. The floating metal between electrodes will increase the measured capacitance due to the reduction in spacing between the electrodes. Dixiang Chen *et al*. designed a security screening system using a planar capacitance sensor matrix to generate an image of an floating steel sample [72]. However the tomographic method has not been used in their screening system, the steel sample is directly imaged by the capacitance measurement of the planar sensor. In our ECT experiments, by calculating this capacitance change caused by the metallic sample in ECT, an illusion of the permittivity change is reconstructed at the location of the metallic sample. A combination of permittivity change and presence of metal sample can also be imaged using ECT. Imaging metallic samples using ECT can be potentially very useful in various areas. Possibility of metal flow imaging using ECT can be very interesting. Simultaneous reconstruction of metallic samples and dielectric samples using ECT can provide a novel solution in many non-destructive evaluation applications where there is a mixture of conductive

and dielectric medium.

This chapter presents imaging metallic samples and simultaneous imaging of metallic samples and dielectric samples for the first time. Analysis of metallic sample as floating and grounded conductors is shown in simple capacitance measurement enabling a better understanding of metallic imaging using ECT.

4.2 Methodology to Image both Dielectric and Conductive Samples

4.2.1 Forward Model Setting and Inverse Solver

ECT process is to convert the capacitance measurements into an image of permittivity distribution. To meet the requirements of ECT forward model (expatiated in **section 3.1**), the sensing region should has no or very low-conductivity components. Since the existence of conductor is beyond the consideration of an ECT process, the introduction of metallic sample into sensor makes the ECT impossible to reconstruct the conductivity distribution of the metal. Therefore some researchers tried different ways to dig out the information of metallic sample. Hyenkyun Woo *et al* applied a tracking method for the grounded conductor [73], or a method proposed in [71] shows how MIT guided ECT can image both grounded conductor and permittivity contrasts. **Figure 4.1** shows the ECT sensor array with grounded and floating metallic inclusions.

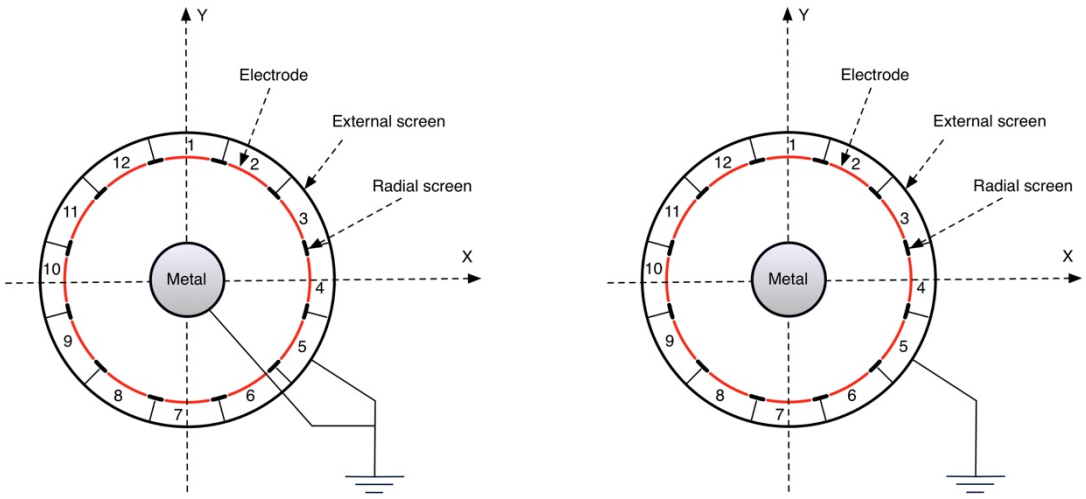

(a) (b)

Figure 4.1: Schematic drawings about cross section of a 12-electrode ECT sensor with **(a)** grounded metal or **(b)** floating metal.

When a metallic sample stands in the ECT sensor, as in **Figure 4.1(b)**, the high conductivity ($\sigma > 10^6$) performs as an equipotential in electrical quasi-static mode, *i.e.* the electrical voltage drops on a metal is negligible. In **Figure 4.1(a)**, the conductor is grounded, where except for that the voltage potential remains the same within the region of conductor, the value of the voltage on the conductor is zero. When both dielectric and highly conductive samples exists in the sensor region, to visualize these two types of inclusions, different settings are applied to grounded and floating conductor.

1. In the case of grounded conductor, to image the rest region excluding the conductors, the forward model of ECT can be modified since the boundary condition of the sensing domain is changed. The grounded metal is set as an extra grounded “electrode”, the voltage potential remains at zero [71]. The reference measurement is also updated: a measurement of the grounded metal standing in the sensor is used.

2. In the case of a floating conductor in ECT, the settings are different in electrostatic model or electro-quasi-static one.

2.1 If the static model is used in forward problem, the region of metal is set as the same voltage but still unknown. Then the voltage will be calculated in forward model.

2.2 If it is electro-quasi-static mode, every element in the mesh has a complex permittivity, which consists of both permittivity (ε) and conductivity (σ) with signal frequency (ω), *i.e.* $\varepsilon_{complex} = \varepsilon + \frac{\sigma}{j\omega}$. Since the frequency of exciting voltage in ECT is within radio frequency, the permittivity of metal is conductivity-dominant, *i.e.* the effective permittivity is an imaginary number [74].Then a big value of conductivity is assigned to the region of conductor, and normally the order of magnitude is about 7.

For the traditional ECT forward model, the permittivity of the sensing region is a real number. Therefore, the real-number ECT forward model cannot give a solution to conductor. To complete the settings above, prior information is needed, which includes the size and location of metallic sample. However without using another imaging or measure modality to provide prior information, the ability of ECT to visualise the metal will be analysed in next section.

In this chapter, a standard Tikhonov regularisation algorithm is used to calculate permittivity changes:

$$\Delta\varepsilon = [S^T S + \gamma I]^{-1} S^T (C_s - C_r) \tag{4.1}$$

where S is the sensitivity matrix, and the level of regularisation is controlled by the factor γ, which is selected empirically.

4.2.2 Analysis of Feasibility on ECT Imaging Grounded and Floating Conductor

An ideal model of a parallel-electrode capacitor is shown in **Figure 4.2**, the spacing is L and the size of electrode is A. A metallic sample with width of D is inserted between the electrodes, and the distance between the left edge of the metal and excited electrode is D_1. The permittivity of air is ε_0.

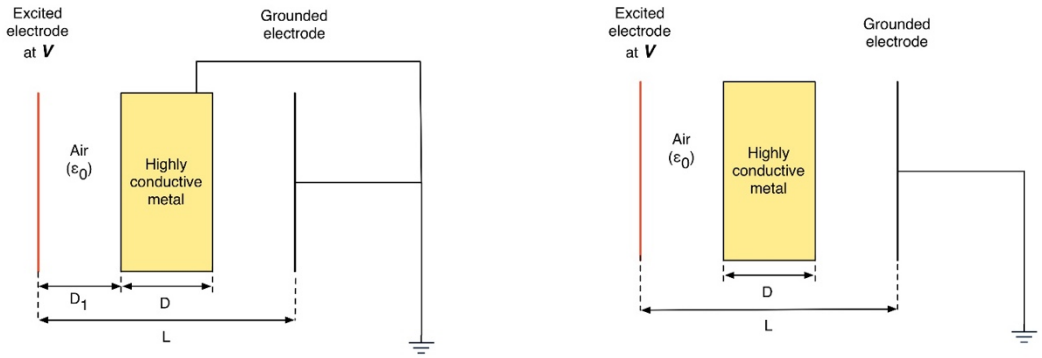

Figure 4.2: An ideal parallel electrode model with **(a)** a grounded metallic sample **(b)** a suspended metallic sample.

If the metal is grounded, as shown in **Figure 4.2(a)**, the capacitance between the electrode, $C_{grounded}$, can be expressed as:

$$C_{grounded} = \frac{\varepsilon_0 A}{D_1} \tag{4.2}$$

If it is suspended as **Figure 4.2(b)**, the capacitance $C_{non-grounded}$ can be expressed as below:

$$C_{non-grounded} = \frac{\varepsilon_0 A}{L - D} \tag{4.3}$$

In the pure dielectric model of ECT, in **Figure 4.3**, the permittivity distribution is the only thing can be calculated, so the high conductivity is the region of metal cannot be computed in this way. But the conductor between two electrodes increase the capacitance measurement, this produces an illusion of higher permittivity in the sensing area.

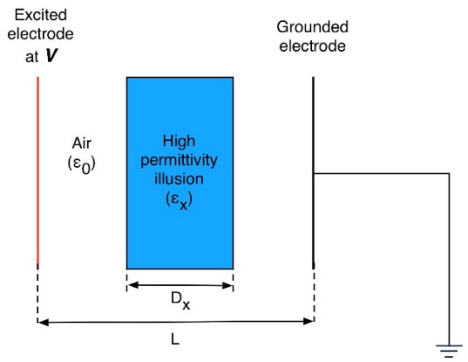

Figure 4.3: An equivalent dielectric illusion of an conductor.

Let's set that the permittivity of the illusion is ε_x and homogeneous and the width is D_x. The capacitance for this illusion is:

$$C_{illusion} = \frac{1}{\frac{L - D_x}{\varepsilon_0 A} + \frac{D_x}{\varepsilon_x A}} \tag{4.4}$$

To obtain the relationship between the conductor and the illusion, we make $C_{illusion}$ equals $C_{grounded}$ and $C_{non-grounded}$ respectively.

For grounded metal:
$$\frac{\varepsilon_x}{\varepsilon_0} = \frac{D_x}{D_x + D_1 - L} \quad \textbf{(4.5)}$$

For floating metal:
$$\frac{\varepsilon_x}{\varepsilon_0} = \frac{D_x}{D_x - D} \quad \textbf{(4.6)}$$

If the permittivity of illusion is k times the permittivity of air, *i.e.* $\varepsilon_x = k * \varepsilon_0$, then relationships between the two values of width are:

For grounded metal:
$$D_x = \frac{k}{k-1}(L - D_1) \quad \textbf{(4.7)}$$

For floating metal:
$$D_x = \frac{k}{k-1}D \quad \textbf{(4.8)}$$

From the equations **(4.7)** and **(4.8)**, if the grounded metal is placed in ECT sensor, the size of the illusion is related to $(L - D_1)$, not to the size of the metal, D. However for the floating metal, the sizes of illusion and metal are related to each other. In fact, both $(L - D_1)$ and D are the distance shortened between parallel electrodes. So the width of illusion is proportional to shortened spacing:

$$D_x \propto D_{shortened} \quad \textbf{(4.9)}$$

Therefore, for 1-D consideration, the floating conductor performs like a dielectric sample, where ECT can be used to image this dielectric illusion. In the following sections, the experiments on imaging metallic and dielectric sample using ECT are carried out.

4.3 Imaging Metallic and Dielectric Samples

A 12-electrode sensor is used to assess the ECT imaging of floating metals. The capacitance measurement unit is PTL-300E, which has been mentioned in **section 2.1** [45]. The metal imaging results here are based on this ECT device, which is a charge transfer system. For more information on various ECT hardware design see [40, 75, 76].

4.3.1 ECT Imaging of Metallic Samples

To show imaging of metallic samples, a metallic pipe is used various locations. The metallic pipe of 32mm in diameter is used to show the feasibility of metallic sample imaging, as shown in **Figure 4.4**. The experimental results are listed below. The directions of X-Y axes on the sensor are shown in **Figure 4.1**. The pipe is moved from the centre (0, 0) to (0, 5) cm in the sensor. The reconstruction images are in **Table 4.1**. As expected, an image of exterior surface of the conductor is possible obtained by ECT, so it might be better to state that the ECT is capable of imaging floating metal in topographic imaging mode. It is interesting to see that the simple inversion of equation **(4.1)** primary designed for permittivity imaging is capable of producing surfaces of floating metal. Although the images of **Table 4.1**. Shows a profile of permittivity change but a transition from air to conductor is sharp change in electric field. The standard Tikhnov algorithm is introducing an artificial smoothness profile as trade off to improving the ill-posedness of the ECT inverse problem. In reality the metal will act as a shield so there is no variation inside can be detected.

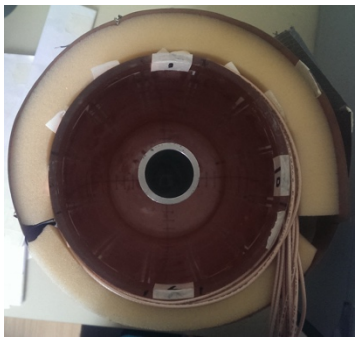

Figure 4.4: A floating metallic pipe stands in the ECT sensor.

Table 4.1: ECT imaging of floating conductor.

Pipe's centre (x,y) /cm	**(0,0)**	**(0,1)**	**(0,2)**
ECT images	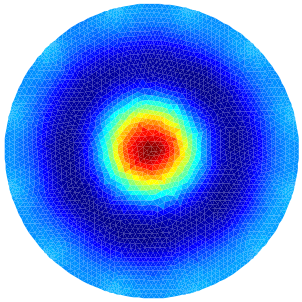	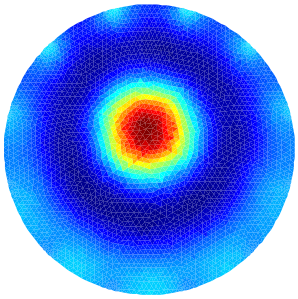	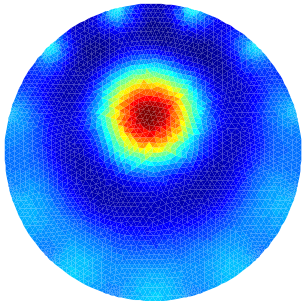
Pipe's centre (x,y) /cm	**(0,3)**	**(0,4)**	**(0,5)**
ECT images	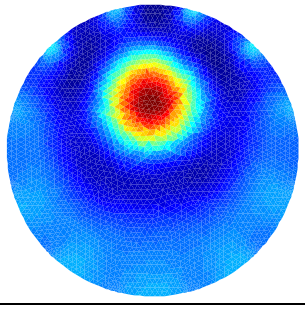	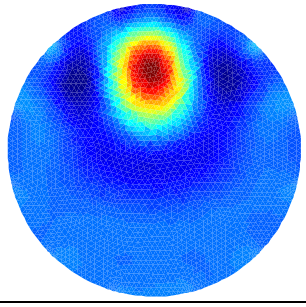	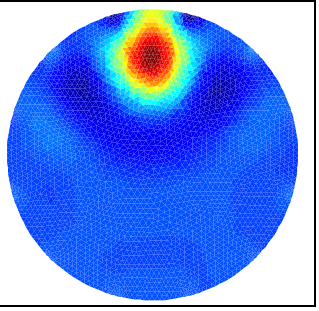

4.3.2 ECT Imaging of Metallic and Dielectric Samples

Remaining results show that simultaneous reconstruction of metallic and dielectric inclusions

is examined by using a metallic pipe and wooden bars. The external diameter of the metallic pipe is 32 mm. the diameter of the wood bar is 23 mm. At first only one wooden sample is placed next to the pipe. In **Table** 4.2, the pipe is fixed at (0, 4) cm, and the wooden bar is moved along the Y-axis from (0,-4) to (0, 0) cm. We can see that the wood bar is the region of lighter colour, *i.e*. smaller reconstructed value of permittivity, while the red area stands for the metallic pipe. This is not just because of the size difference between these two samples but the different effective capacitance increment caused by them. In other words, the pipe raises more capacitance measurement than the wooden bar.

From the images, they clearly indicate that the wooden bar is approaching the metal. But when the wooden bar is close to the pipe, these two samples are merged into one on the reconstruction image. Since separating two adjacent dielectric samples is a difficult problem existing in normal ECT [55], it is also hard for a metal pipe and a wood bar.

Table 4.2: ECT images of metal and wood.

Locations of samples' centre (x,y) / *cm*	**Photos of experiment scenario**	**Reconstruction images**
Metal at (0,4) **Wood at (0,-4)**		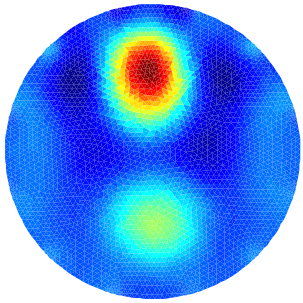
Metal at (0,4) **Wood at (0,-3)**		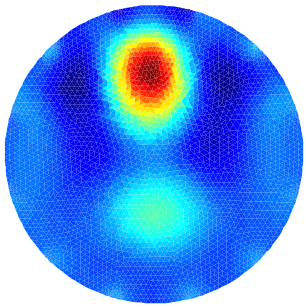
Metal at (0,4) **Wood at (0,-2)**	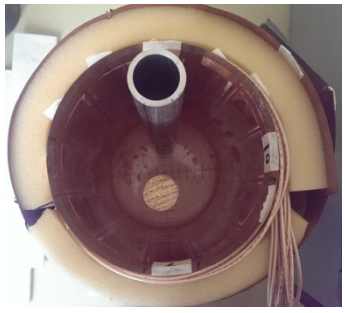	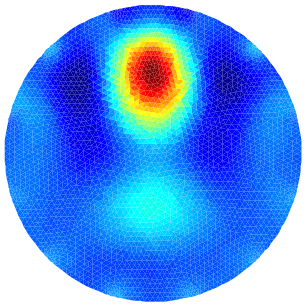
Metal at (0,4) **Wood at (0,0)**	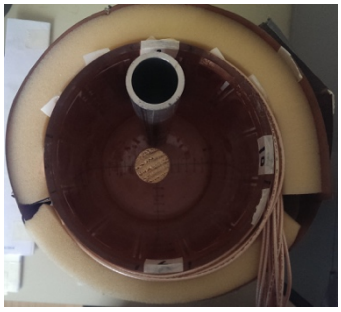	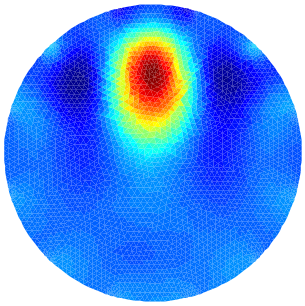

In **Table 4.3**, the pipe is placed at the centre. The wooden samples are standing on one or two sides of the pipe. The ECT deformed images implies the wooden samples, but still cannot separate it from metallic pipe.

Table 4.3: ECT images of metal and wood.

Locations of samples' centre (x,y) / *cm*	**Photos of experiment scenario**	**Reconstruction images**
Metal (0,0) **Wood (0,-4)**	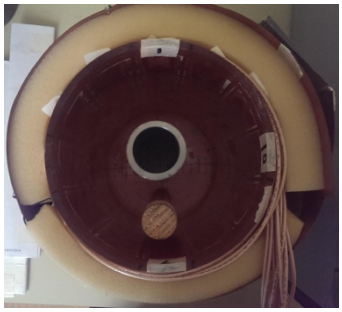	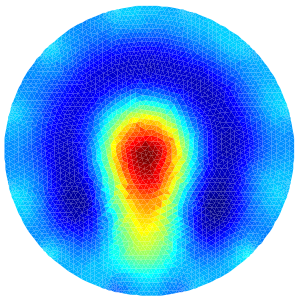
Metal (0,0) **Wood 1 (0,4)** **Wood 2 (0,-4)**		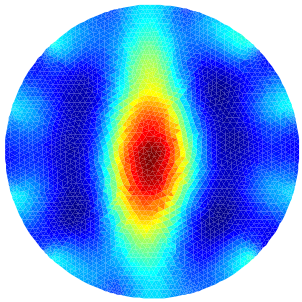

For the cases of using the air-filled sensor as reference scenario, the ECT fails to separate the wood samples from metal. When the reference measurements are updated with the metal information, the quality of image can be improved. When the measurement of the metallic pipe standing in the air background is regarded as a reference measurement, the ECT can easily reconstruct and separate the wooden samples, as shown in **Table 4.4**. To compare the reconstruction quality, an ECT image of only two wooden samples is listed as well. The two ECT images in first two rows demonstrate a consistency between two scenarios. In third row, the result of a grounded metal with two wooden samples is presented, where the measurement of the grounded metallic pipe standing in the air background is regarded as a reference measurement. The value of the calculated permittivity distribution is in different scale from the first two rows, but also indicates the information of the two wooden bars. To detect the dielectric samples, prior information about the conductor is important. Updating the reference measurements has a big improvement in the detection and reconstruction of the dielectric components.

Table 4.4: ECT images of wooden samples with different reference measurements.

Reconstruction of two wooden samples with air background		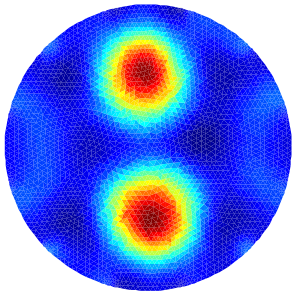
Reconstruction of two wooden samples with floating metal background		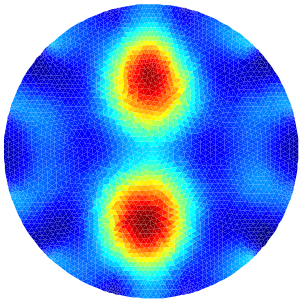
Reconstruction of two wooden samples with grounded metal background		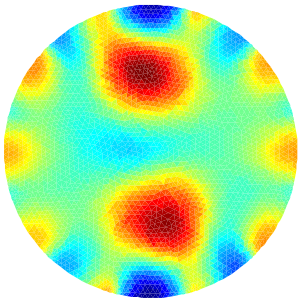

4.4 Summary

In this chapter, the ability of ECT to detect a floating metallic sample or a metallic sample with dielectric samples is presented. The reason why the permittivity images of ECT can indicate the floating conductor is explained in the one-dimensional model for changes in capacitance data with floating metal as well as the meaning of the metal sample image through an algorithm primarily designed for permittivity imaging. However, ECT is not capable to distinguish the metal and dielectric in our experiments. MIT is a good choice to find the metal component, and then by combining the images from MIT and ECT, the metal and dielectric samples can be distinguished. In this chapter we have demonstrated ECT is capable of imaging dielectric and

metallic samples. Imaging interior of dielectric samples is possible in ECT while the ECT metal imaging only capable of imaging of the surface of a metallic object. A combined ECT-MIT might be possible to extend the imaging of interior of metallic object, which is a subject of our future studies. The future potential of the ECT in imaging outer surface of metallic sample will be explored in future studies for metrology applications and industrial process applications such as metal flow imaging.

Chapter 5 MIT-ECT for Grounded Metal

5.1 Introduction

Metal can cause a large change of electrical field in ECT and subsequently large change in the sensitivity map. This will make the ECT image reconstruction inaccurate, especially if a free space sensitivity map is used. This effect is more severe in grounded conductor than floating conductors, so this chapter focuses on grounded conductor. In order to improve the accuracy of the sensitivity map, one needs to gain more information about the conductivity distribution in ECT problem. It is well known that MIT is sensitive to electrical conductivity; therefore, it can be used to visualize the conductivity distribution of the target under test. In this chapter, a dual-modality MIT and ECT system is proposed to fully employ the advantage of MIT in ECT image reconstruction in such an imaging context. This is a novel technique to improve the accuracy of the sensitivity map, and subsequently reduce the inaccuracy in inversion of the ECT. Both simulated and experimental results are presented, which demonstrate the feasibility of the proposed method.

Typically, a time difference imaging is used in ECT image reconstruction: the change in permittivity is reconstructed by the sensitivity map of reference condition and the difference between reference measurements and sample measurements [70]. Therefore, the accuracy of a sensitivity map has a significant effect on the reconstruction quality.

When a highly conductive sample is under test, especially for grounded conductors, in the sensor area, the electric fields will be deformed. Therefore, the sensitivity map of a typical reference condition, *i.e.* air-filled sensor, is not accurate [55]. To decrease the nonlinearity caused by high conductivity, a precise forward model must be introduced. This modified model, which is close to the real physical scenario, includes the highly conductive content and modelled as ground conductor. The previous study of EIT with metallic samples in [77], the

surface of metal is regarded as one electrode of the sensor, that is electrically grounded. Furthermore, the boundary condition on the shaft is set at zero voltage as well. Here we extended this to the case that the location of conductor must be identified first.

To detect and identify the high conductivity in sensor area, MIT is used and using the location of grounded metal we can build a precise sensitivity map in ECT. MIT aims to visualized the distribution of passive electromagnetic properties in particular permeability μ or conductivity σ [13]. In MIT, the magnetic field induces eddy currents in the conductive object, which produces a change in the magnetic field received by the receiver coils of a MIT sensor. These two tomographic technologies: MIT and ECT are combined as a dual modality to be introduced in this chapter. MIT is not sensitive to dielectric permittivity variations, making a sequential data fusion possible. The information about electrical conductivity from MIT feeds into ECT image reconstruction software allowing reconstruction of both conductivity and permittivity. Compared with the dual-modality ERT and ECT system have been built in [78-80], ECT and MIT have a common feature: no requirement of electrical contact to objects under test, while ERT requires electrical connection to objects. In [81], a two electrode capacitive measurement system is used to image either void (dielectric permittivity change) or rebar . In this chapter we propose a dual modality method, in which dielectric permittivity changes and grounded conductor can be monitored simultaneously. This dual modality imaging method provides a wider range of applications for ECT, where the conductive media between an object and a sensor is not known. This chapter demonstrates that the ECT imaging capability of dielectric variations will be substantially reduced, in particular when the ground conductors are close to dielectric inclusions. The dual modality has potential applications for mixture of highly conductive samples and dielectric ones, such as defect detection for reinforced concrete.

The aim of this chapter is to investigate a dual modality imaging for a combination of ground conductors and dielectric inclusions using MIT and ECT. The structure of the chapter is organised as follows. In **section 5.2**, the ECT and MIT hardware are introduced. In **section 5.3**, the error tolerance of ECT is will be evaluated by the figure of merits, which is developed by Andy Adler *et al.* [82]. In **section 5.4**, the experiment of dual-modality MIT/ECT is conducted, and the final results are assessed.

5.2 ECT and MIT Hardware

Here we briefly describe ECT and MIT system, sensor and forward modelling and sensitivity maps. A 16 channel MIT system and a 12 channel ECT system is used for sequential data fusion in dual modality ECT and MIT imaging, **Figure 5.1** shows both sensor arrays.

(a) **(b)**

Figure 5.1: (a) The 12-electrode ECT sensor; **(b)** The 16-coil MIT sensor.

5.2.1 ECT

A typical ECT sensor consists of 6, 8, 12 or 24 electrodes [83], which are evenly mounted outside a pipe-shaped non-conductive wall and separated with radial screens. And an external screen for shielding the noise from outside is installed. All electrically grounded screens reduce the effect of the external capacitance between pairs of electrodes. In some special cases, where the wall is conductive, the electrodes are built on the inner surface of the wall, like a metal vessel or pipe.

Figure 5.1(a) is the ECT sensor used in our experiment, which is composed of a plastic pipe, 12 electrodes, radial screen between the electrodes and external shielding. The external diameter of pipe is 150 mm, the size of the electrode is 217×32 mm^2 and the screens between the electrodes are 3 mm wide. The capacitance measurement unit is the PTL 300E ECT system, whose excitation frequency is fixed at 1.25 MHz. Twelve channels are connected to the electrodes to measure the inter-capacitance.

5.2.2 MIT

In this study, a 16 channel MIT system is used to realise the proposed dual-modality imaging technique. The MIT system consists of: (1) a coil array of sixteen air-cored inductive sensors, shown in **Figure 5.1(b)**; (2) MK-I system which mentioned in **section 2.2**, where the data process and image reconstruction take place. This system was designed to measure targeted object(s) with high conductivity, which corresponds to a negative imaginary part of the magnetic field perturbation, as such, the measurements can be approximated by their amplitudes, the phase shifts are therefore neglected [84]. The system development has been reported in [48], and many applications have been proposed using this system architecture.

5.3 Analysis of Metallic Sample in ECT Imaging

Our experimental scenario is schematically shown in **Figure 5.2**, which is an ECT sensor with grounded conductor. For image reconstruction algorithm in both ECT and MIT we have used standard Tikhonov regularisation method [66]. We have selected an empirical regularisation parameter for MIT and one empirical regularisation parameter for ECT. This way we can assume same level of regularisation in all cases allowing better comparison. The same level of thresholding was used for post processing imaging results for quantitative imaging comparisons.

5.3.1 Reference Measurement

In our experiment the sample under test consists of a metallic bar and a wooden bar. Traditional ECT utilizes the difference between the reference capacitance (C_r) and the measured capacitance of the sample (C_m) to visualize the dielectric distribution change. In the case of sensing a mixture of a metallic sample and a dielectric sample, without knowing the existence of the metal, the capacitance measurement of the air-fulfilled sensor (C_{air}), is chosen as the background data (or reference data). The difference between the measurement of samples (C_m) and C_{air} is utilized to solve the inverse problems; however the metal will affect the imaging on the rest of dielectric region. Therefore choosing the capacitance measurement of metal and air, ($C_{metal+air}$) as the reference measurement describes the real condition more precisely.

5.3.2 Modification of Forward Model

If the location and size of grounded conductors are known, we can modify the ECT forward model to account for these grounded conductors. In the case of a metallic bar, the sensitivity map of a pair of electrodes is shown in **Figure 5.3** [53, 55]. The sensitivity "valley" is split up around the metallic bar, since the metallic bar is defined as a grounded electrode of the sensor. This forward model is proximate to the real condition within the sensor area.

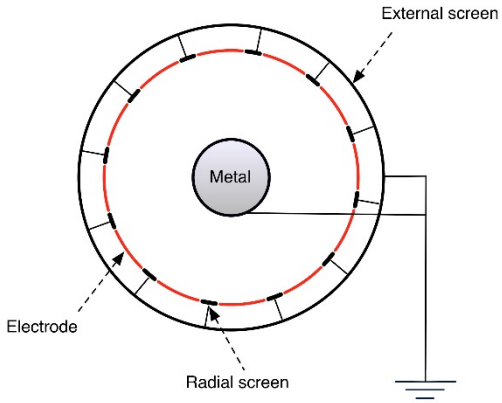

Figure 5.2: Schematic drawings about cross section of the ECT sensors.

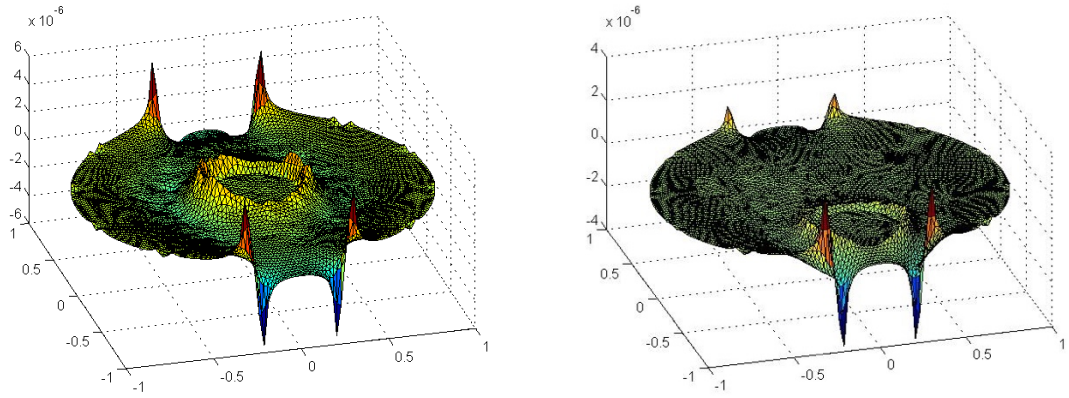

Figure 5.3: The sensitivity of opposite capacitance measurement when the metal bar stands in the centre and near one electrode.

Two images will be reconstructed from different reference measurements and different forward model in **Figure 5.4**. In **Figure 5.4 (b)**, the traditional ECT forward model and background data from air-filled sensor indicates the imaging the mixed material under test is not possible. The updated background data and forward model provides a clear distribution of dielectric in **Figure 5.4 (c)**.

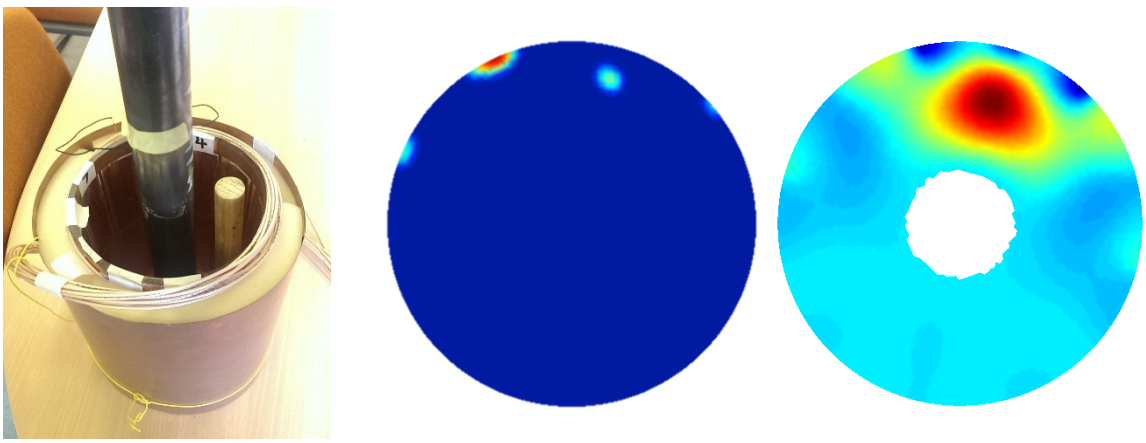

(a) **(b)** **(c)**

Figure 5.4: (a) Real position of samples in the ECT sensor; **(b)** the reconstructed image with the reference measurement of air; **(c)** the reconstructed image with reference measurement of

iron bar in the middle and updated forward model.

5.4 Dual-modality MIT/ECT

MIT is used to obtain the size and the location of metallic bar in a dual modality solution proposed in this chapter. In this dual-modality experiment, separate MIT and ECT sensors measure the samples individually. As mentioned in [13], theoretically MIT is capable to image both conductivity and permittivity, but the in reality MIT has almost no sensitivity to dielectric permittivity. The MIT only focus on visualizing the electrical conductivity distribution and is not affected by dielectric sample. So the information of the metal position from MIT is transferred to the forward model of ECT, and then the space of sensing area excluding the metal is visualized by ECT. The experiment workflow can be explained in **Figure 5.5**. The visualized image of MIT may include some errors in location and dimensions. These errors will have an impact on the final results on the image of the dielectric part within the sensing area. Therefore, the error is simulated and corresponding effect is analysed in **section 5.4.1**.

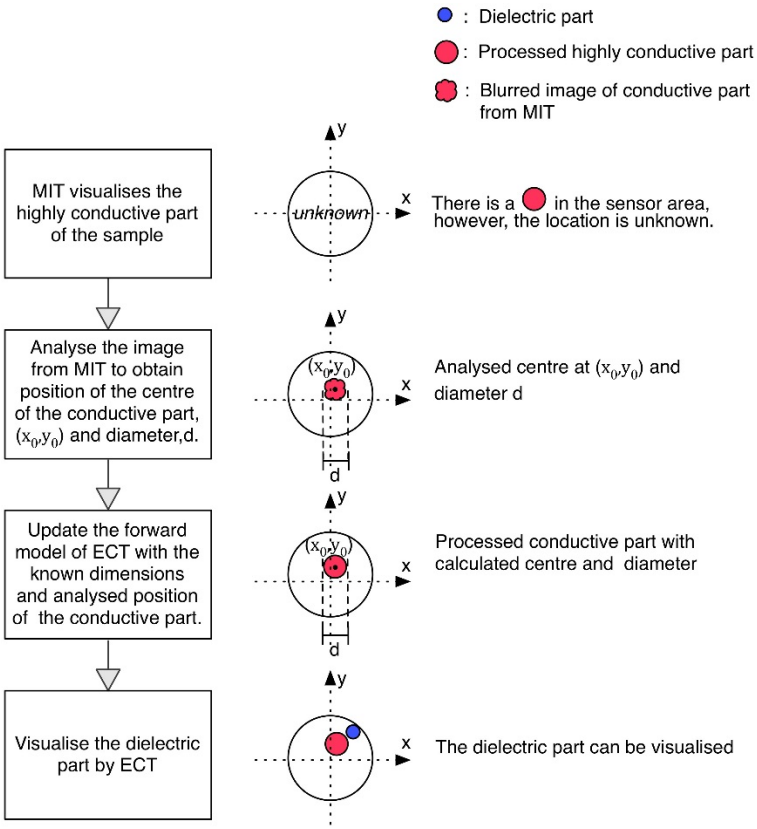

Figure 5.5: The experiment steps and relevant reconstructed image of the sensing area.

5.4.1 Simulation of Errors in Location and Size of Metal Sample

To identify the size and location of metal, MIT is introduced to image the conductivity distribution. However as a result of the ill-posed and non-linear nature of soft-field tomography and the noise in MIT measurement, the reconstruction image of MIT will have some errors in location and dimensions. Therefore, before combining the ECT with MIT, we simulate errors from MIT images by defining different size and location of metal in ECT forward model. Meanwhile, the capacitance measurements of sample and background kept the same. To analyse the quality of the ECT reconstruction quantitatively, the GREIT figure of merit proposed in [82] is introduced in our test. The figure of merit includes centre of gravity (CoG), resolution and shape deformation (SD). Resolution measures the size of reconstructed targets as a fraction of the medium; SD measures the reconstructed image with threshold setting which

does not fit within a circle of an equal area, since reconstruction algorithms typically create circular images for targets.

Table 5.1: Reconstruction images when radius of metal is ***R***.

Distance to centre	**0**	**0.1 *R***	**0.2 *R***	**0.3 *R***	**0.4 *R***
Reconstruction	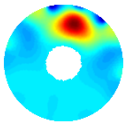	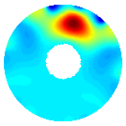	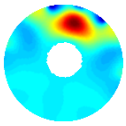	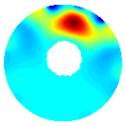	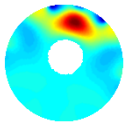
Reconstruction with threshold					

0.5 *R*	**0.6 *R***	**0.7 *R***	**0.8 *R***	**0.9 *R***	**1.0 *R***
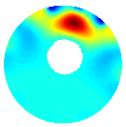	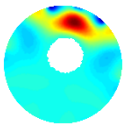	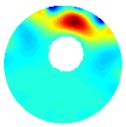	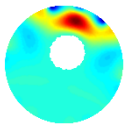	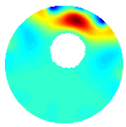	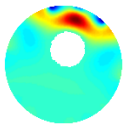
					

To obtain each figure of merit, the reconstructed image is transferred to a square gridding of 1000 × 1000 divisions. In this experiment, the iron bar is $R = 2$ *cm* in radius, and stands at the centre, (500, 500) in coordinate frame. For evaluate the effect of the simulated errors, reference image and figures of merit should be achieved by feeding these practical information of size and location to the forward model of ECT. The reference image is shown in the column of "Distance to centre" = 0 in **Table 5.1**, and reference figures of merit are obtained by processing this image.

5.4.1.1 Simulation of Location Error

Firstly the real CoG of the wooden sample is obtained. To simulate the error in location, the metallic bar is assumed to approach the real CoG of the wooden sample in a step of 0.1 *R* in the forward model of ECT. The quality of the image depends on the reconstruction of the dielectric sample. To obtain figures of merits, images are converted to binary images with

threshold. In our test, the threshold is set as 80% of the maximum amplitude of reconstructed permittivity matrix. When the radius of the iron bar is *R*, **table 5.1** indicates the reconstruction image of the wooden sample, as the iron bar is moving towards the CoG of the wooden sample in the forward model of ECT.

5.4.1.2 Simulation of Size Error

Since images from MIT can be smaller or larger than the real size of the metallic sample, in our test, the radius of bar is assumed to be 0.8 *R* and 1.2 *R* for the simulation of errors in size. Meanwhile, the error in location is also present while the size errors exist. So the simulation of location error is conducted in different radius set. **Table 5.2** and **Table 5.3**indicate the reconstruction images when the radius is 0.8 *R* and 1.2 *R* respectively.

Table 5.2: Reconstruction images when radius of metal is 0.8***R*.**

Distance to centre	**0**	**0.1 *R***	**0.2 *R***	**0.3 *R***	**0.4 *R***
Reconstruction	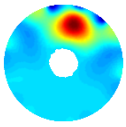	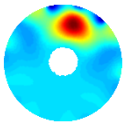	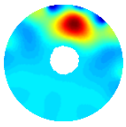	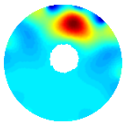	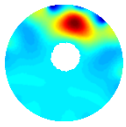
Reconstruction with threshold	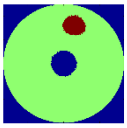		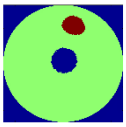		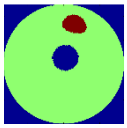

0.5 *R*	**0.6 *R***	**0.7 *R***	**0.8 *R***	**0.9 *R***	**1.0 *R***
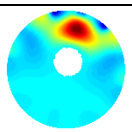	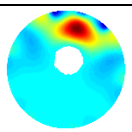	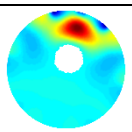	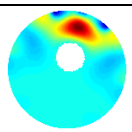	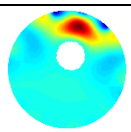	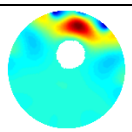
					

Table 5.3: Reconstruction images when radius of metal is 1.2***R***.

Distance to centre	**0**	**0.1 *R***	**0.2 *R***	**0.3 *R***	**0.4 *R***
Reconstruction	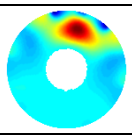	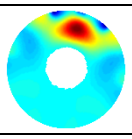	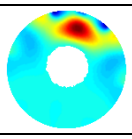	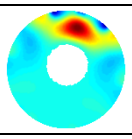	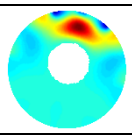
Reconstruction with threshold	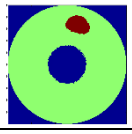	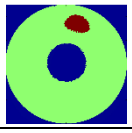	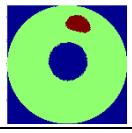	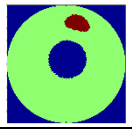	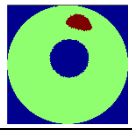

0.5 *R*	**0.6 *R***	**0.7 *R***	**0.8 *R***	**0.9 *R***	**1.0 *R***
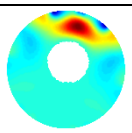	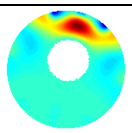	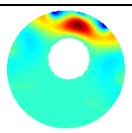	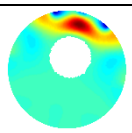	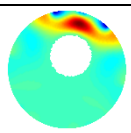	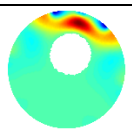
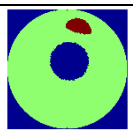	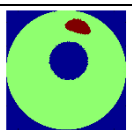	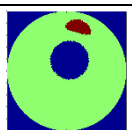	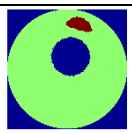	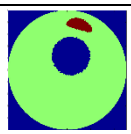	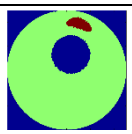

5.4.1.3 Simulation Results

In this simulation, the iron bar is supposed to be moved with a maximum distance of R from the centre. According to the results shown in **Table 5.1**, **Table 5.2**,

Table 5.3 and **Figure 5.6**, the images and relevant figures of merit are decaying monotonically while the error in location is increasing. The quantitative analysis of the figures of merit is done below.

(1) Shift of the CoG: In **Figure 5.6(a)**, the reference CoG of the wooden sample is (589, 824). When the metallic bar is moving with the radius of 0.8R, R and 1.2R, the maximum shift of CoG is 3.8%, 5.1% and 6.3% of the diameter of the sensing area respectively.

(2) Resolution change: in **Figure 5.6(b)**, the minimum resolution is 16.32%, 15.59% and 14.71%, when the radius changes from 0.8R to R and finally to 1.2 R. The decrement in

resolution is 11.4%, 15.3% and 20.1% from the reference resolution (18.41%).

(3) SD change: In **Figure 5.6(c)**, the reference SD is 3708. The maximum SD reaches 7994, 8358 and 8956, while the radius is 0.8 R, R and 1.2 R respectively; accordingly the deformation rate is 116%, 125% and 142% from reference.

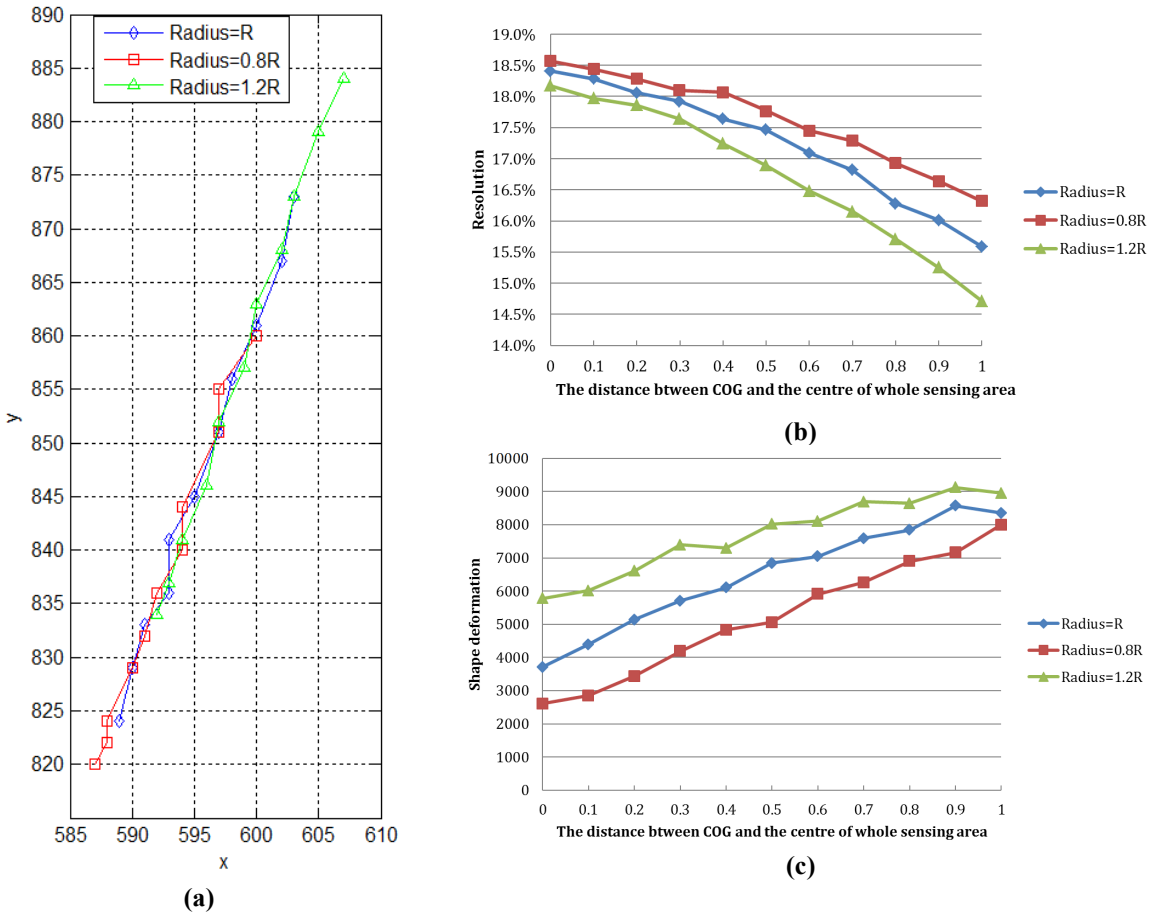

Figure 5.6 (a) The tracks of CoG; **(b)** the resolution change; **(c)** the SD change.

In addition, when the metallic bar is moving away from the dielectric sample from the centre (500,500), it causes very small change on the reconstruction and figure of merit from our experiments. Similarly, both the images and the figures show a better outcome when the radius is 0.8*R*, where reduction in size results in the same effect caused by movement of the iron bar away from the wooden sample.

5.4.2 Results from MIT

To investigate the location information from MIT, the real location and the analysed location will be compared. The centre point of the region is set as (0, 0) cm, and the metallic bar is moved from the central point to the edge in the step of 1 cm along the horizontal axis (x-axis). Both the reconstruction images and COGs of the metallic bar are obtained in **Table 5.4** and **Figure 5.7**. Normally different threshold settings have varying COGs under a small range. In this experiment, the threshold is set to match the size of the reconstructed metallic bar to the real size.

Table 5.4: The table of reconstruction images, analysed COG change and error rate.

Reconstruction image	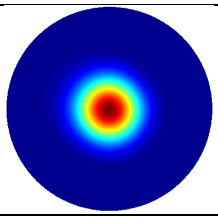	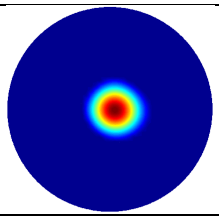
Real COG coordinate (x_0, y_0) /(cm)	**(0,0)**	**(1,0)**
Analysed location (x_i, y_i) /(cm)	**(0.188,0.188)**	**(0.797,0.100)**
LER	**13.32%**	**11.32%**

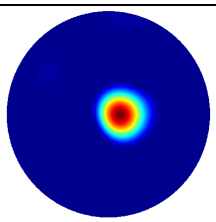	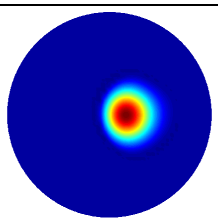	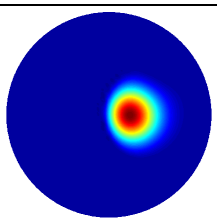
(2,0)	**(3,0)**	**(4,0)**
(1.558,0.197)	**(2.145,0.221)**	**(2.704,0.199)**
24.20%	**44.16%**	**65.57%**

In **Table 5.4** both the practical and analysed location of COG are listed. The location error rate (LER) is defined as the equation below:

$$LER = \frac{\|(x_i, y_i) - (x_0, y_0)\|}{R} \times 100\% \tag{5.1}$$

In **section 5.3**, the simulation is conducted under the condition that the metallic bar is shifted from $0.1R$ to $1R$ in forward model of ECT, so the coefficient before R represents the simulated LER.

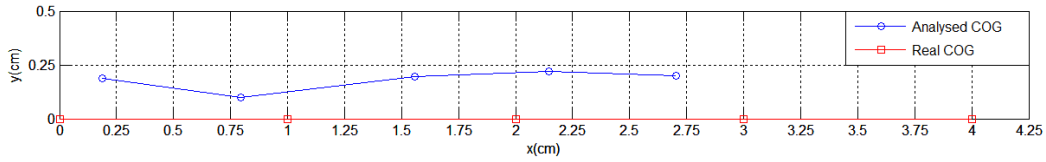

Figure 5.7: COG of the metallic bar in real and analysed conditions.

In **Figure 5.7**, in comparison to the real COG, the COG from MIT is pulled back to centre along x-axis. If the metallic bar is placed further from centre, the LER is increasingly larger. Due to the symmetric structure of MIT sensor, the shifts happened in y-axis is caused by the inevitable inaccuracy in placing the metallic bar along the x-axis during experiments. These analysed data of COG are inputted to the forward model of ECT. Subsequently the reconstruction images and the figures of merits will judge the quality of dual-modality.

5.4.3 Dual Modality Results

In this section, the forward model of ECT is separately updated with the real COG and analysed COG that is from MIT for comparison. Then ECT will reconstruct the round wooden sample, which is the red part shown in reconstruction image. To evaluate the quality of reconstruction, figure of merits is calculated. The image with threshold is plotted in the same gridding of 1000×1000 as the one in **section 5.4.1**.

Table 5.5: ECT Reconstruction images and the ones with threshold under both real and analysed location in forward model.

	Real location	**Location from MIT**
Reconstruction image	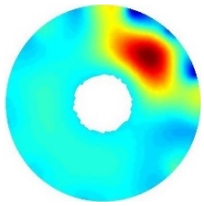	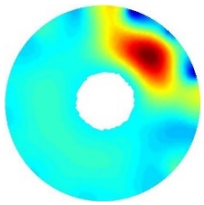
Reconstruction image with threshold	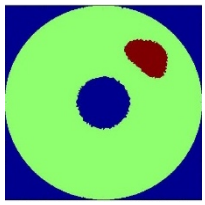	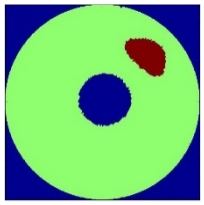
COG	**(725.3,734.7)**	**(730.6,739.5)**
RES	**20.54%**	**19.85%**
SD	**8353**	**8875**

a. Metallic bar stands at (0,0) cm

Real location	**Location from MIT**	**Real location**	**Location from MIT**
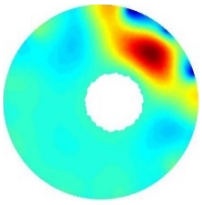	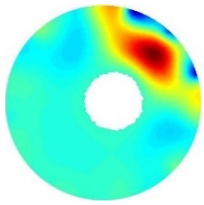	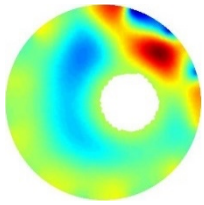	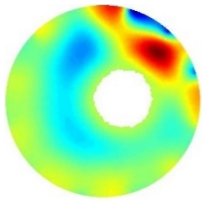
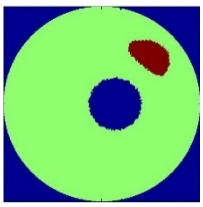	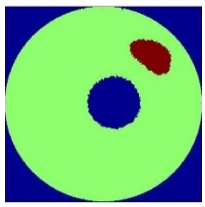	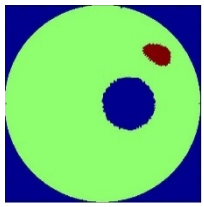	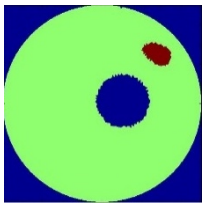
(748.5,746.2)	**(746.1,747.9)**	**(782.5,750.9)**	**(780.1,752.9)**
18.98%	**19.02%**	**12.68%**	**12.91%**
8727	**8675**	**3535**	**3443**

b. Metallic bar stands at (1,0) cm

Real location	Location from MIT
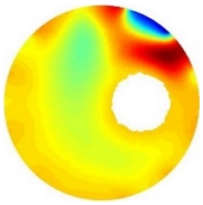	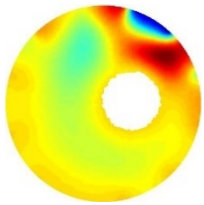
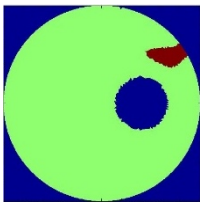	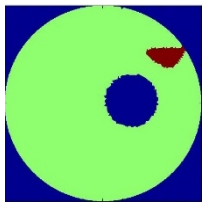
(837.1,745.2)	**(823.0,743.3)**
14.7%	**14.2%**
7120	**6154**

c. Metallic bar stands at (2,0) cm

Real location	Location from MIT
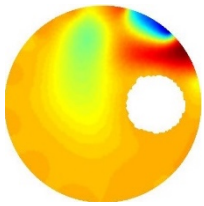	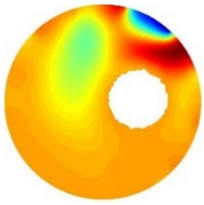
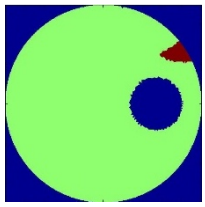	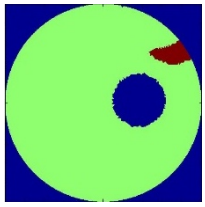
(874.0,752.9)	**(849.0,747.7)**
11.7%	**14.6%**
3638	**6697**

d. Metallic bar stands at (3,0) cm

e. Metallic bar stands at (4,0) cm

The image quality is decaying while the metallic bar is moving away from the centre, even though the forward model is defined by the accurate location of the metallic bar. However, in the analysis of result the key point is to show the difference in the quality of images between the two different forward models.

Table 5.6: The change in figures of merit from the forward model with real location to the analysed one.

	(0,0) cm	(1,0) cm	(2,0) cm	(3,0) cm	(4,0) cm
ΔCOG (unit length)	7.15	2.94	3.12	14.23	25.54
ΔRES	-3.36%	0.19%	1.81%	-3.4%	24.79%
ΔSD	6.25%	-0.60%	-2.60%	-13.57%	84.08%

Since the change in COG in **Table 5.6** is from the gridding of 1000×1000 unit length, the maximum shift of COG is only 25.54/1000=2.554% of the diameter of the imaging region,

which is very small. The change in RES and SD stays in a low percentage until the metallic bar is placed at (3, 0) cm. From the images in **Table 5.5 (d)** and **(e)**, with the real forward model applied, the reconstruction of round wooden stick has seriously deformed, therefore the factor of SD is not accurate enough. When the reference image is largely deformed, it is not applicable to use SD to describe the image quality and the 84.08% change in SD cannot express the real change in the image as we can see in **Table 5.5(e)**.

5.5 Summary

The purpose of this chapter is to introduce a new method for ECT imaging with ground conductors assisted by the MIT imaging. The dual-modality can detect the existence of highly conductive sample and use the location information to improve the image reconstruction of ECT. The simulations and the experiments are conducted in various imaging scenarios, and the images are assessed by figure of merits: COG, RES and SD. The result from dual-modality tomography is promising and can be applied to test complex samples with metallic and dielectric material. For example, detection cracks in reinforced concrete, where reinforcing steel bars in concrete is highly conductive and electrically grounded. Depending on location of the metallic object, the ECT forward problem needs to be solved and an updated sensitivity map needs to be generated. In dynamical imaging situations where online image reconstruction may be needed further work is needed to speed up the computational time, in particular those of the ECT system. For purpose of this study an ECT system and an MIT system was used, a future hybrid ECT–MIT system can be developing allowing for some sharing hardware and structure, which can help reduce the cost of hybrid system. In our future study we will extend the dual modality ECT, MIT imaging by adapting a complex impedance forward and inverse model for ECT where we can deal with floated conductors as well as low conductivity inclusions such as water contents.

Chapter 6 **Low Conductivity MIT-ECT**

6.1 Introduction

In last chapter, we used MIT to find metallic component, which is still very challenging and not very well established the same as ECT. For MIT detecting metallic samples, the amplitude of induced voltage over sensing coil is the measurement of interest. But for low-conductivity sample, like conductive water, the amplitude change of the induced voltage is extremely small. In this case, therefore, the phase difference in the measurements is used to capture the information of conductive component. Currently there is not a robust and real time MIT data acquisition for low conductivity industrial process applications reported yet. The phase accuracy required for MIT low conductivity imaging poses a challenge in electronic hardware design of MIT as well as its shielding and sensor front end. The forward problem in MIT is a complex eddy current problem compared to well-understood elliptic partial differential equations describing the ECT forward modelling. Here we propose to use MIT as a complementary technique for the ECT in a sequential data fusion scheme for low conductivity applications.

In [85], electrical impedance methods has been used in the three-phase flow measurement to provide electric resistance and capacitance for calculating the oil, gas and water fractions. Normally the three-phase flow is mixture of gas, oil and water. The relative permittivity of each phase are different:$\varepsilon_{gas} \approx 1$, $\varepsilon_{oil} \approx 2-3$ and $\varepsilon_{water} \approx 80$. The permittivity difference is very small between gas and oil but very large between water and gas or oil. Therefore, this becomes a problem of ECT imaging in distinguishing oil from gas. In addition the electrical conductivity of the water phase will be a challenge for ECT modelling. In petroleum industry, to decrease the difficulty of three-phase flow, a separator is used to free the gas and the rest two-phase flow of oil and water is monitored. To provide a solution to determine the fraction of each phase without using a separator, which would saves cost on a separator, some dual-modality

tomography are proposed. In [78, 86], ERT is combined with ECT as a dual-modality solution. ERT generates an image that can discriminate gas (*i.e*. low conductivity) from mixture of oil and water (*i.e*. higher conductivity than gas), meanwhile an image from ECT distinguish water (*i.e*. high permittivity) from the mixture of gas and oil (*i.e*. low permittivity). And in [80, 87-90], the gamma radiation meter (GRM) are introduced to determine the fraction of gas from liquid (*i.e*. water and oil), similar to what is obtained from ERT. Then by fusing the images from ERT or GRM with ECT images, the distribution of three-phase flow is visualized. The data fusion method used in these dual-modalities is basically to merge the two separate images from ECT and ERT reconstruction. However ERT needs electrical contact between the sensors and the sample under test, and GRM takes a long time for measurement acquisition. By contrast, both ECT and MIT have advantages of no direct contact to the sample under test and fast speed on data acquisition and image reconstruction.

The dual modality of MIT-ECT is firstly introduced in [71], where an MIT guided ECT modality is proposed to solve the problem of effect from the grounded conductor in ECT. Unlike the data fusion used in ERT-ECT, MIT-ECT works in a sequential process. MIT is a method to obtain the information of the conductive water and to feed the information to the forward model of ECT, since the water with conductivity is also of high permittivity. The prior information helps to linearize the high contrast problem in ECT by producing a reference measurement (model) closer to the two low permittivity phases. Then ECT will image the rest parts in the sensing area. The focus of this chapter is mainly to solve high contrast ECT problem aided by MIT, and that is currently being extended to imaging conductive background where major modification in ECT software will be needed.

6.2 Methodology

6.2.1 Forward Model

A typical ECT sensor usually consists of 8 or 12 electrodes, which is designed to measure the

capacitance of the material under test [91]. And in a measurement, one of the electrodes is excited by a given voltage and the rest electrodes are grounded to receive signal of current. Outside of an ECT sensor, normally a screening wall is used to shield the effect from external electric field. From Maxwell's equations, the relationship between permittivity and conductivity distribution $\varepsilon(x)$, $\sigma(x)$and electrical potential $u(x)$are in the following way within the region, where

$$\nabla \cdot \left[\varepsilon(x) + \frac{\sigma(x)}{j\omega}\right] \nabla u(x) = 0 \tag{6.1}$$

And the boundary conditions of this problem are the electric potential $u(x)$ on different surfaces of the sensors, as shown in equation **(3.4)** and **(3.5)**.

The electric charge on the l-th electrode is generated from the Gauss's law, as shown below.

$$Q_l = -\int_{\Gamma_l} \left[\varepsilon(x) + \frac{\sigma(x)}{j\omega}\right] \frac{\partial u(x)}{\partial n} d\Gamma \tag{6.2}$$

where n is the normal vector on an electrode. This leads to a complex capacitance measurement, which has information about both electrical conductivity and dielectric permittivity. The sensitivity of this complex capacitance (if it can be measured), to each of these two electrical properties depends on our ability to measure accurately real and imaginary parts of the capacitance as well as operational frequency.

6.2.2 Inverse Problem

To convert the measurements into an image of permittivity or conductivity distribution, we need reconstruction algorithms to solve this inverse problem. A standard Tikhonov

regularisation used here:

$$\Delta x = (S_k^T S_k + \gamma I)^{-1} S_k^T M \tag{6.3}$$

where Δx is the proper distribution change, it can be permittivity for ECT or conductivity for MIT. S is the sensitivity map, and M is difference in measurements. γ is the regularisation factor.

6.2.3 Improve Reference Point for ECT Reconstruction

To reconstruct ECT images, the key inputs to the inverse solvers are the sensitivity map and the differences between measurements. And these two inputs are related to the selection of reference point. If oil and water samples are placed into an air-filled ECT sensor, then the relation between measurements, sensitivity maps and permittivity distribution is expressed in **Figure 6.1**.

C_{air}:	**The capacitance measurements of air-filled sensor**	ε_{air}:	**The permittivity distribution of air-filled sensor**
$C_{air+water}$:	**The capacitance measurements of the sensor containing air and water**	$\varepsilon_{air+water}$:	**The permittivity distribution of air and water**
$C_{air+water+oil}$:	**The capacitance measurements of the sensor containing air, water and oil**	$\varepsilon_{air+water+oil}$:	**The permittivity distribution of air, water and oil**
S_{air}:	**The sensitivity map of air-filled sensor**	$S_{air+water}$:	**The sensitivity map of air and water**

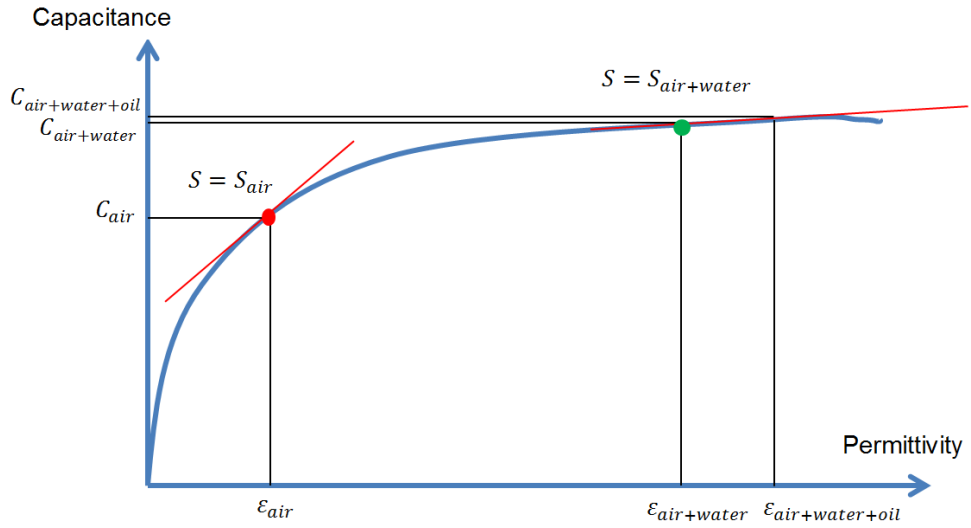

Figure 6.1: The non-linear relationship between capacitance and permittivity in ECT (air-background).

The schematic way of non-linear relationship between capacitance and permittivity in ECT is extended from [55]. Normally to detect an unknown distribution in ECT, the empty sensor is used at a reference point, *i.e.*, the red point, where the sensitivity map $\boldsymbol{s_{air}}$ and capacitance measurement $\boldsymbol{c_{air}}$ is obtained from a purely air-filled sensor. In a multi-phase problem, to image the rest two phases within the ECT sensor is hard, since water is of high permittivity and increases non-linearity in reconstruction. To linearize the problem, a reference point include the water phase is selected. Instead of the red point, the green point contains the information of both air and water is closer to the real distribution and assists the inverse solver to find the oil phase easier.

The capacitance measurements for the green or red points are obtained straight from measurement machine. To investigate the changes in sensitivity maps, the three phases are categorized into two basic and simplified scenarios: **1. Air background**, where a bottle of water is inserted; **2. Water background**, where a bottle of air is inserted. In **Table 6.1**, the sensitivity maps between a pair of opposite electrodes are plotted. This ECT model is made of 12 electrodes, which evenly mounted on periphery of a pipe wall (relative permittivity of wall is

$\varepsilon_{wall} \approx 3$). And the external radius of the pipe is in 100 mm, and the thickness is 5 mm, and the radius of the bottle is 29 mm.

For air background, the sensitivity increases on the region of a bottle of water; but it decreases on the region of a bottle of air for water-background case. In **Table 6.1**, both the colour and the height on z-axis indicate the value of sensitivity. Those images show the change in sensitivity. This will help to find the third phase of oil in a three-phase problem.

The water in the three-phase problem is not only of high permittivity but also of conductivity. So MIT is introduced to image the conductive water from air and oil before ECT senses the unknown region to obtain the green point in **Figure 6.1**. Thereafter ECT utilizes the new information of water from MIT to shift the linearizing point from red to green. And the ECT reference data is also changed from the measurements of the air-filled sensor to the measurements of the sensor containing both air and water. At the final stage, the capacitance measurement of air, water and oil is processed to visualize the oil component.

Table 6.1: The sensitivity maps between two opposite electrodes in the ECT sensor.

	Air-background	
	Free space	**A bottle of water sits in the sensor**
Schematic diagram	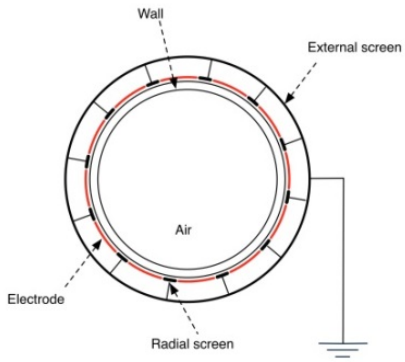	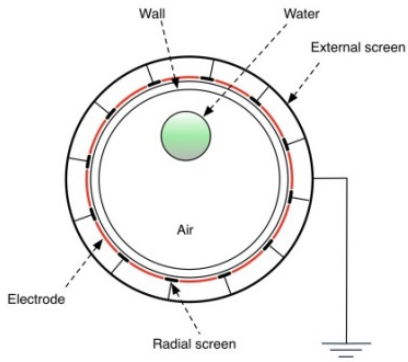
Sensitivity map of sensing region	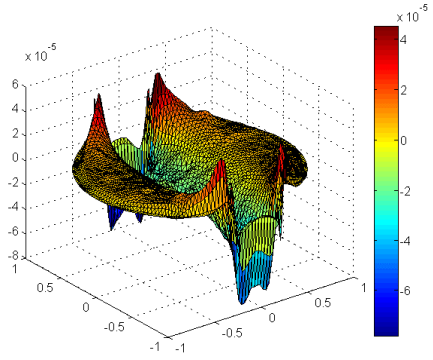	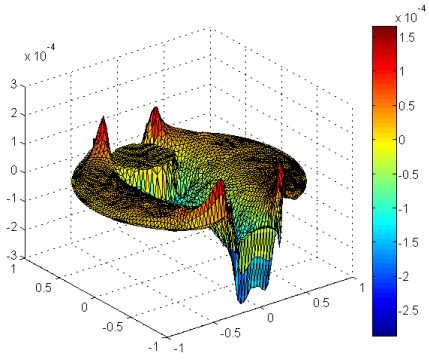
	Water-background	
	Fully water-filled sensor	**A bottle of air sits in the water-filled sensor**
Schematic diagram	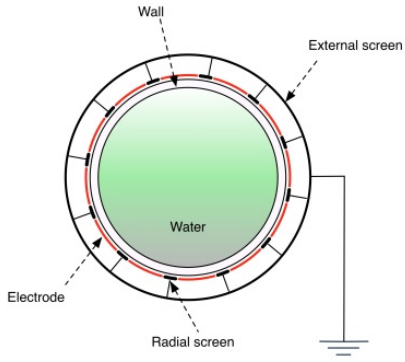	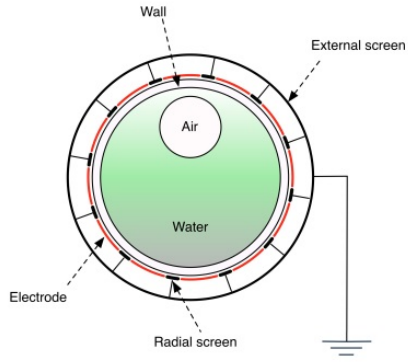

Sensitivity map of sensing region	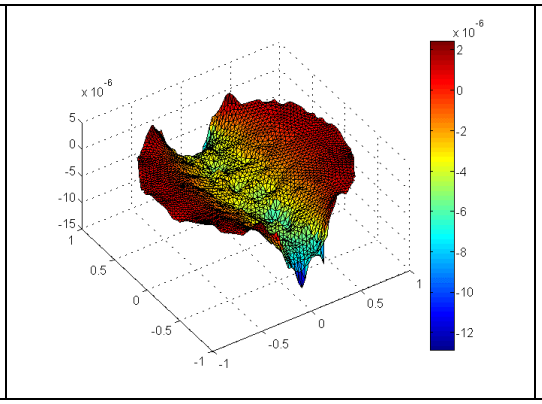	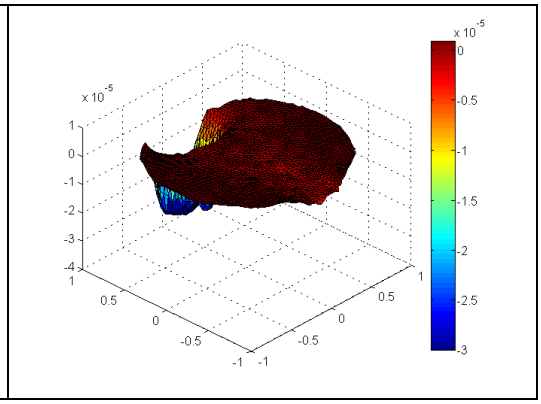

6.2.4 Sequential Dual Modality Procedure

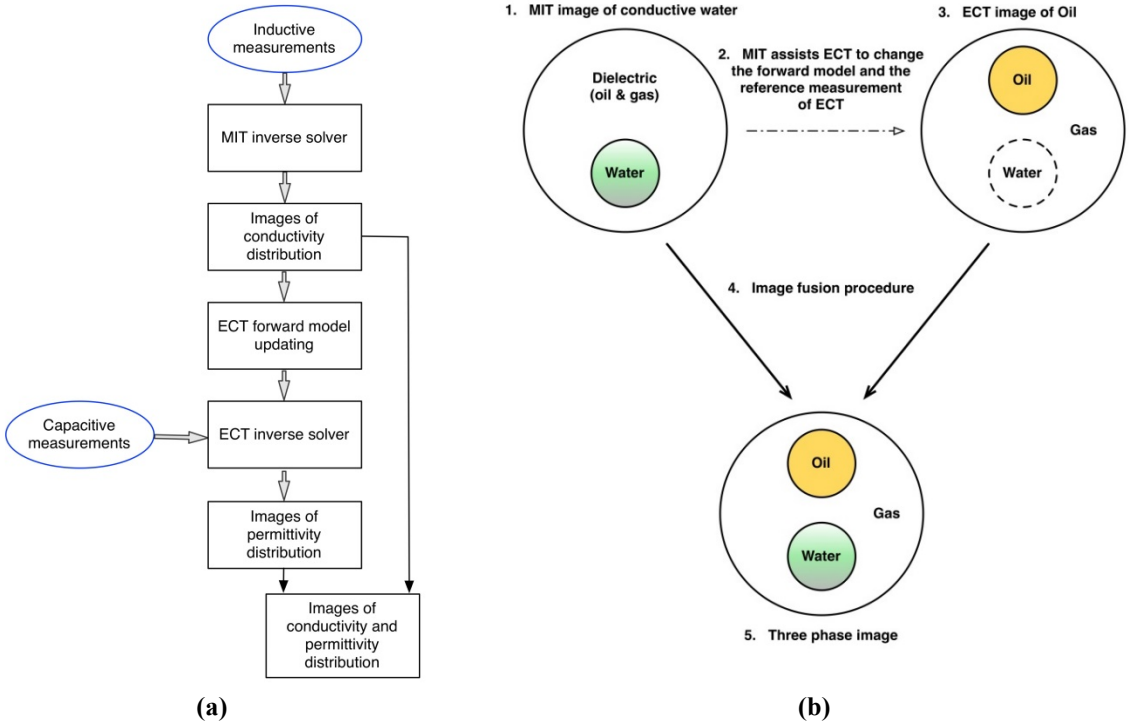

Figure 6.2: (a) Working flow chart of dual-modality; **(b)** Fusion of the two tomograms.

Firstly in MIT system, by solving the difference in inductive measurements, an image of conductivity distribution is reconstructed, as shown in the step 1 of **Figure 6.2(b).** The ECT forward model and the set of capacitance measurements under this condition are acquired for this sequential procedure. To update the forward model, we assign the relative permittivity of

80 to the designated region of water in ECT forward model. To obtain the capacitance measurement, we replace the experiment samples according to the images got from MIT and collect the measurement.

Then ECT reconstructs permittivity distribution of the rest area apart from the water, therefore the oil and gas phase can be discriminated. The final stage is to merge the two images and generate a three-phase image. This procedure is also explained in the flow chart, **Figure 6.2(a)** and the fusion of the two tomograms are shown in **Figure 6.2 (b)**.To be noticed, MIT uses the inductive measurement and sensitivity map of air-filled MIT sensor as the reference point to find the conductive water component.

6.3 Setting Up of Experiments and Simulation

6.3.1 Equipment Description

Table 6.2: MIT sensor and measurement unit.

	
(a) MIT sensor	**(b) MIT measurement unit**

The Bath MIT system consists of a coil array of equally spaced 16 air-core sensors, a National Instrument (NI) based data acquisition system and a host computer (Table 6.2 a and b). The sensing zone has a diameter of 25 cm. Each coil has 6 turns, a side length of 1 cm, and a radius of 2 cm. The coil resonance frequency is 45 MHz. This system was designed to measures the phase change caused by imaging substances and uses that change for image reconstruction.

Among 16 coils, 8 coils are dedicated for transmitting signals, and the remaining 8 coils are used for receiving signals. The total number of independent measurements is therefore 64. Noting that the neighbouring measurements are eliminated to reduce the capacitive coupling effect between the excitation and receiving coils, therefore 48 measurements are used in the inverse model to passively map the distributions of the imaging subject. Furthermore, this system operates in MHz range in attempt to increase the signals, a common practice for MIT systems designed for biomedical and industrial process applications. Low frequency MIT can only be used for imaging highly conductive metallic samples. The detailed measurement system design has been reported in [47]. Inside the sensor, a circular tank is used to hold water for future experiment. The external diameter of the tank is 20 cm with a thickness of 0.5 cm.

Table 6.3: ECT sensor.

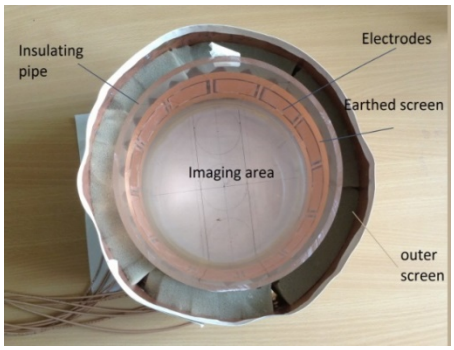

The ECT sensor consists of 12 copper electrodes mounted on the pipe of the same size as the tank in the MIT sensor. Each electrode in the size of 45 mm*40 mm is evenly distributed on the periphery. For the purpose of screening, there is a thin piece of copper between neighbour electrodes and two circular strips of copper are separately mounted above and below the sensing electrodes. The ECT measurement system in our laboratory is the PTL 300E.

In our static experiments, bottles of saline water ($\varepsilon_{water} \approx 80$), silicone oil ($\varepsilon_{oil} = 2.5$) and air ($\varepsilon_{air} = 1$), are samples to simulate the three-phase flow. The radius of bottle is 29 mm.

6.3.2 Simulation for Conductivity in ECT

In **section 6.4**& **6.5**, experiments conducted in the two scenarios (*i.e*., air or water background) attempt to tell the feasibility and the limitation of each tomographic modality and the combined dual modalities. Generally, ECT is designed to test the dielectric material, but in our experiment the conductivity is introduced, as it is factor from the water component in three-phase flow. Therefore before applying ECT to the scenario of conductive water, the impact of conductivity on capacitance measurement should be investigated by both simulations and experiments.

In our experiments, sodium chloride (NaCl) is added into water to increase the conductivity, the permittivity of the solution changes as well. In [92], the permittivity changing as the concentrations changing in NaCl solution has been elaborated. And from [92], the relative permittivity change drops from 80.5 to 78.3 when we increase the concentration of saline water from 0 to 50 g/L at 20 °C. Since the permittivity change is very small within the concentration range of our experiments, the relative permittivity of water is fixed at 80 while the conductivity increases in our forward model.

The simulation of ECT is based on a noise-free complex-permittivity model. As shown in equation **(6.2)**, the conductivity is the imaginary part of the complex permittivity. All of the bottles used in the simulation are 29 mm in radius, and the sensor pipe is 100 mm in external radius and 95 mm in internal radius. The relative permittivity of the sensor pipe is 3. To match the real experiment, the simulation model works in the same frequency as the PTL 300E-3D equipment, which is f=1.25 MHz.

6.4 Air Background

6.4.1 Impact of Conductivity on Capacitance Measurement

6.4.1.1 Simulation Results

A bottle of water standing in the centre of the sensor is measured as the reference. A bottle of oil is placed at (0, 65) mm for the sample measurement. While increasing the conductivity of water from 0 to 5 S/m in both cases, the capacitances data are collected. In each single set of capacitance measurements, there are 66 capacitances between 12 electrodes. And the measurements are in complex value. To indicate the trend of capacitance change, the 2-norm values of each set of 66 capacitances are used. In the third row of Table 6.4, the difference between the two measurements is $\|\mathrm{C}_s - \mathrm{C}_r\|_2$, which means the norm value is obtained after the subtraction.

Table 6.4: 2-norm of simulated capacitance changes when conductivity increases from 0 to 5 S/m (air background).

Reference measurement $\|\mathbf{C}_r\|_2$	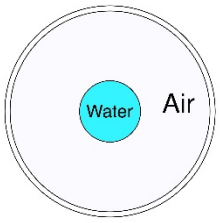	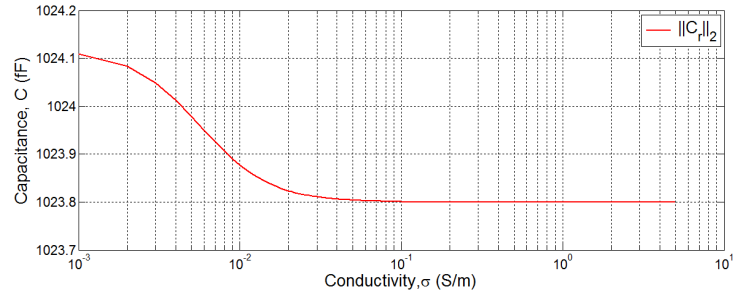
Sample measurement $\|\mathbf{C}_s\|_2$	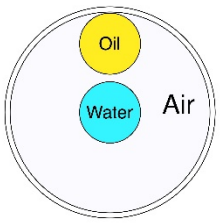	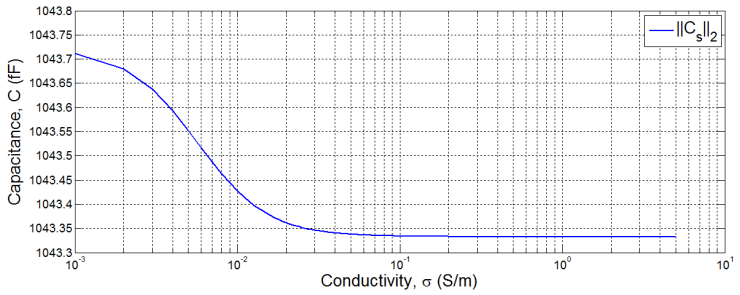

Difference of the measurements above $\|\mathbf{C}_s - \mathbf{C}_r\|_2$	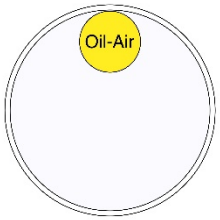	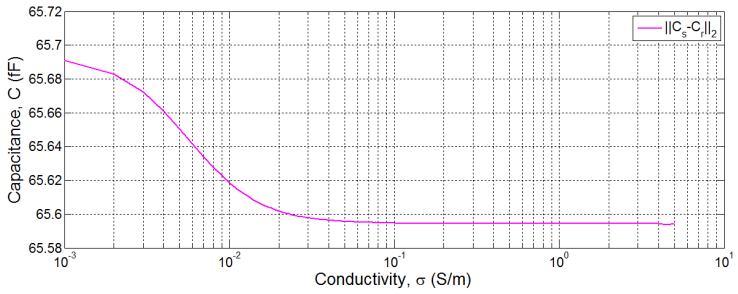

From the simulation, the capacitance value changes in a small range: from 1023.8 to 1024.1 for reference measurement, from 1043.3 to 1043.7 for oil and water measurement. The capacitance change, *i.e.* the difference of two measurements, is the input for ECT reconstruction. The increasing conductivity causes small effect on the capacitance difference from 65.59 to 65.69. According to the simulation of air background, the interference from a bottle of conductive water is very small for the ECT testing. Therefore, the conductivity in air background does not affect the capacitance measurement.

6.4.1.2 Experiment Results

The simulation indicates that the conductivity of the water in a bottle makes a minor impact on the capacitance measurement. Experimentally, several bottles filled with saline solution of different concentration are individually placed in the centre of the sensor and the data of capacitances is measured. Table 6.5 are conductivities of different solutions measured by the Jenway 4510 conductivity meter. The bottle is placed in the centre of the sensor, and the according capacitances are measured. The outer radius of the bottle is 29 *mm*. The capacitance change from air background is plotted out in **Figure 6.3**. In **Figure 6.4**, the 2-norm values of capacitances of different solutions are listed.

Table 6.5: Conductivity of different solutions.

Test material	Conductivity
9 *g/L* saline solution	**1.557 S/m**
30 *g/L* saline solution	**4.68 S/m**
50 *g/L* saline solution	**7.07 S/m**
Tap water	**0.0586 S/m**
DI water	**0.0003 S/m**

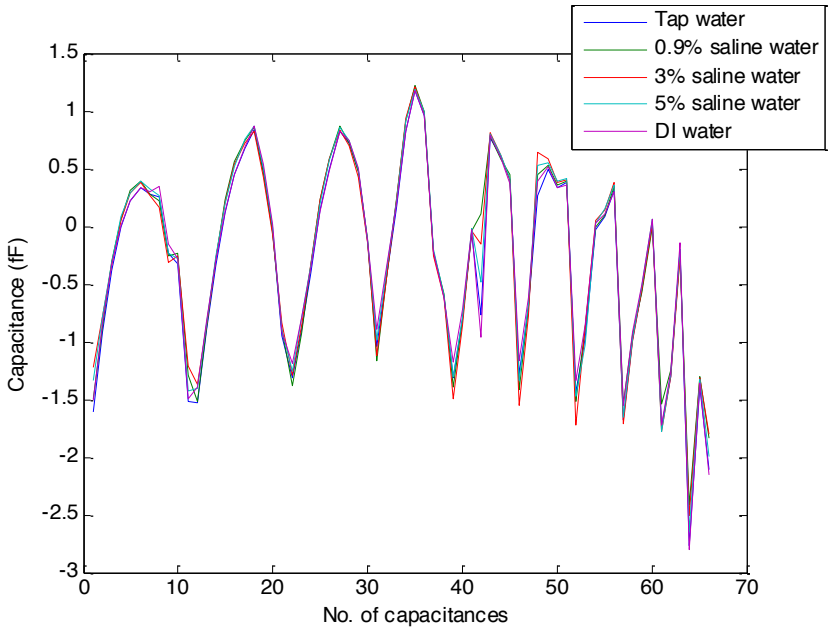

Figure 6.3: The plot of capacitance differences from air background.

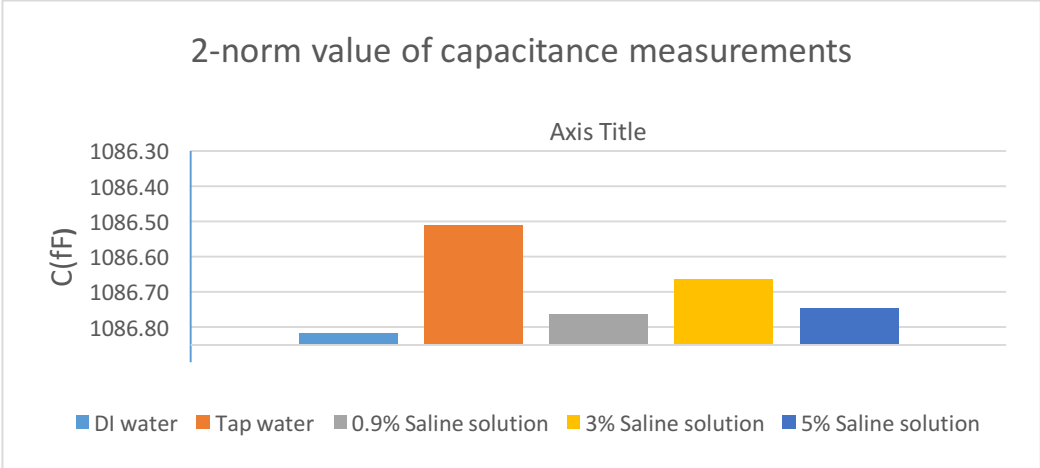

Figure 6.4: The 2-norm value of each set of measurements.

Figure 6.4 indicates the minor impact of conductivity on the capacitance measurements, which matches the simulation. These results help us to move forward to next step of ECT experiments.

6.4.2 Dual Modality Test

6.4.2.1 Positions and Concentration of Samples in Air

In the experiment, we use the 3% and 5% saline solution and the silicone oil as our samples. Each time, only two bottles are placed in the sensor: one filled with saline solution and the other filled with silicone oil. The position arrangement of the samples is shown in Table 6.6. In position 1, one bottle sits at top of coordinate (0 mm, 65 mm) and the other sits at bottom of coordinate (0 mm, -65 mm). In position 2&3, one bottle sits at centre (0 mm, 0 mm), the other is placed at top of coordinate (0 mm, 65 mm).

Table 6.6: Positions of the samples in air.

Position 1	Position 2	Position 3
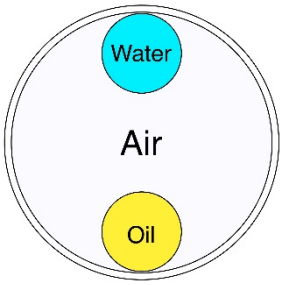	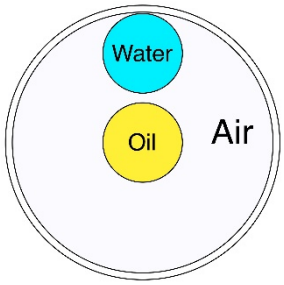	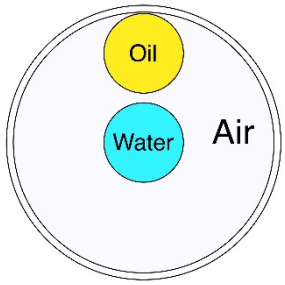

6.4.2.2 MIT Experiments

Table 6.7: MIT images of different position and concentrations of saline solution.

	Position 1 & 2	Position 3
3% saline solution	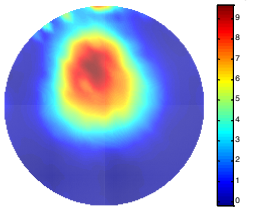	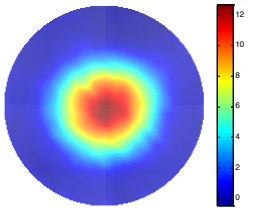

5% saline solution	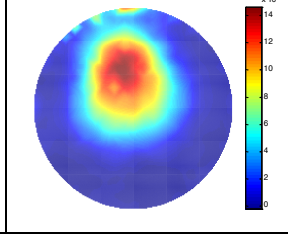	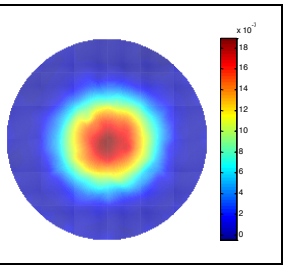

The conductivity of both oil and air is closed to zero, so the major detectable component in MIT is the saline solution. Therefore in both case of Position 1 and 2, the images are the same. The experiment results are shown in **Table 6.7**.

6.4.2.3 ECT Experiments

By obtaining the MIT results, the position and size information will be inputted to the ECT forward mode. In current stage of study, we only feed the position information to the ECT forward model, and set the water component as a circular region of diameter 56 *mm*. After that, ECT reconstructs images with prior information of the water. The ECT experiment results are listed in **Table 6.8**. The images shown are the permittivity distribution. When MIT information is introduced into the ECT, the conductive component (*i.e.* water) is not visualized in the ECT images. To obtain a complete image of the three components, MIT and ECT images will be merged. In **Table 6.8**, the DI water is used as a reference sample to be compared with the conductive water. The non-conductivity of DI water disables the detection of MIT. Therefore, "N/A"s in the table mean that MIT-ECT cannot be applied to the completely non-conductive samples.

Table 6.8: The images from ECT-only and MIT-ECT system.

Position number	Modality	DI water & oil	3%saline solution & oil	5%saline solution & oil
1  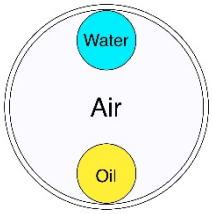	ECT	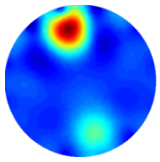	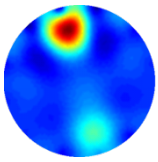	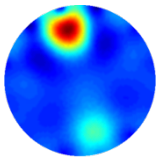
	MIT-ECT	N/A	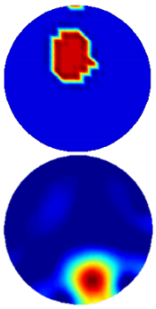	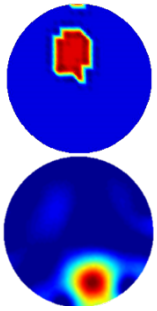
2  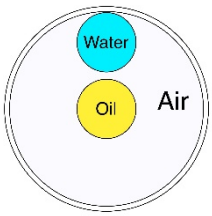	ECT	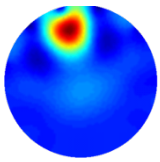	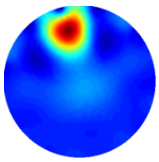	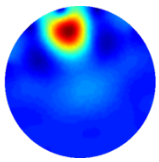
	MIT-ECT	N/A	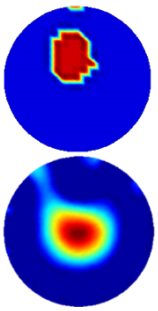	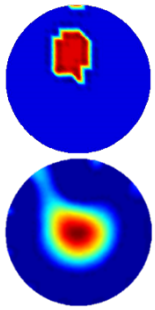
3  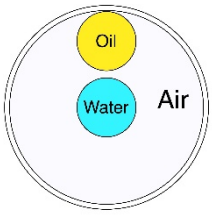	ECT	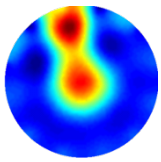	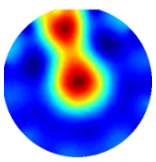	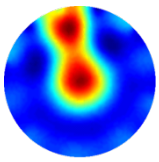
	MIT-ECT	N/A	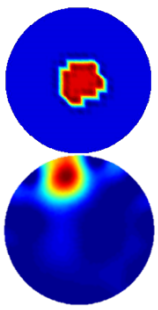	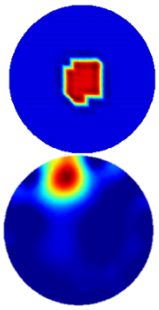

ECT is able to distinguish the high permittivity from the low. When both the oil and the water sit near the electrodes, the reconstruction images tell the different permittivity of oil and water. However, when the water and the oil are placed closely together, the information from the images become difficult to read: (a) when the oil is facing the electrode, the image cannot distinguish which is of higher permittivity; (b) when the water is facing the electrode, the oil placed in the middle can hardly be recognized from the ECT image. MIT helps to find the conductive components (*i.e*. the saline solution), which provides prior information to assists ECT to image the rest region in the sensing area. With the help of MIT, ECT can distinguish the oil from the air, even though the water is closed to the oil. In **Table 6.8**, on the rows of MIT-ECT, the images on the top are the MIT images of the water inclusion, which is obtained by apply a threshold of 70% to the images in **Table 6.7**.The MIT-ECT dual-modality provides a better solution to separate oil from water in the three-phase flow imaging than ECT-only.

6.5 Water Background

6.5.1 Impact of Conductivity on Capacitance Measurement

6.5.1.1 Simulation Results

Firstly, the sensor region is filled with water, where the capacitances measured are the reference measurements, C_r. Then a bottle of air and a bottle of oil are placed in our simulation model, where the sets of capacitances measured are the sample measurements, C_s. The 2-norm values of each set of 66 capacitance measurements are plotted along the conductivity change in the table below.

Table 6.9: Simulated capacitance changes when conductivity increases from 0 to 5 S/m (water background).

Reference measurements $\|\mathbf{C}_r\|_2$	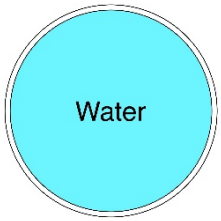	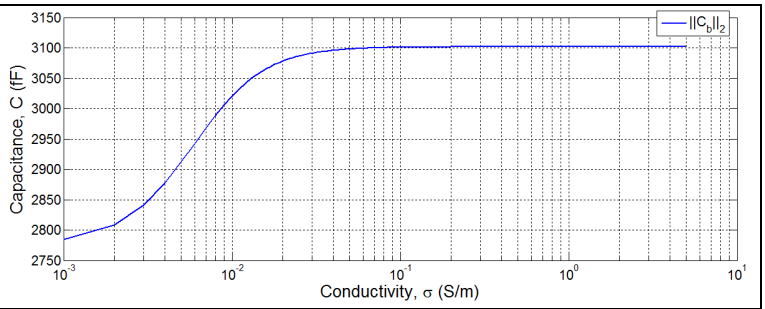
Sample measurements $\|\mathbf{C}_s\|_2$	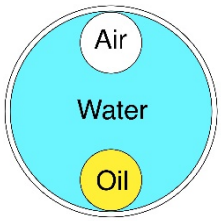	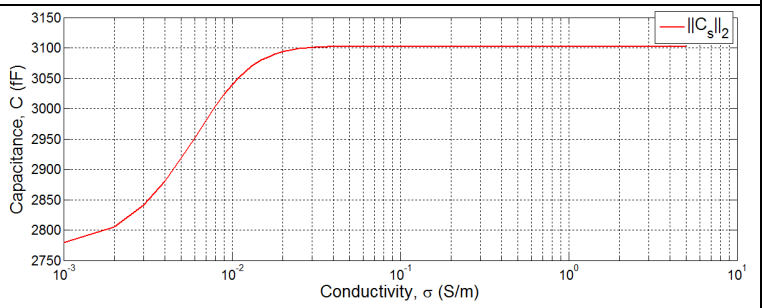
Difference of the measurements above $\|\mathbf{C}_s - \mathbf{C}_r\|_2$	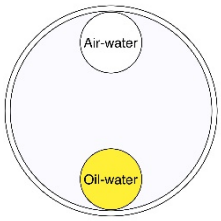	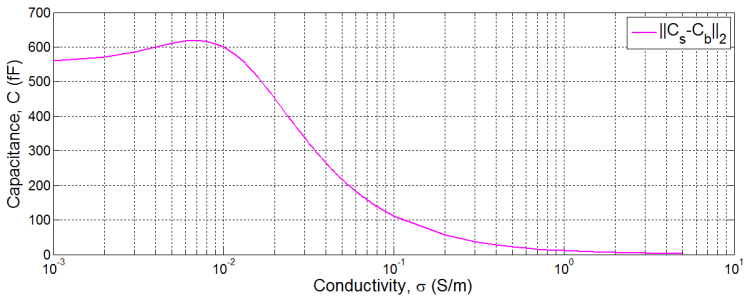

For image reconstruction, the difference of the measurements determines the quality of the image. In the third column of **Table 6.9**, the value of the difference drops rapidly to approach the 0, which is much smaller than the value of low conductivity, *i.e.*, less than 0.5 S/m. The big change in the 2-norm value of the difference value causes decline in image quality. Several points within the conductivity range from 0 to 0.1S/m are selected to reconstruct the images, and the capacitance measurement of the 5S/m is also shown in **Table 6.10**.

Table 6.10: ECT images reconstructed by the selected simulated capacitance (water background).

2-norm value plot along σ changes	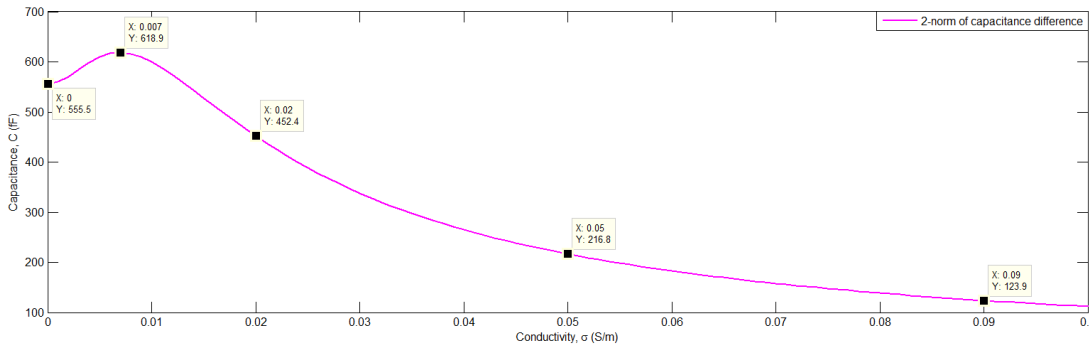		
σ (S/m)	**0**	**0.007**	**0.02**
ECT images	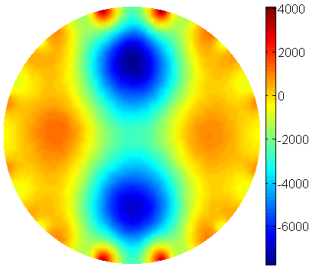	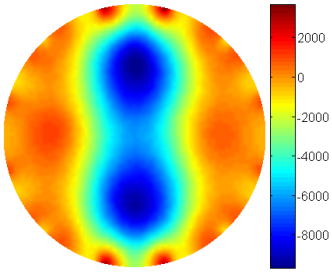	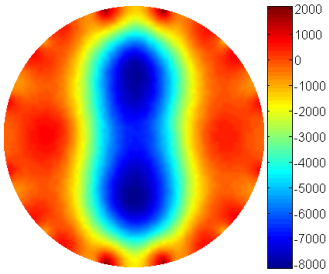
σ (S/m)	**0.05**	**0.09**	**5**
ECT images	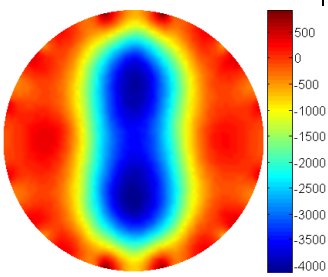	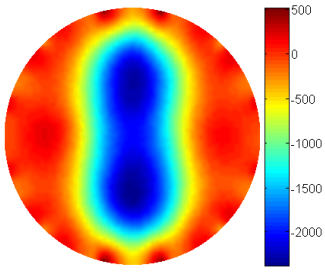	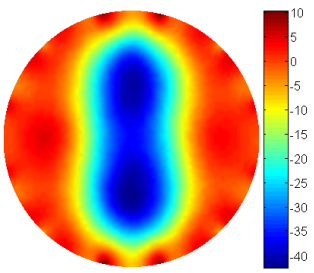

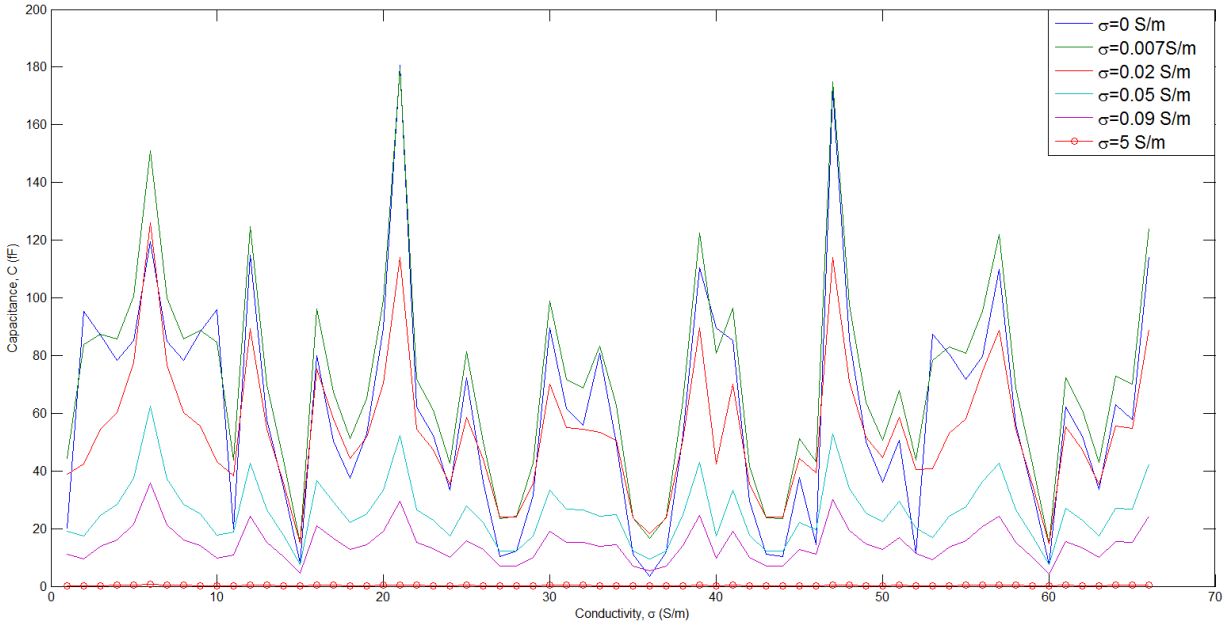

Figure 6.5: Six sets of inter-electrode capacitances change, $|C_s - C_r|$, from simulation.

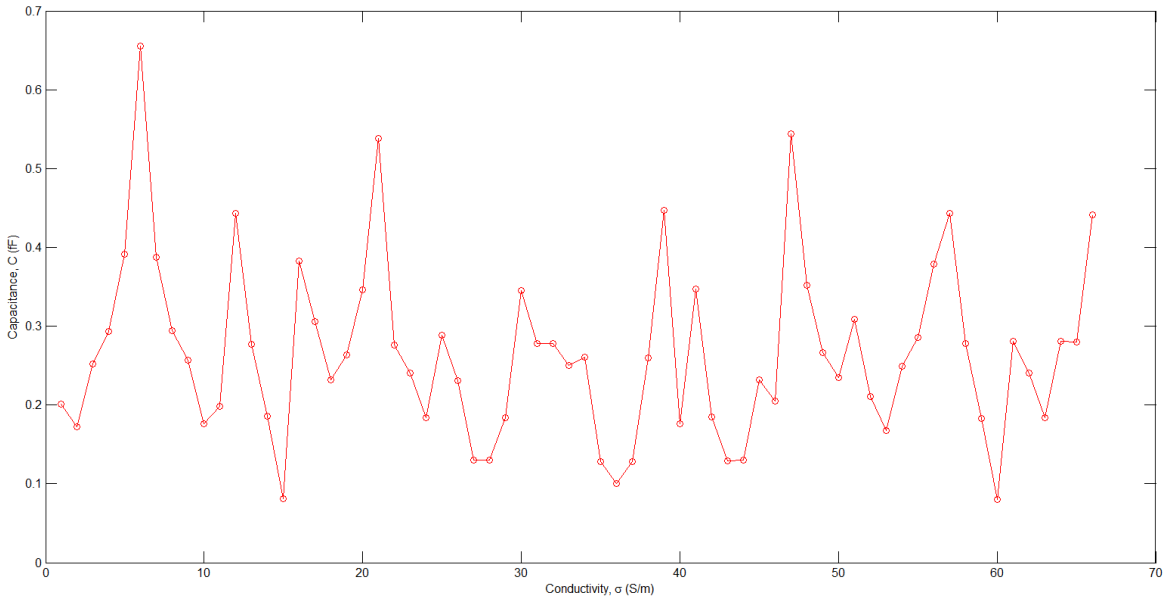

Figure 6.6: Inter-electrode capacitances change, $|C_s - C_r|$ when conductivity is 5 S/m.

The simulated inter-electrode capacitance changes at 6 selected values of conductivity are plotted in **Figure 6.5**. As the conductivity increases, the capacitance difference declines and is

less sensitive to permittivity distribution. However in **Figure 6.6**, the profile of these plots remains very similar, even the conductivity reaches 5 S/m. Therefore, the reconstruction image at 5 S/m indicates a very similar pattern to the one at 0.09 S/m. But calculated permittivity values of each case are in difference scale, which can be found by the colour bars in **Table 6.10**.

6.5.1.2 Experimental Results

The bottom of the sensor pipe is sealed, so it can be filled with water for this test. The experiment starts with measuring DI water ($\sigma_{DI} = 2.87\times10^{-4} S/m$). Then the conductivity is increased to 0.5450 S/m by adding high-concentration saline water slowly and gradually. Both conductivity and the inter-capacitance are measured and recorded. For the capacitance measurements, as the simulations in **Table 6.9**, the water-filled sensor is measured as the reference, C_r; the bottles of air and oil are placed at top and bottom within the sensor region are the sample measurement, C_s. In **Figure 6.7**, the 2-norms of the capacitances difference are plotted.

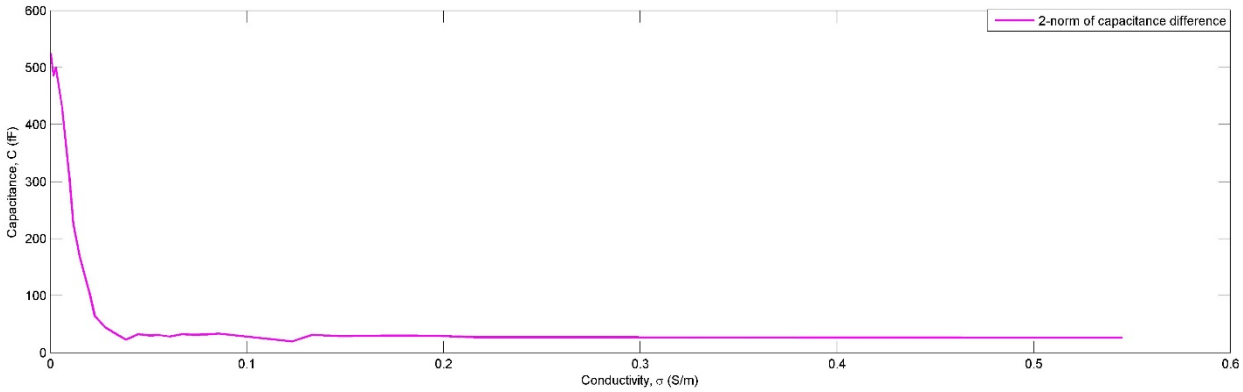

Figure 6.7: 2-norm of the capacitance measurement difference between reference and samples, Cr-Cs.

To compare with images reconstructed from simulated measurements in **Table 6.10**, the experimental measurement are calculated and the images are plotted in **Table 6.11**. The points close to the one selected in **Table 6.10** are chosen. And the imaging fails around $\sigma = 0.3$ S/m

and an image at the 0.5450 S/m is shown at the end of **Table 6.11**.

Table 6.11: ECT images reconstructed by the selected measured capacitance (water background).

2-norm value plot along σ changes	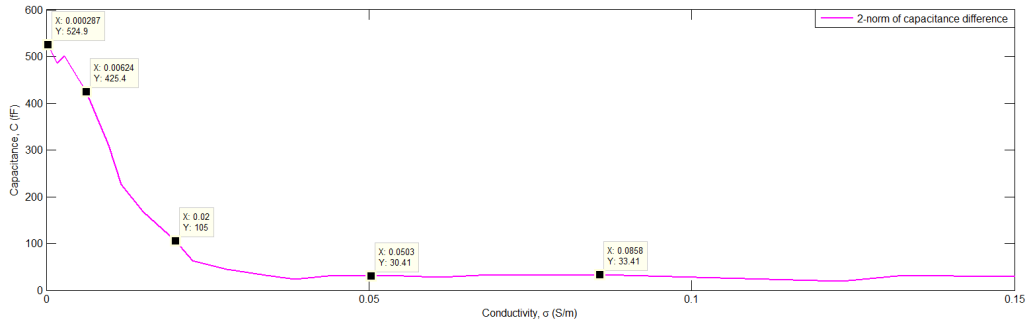		
σ (S/m)	**0.0003**	**0.0062**	**0.0200**
ECT images	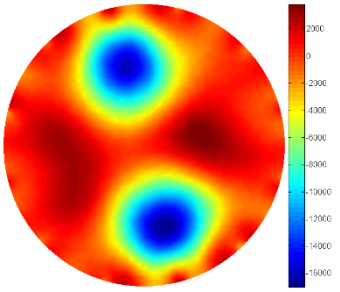	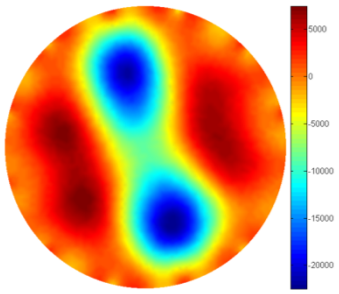	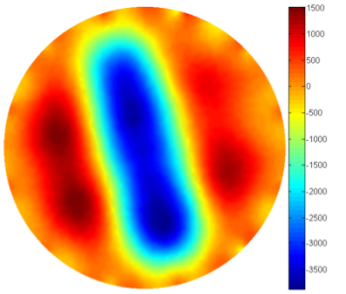
σ (S/m)	**0.0503**	**0.0858**	**0.5450**
ECT images	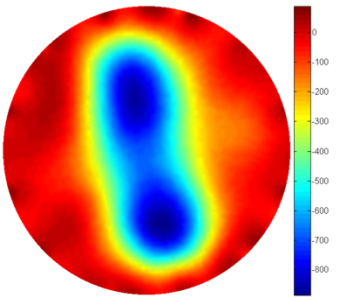	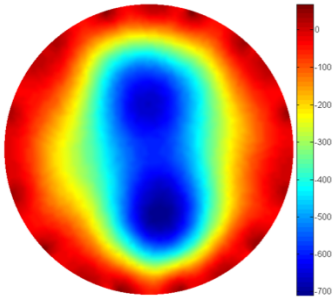	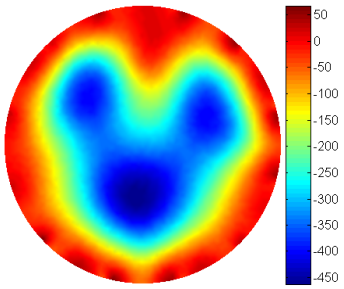

6.5.2 Dual Modality Test

6.5.2.1 Positions of Samples in Water

The conductivity of the water background are chosen as 0.863 S/m and 1.557 S/m (9% saline water). The other two-phase flow is simulated by a bottle of silicone oil and a bottle of air. The

samples are placed in the positions below in **Table 6.12**.

Table 6.12: Positions of the samples in water.

Position
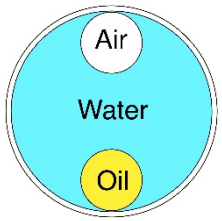

6.5.2.2 MIT Experiments

The conductivity difference between the background and samples determines the ability of MIT to image the dielectric from the conductive inclusions. From our experiments and observation, when the conductivity of the water background is lower than 0.5 S/m, the MIT images starts deforming, and our MIT system reaches its limitation of detecting non-conductive samples from conductive background. The table below shows some results of MIT imaging when the conductivity is higher than 0.5 S/m.

Table 6.13: MIT images of air and oil samples under difference conductive background.

	0.863 S/m	1.557 S/m
MIT images	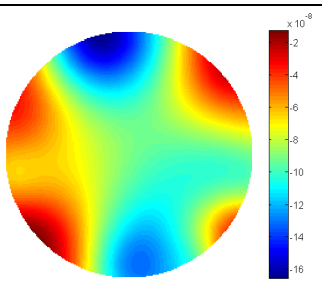	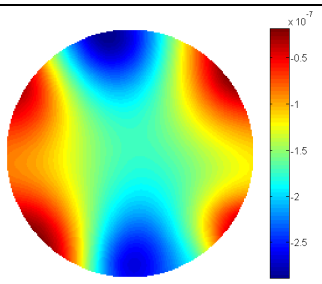

6.5.2.3 ECT Experiments

The images of ECT under different conductivity water background are listed in **Table 6.14**. The letter "r" in the table is the regularisation parameter in Tikhonov algorithm, and the images on the same column are calculated by the same settings of Tikhonov parameters. In the column

of **ECT (air reference)**, the air-fully-filled sensor is measured as a reference measurement. ECT can only image the two low-permittivity inclusions clearly under the DI water background. As the conductivity goes a little bit higher, the reconstruction image fails. In the column of **ECT (water reference)**, the water-fully-filled sensor is measured as a reference measurement, which is changing as the conductivity changes. The image quality deteriorates while conductivity increase, but it performs better than the air reference.

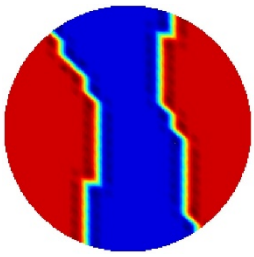

Figure 6.8: Binary image of threshold of 55% of the maximum value over the MIT image.

However, due to the limitation of our current equipment, the conductivity contrast lower than 0.5 S/m cannot be imaged by MIT.

Therefore we use the images of the conductivity contrast of 1.557 S/m from **Table 6.13** as a guidance to modify the sensitivity map of ECT, and by setting up a threshold of 55% of the maximum value on this image, a binary image as in **Figure 6.8** is obtained, and in the following ECT process, this image provides the information of dielectric samples and assist ECT to generate a new forward model to help ECT to separate dielectric samples.

In the last column, **MIT-ECT**, the reference measurements are the same as the column of **ECT (water reference)**, but the sensitivity map has been updated with the image from MIT (Figure 6.8). The image quality maintained where the other two fails.

Table 6.14: Reconstruction images of three-phase-system, water background.

Modality / Conductivity	ECT (air reference)	ECT (water reference) r=1e-8	MIT-ECT r=1e-5

0.0003 S/m (DI water)	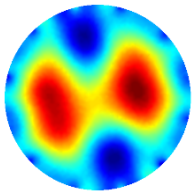	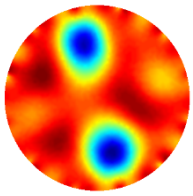	**N/A**
0.0097 S/m	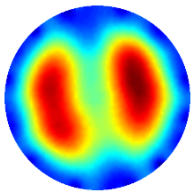	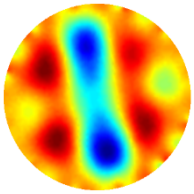	**N/A**
0.0200 S/m	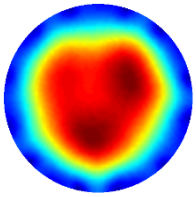	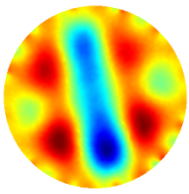	**N/A**
0.0586 S/m (Tap water)	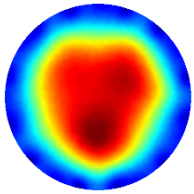	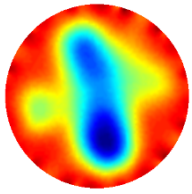	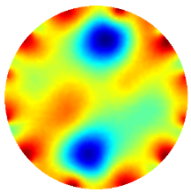
0.1318 S/m	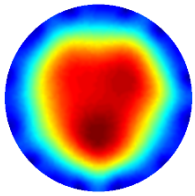	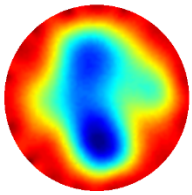	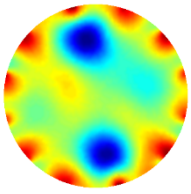
0.1958 S/m	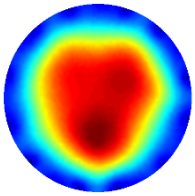	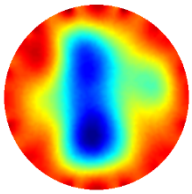	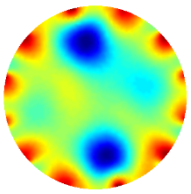
0.3060 S/m	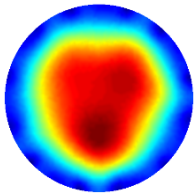	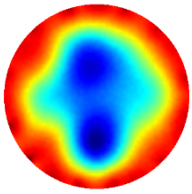	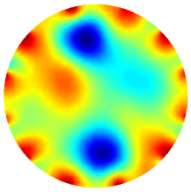
0.5450 S/m	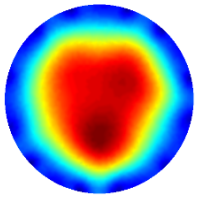	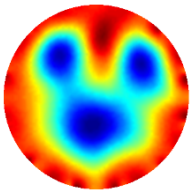	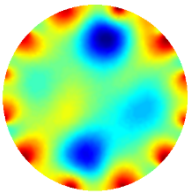

6.6 Discussion

The dual-modality raised in this chapter is a sequential method to image the region containing both conductivity and permittivity contrasts. MIT is sensitive to conductive phase, and as such can be used to distinguish conductivity contrast. The conductivity contrast can be formed either by using a conductive inclusion in a non-conductive background or a non-conductive inclusion in a conductive background. In the context of this study, we considered two representative and also common backgrounds in three-phase flow imaging, *i.e.*, a free space and a water background scenarios in the testing environment. The core-concept of dual modality method is to provide a priori knowledge of the conductivity distribution through the use of MIT, and then to use this information by ECT in attempt to resolve permittivity contrast, hence a three-phase distribution can be established.

Although MIT has a proved capability to identify conductivity contrast [93], the response of MIT system alters according to the change of background conductivity, which suggests for each scenarios mentioned above, different imaging capabilities are observed. Among a large quantity and qualitative experiments conducted, it is showed that in a water background, a conductivity contrast as small as 0.5 S/m can be resolved, which occupies 5.38% of the total imaging region in area. In addition, for an inclusion occupying the same percentage of the imaging region, a conductivity contrast of about 1 S/m is resolved in a free space background. Based on these findings, we anticipate that for both scenarios, for any conductivity contrast lower than these, ECT could be able to operate.

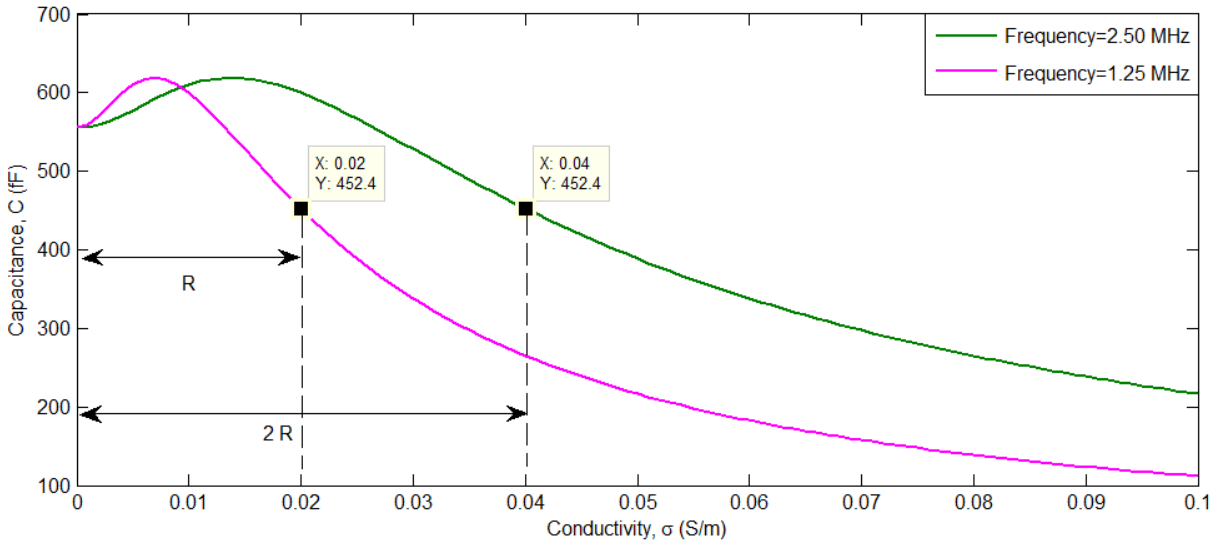

Figure 6.9: Conductivity and frequency impact on the capacitance measurement.

From the conductivity test on the water-background scenario, a conductivity contrast of 0.02 S/m is regarded as a detection limitation of ECT. Under this value, ECT can separate the two low-permittivity phases, *i.e.*, oil and air. From equation **(6.2)**, the complex permittivity is defined as the equation below.

$$\varepsilon_{complex} = \varepsilon(x) + \frac{\sigma(x)}{j\omega} \tag{6.4}$$

Therefore the factor that impacts the imaginary part of this complex value is not only the conductivity but also the signal frequency of the measurement unit. Mathematically, the detection limits can be extended over 0.02 S/m by increasing the frequency. In **Figure 6.9**, the capacitance detection range is doubled when the frequency is doubled, which is generated by the complex-number ECT model. However, due to lack of a higher frequency measurement unit, this extension of limit cannot be proved experimentally. If this mathematical induction works, by increasing signal frequency, the limit of conductivity of ECT can reaches the limit of MIT, and dual modality would work on this scenario as well as the air-background tests.

6.7 Summary

Preliminary results demonstrate the feasibility of three phase flow imaging using a dual modality MIT-ECT combination. The main results in this chapter are focusing on free space background where the effect of conductivity in ECT is minimal and the MIT provides information on location and size of water inclusion, which represents the high permittivity component in ECT, by incorporating this in ECT forward model and the ECT reference measurement, the two low contrast component can be separated. With the case of de-ionized water MIT could not help and further work will be done this dual modality with the conductive backgrounds. Although it requires direct contact, the ERT can image the conductive phase with conductive background. Further development in ECT-MIT combination for conductive background will be subject of further research.

Chapter 7 Complex-value ECT

7.1 Introduction

In the previous study on the conductivity effect on the ECT imaging in **section 6.5.1**, the simulated capacitance in fact are complex values through our complex ECT model.

For electrical metering on flow, the electrical measurements are normally complex value consisting of magnitude and the phase. In [94, 95]capacitive coupling between MIT coils was investigated and highlighted a challenge in the interpretation of MIT data if phase changes are present due to capacitive coupling. In [95] a high frequency phase measurement method adapted from an MIT system was used to show capacitive coupled ECT measurement, referred to as electrical field tomography (EFT). This can be explained through the complex value ECT model presented in this chapter.

In addition to multi-modal techniques, some single modality methods have been proposed: EIT can image complex impedance [96] but as in ERT direct contact with the conductive ccomponent of the imaging medium is needed. [97] shows ECT imaging over a conductive medium , where the electrodes are in direct contact with the medium. This it is essentially the same as EIT and not contactless. In [98], a higher frequency excitation signal is introduced to help ECT to penetrate the conductive water, which is also of high permittivity, and produce more information about the permittivity distribution. In [34-36, 99], a capacitively coupled ERT is used to image the conductivity distribution without contact with the conductive medium, without imaging the permittivity.

A multi-frequency method of contactless measurement and visualisation of both permittivity and conductivity is proposed in this chapter. The aim is to investigate how much more information can be obtained from an ECT device assuming the complex admittance

measurement is possible in a wide range of frequencies. A voltage excitation based admittance measurement is proposed and the receiving electrodes measure resulting complex-valued currents. A complex valued forward model, Jacobian matrix and inversion for ECT are presented in section 7.2. Image reconstruction results are shown in section 7.3, first for single frequency excitation with change of electrical conductivity of the background, and secondly for multi-frequency ECT measurement in a number of imaging scenarios. Summaries of the findings are presented in discussion and results sections.

7.2 Inverse Problem Solver

A more in depth analysis of ECT with conductive background is critical. In this chapter, we study perform a detailed of the relationship between the conductivity/frequency and permittivity and the capacitance measurements based on complex admittance measurements. The complex value forward model has been developed here. To ensure the validity of the complex value forward model, the in-house Matlab based software has been extensively verified against the commercial software COMSOL. First our standard real value ECT forward model was verified against the COMSOL forward model. After exact verification, this new complex value forward model was tested. In both cases our in house ECT software is in full agreement with the COMSOL forward model, which enables us to carry out these simulation studies with full confident.

ECT imaging is generally a time-difference based method, which means that the difference between two measurements at different times is used to calculate the change in permittivity distribution. In equation **(7.1)**, f is the mapping from the change in permittivity to the change in measurements.

$$\Delta C_{complex} = f(\Delta \varepsilon_{complex}) \quad \textbf{(7.1)}$$

Utilizing the finite element method, one can calculate the potential distribution inside the sensor and the capacitances for a given distribution of permittivity/conductivity through building the complex-valued forward model. Furthermore, to obtain the distribution of permittivity/conductivity we need to calculate the sensitivity maps according to the fundamental perturbation theory (the change in capacitance in response to a perturbation of the permittivity or conductivity distribution):

$$J = \frac{\partial C_{complex}}{\partial \mathcal{E}} \; or \; \frac{\partial C_{complex}}{\partial \delta} \tag{7.2}$$

Since the values in equation **(7.2)** are complex, this equation can be rewritten as below

$$J_{complex}\, \Delta\varepsilon_{complex} = \Delta C_{complex} \tag{7.3}$$

$$\begin{cases} J_{r,\varepsilon}\, \Delta\varepsilon_r + J_{r,\sigma}\, \Delta\varepsilon_i = \Delta C_r \\ J_{i,\varepsilon}\, \Delta\varepsilon_r + J_{i,\sigma}\, \Delta\varepsilon_i = \Delta C_i \end{cases} \tag{7.4}$$

where $C_{complex} = \frac{Y}{j\omega}$, Y is the complex admittance; C_r and C_i are the real and imaginary parts of $C_{complex}$; ε_r is the real permittivity value and ε_i is the conductivity divided by angular frequency of signal, $\frac{\sigma(x)}{\omega}$; $[J_{r,\varepsilon}, J_{r,\sigma}]$ and $[J_{i,\varepsilon}, J_{i,\sigma}]$ are the sensitivity maps linked the change in permittivity and conductivity to the real and imaginary part of capacitance change. Equation **(7.4)** can be expressed as the matrix format as:

$$\begin{bmatrix} J_{r,\varepsilon} & J_{r,\sigma} \\ J_{i,\varepsilon} & J_{i,\sigma} \end{bmatrix} \begin{bmatrix} \Delta\varepsilon_r \\ \Delta\varepsilon_i \end{bmatrix} = \begin{bmatrix} \Delta C_r \\ \Delta C_i \end{bmatrix} \tag{7.5}$$

Tikhnov regularization is used to calculate $\Delta\varepsilon_r$ and $\Delta\varepsilon_i$ in the equation above.

$$\begin{bmatrix}\Delta\varepsilon_r\\ \Delta\varepsilon_i\end{bmatrix} = \left(\begin{bmatrix}J_{r,\varepsilon} & J_{r,\sigma}\\ J_{i,\varepsilon} & J_{i,\sigma}\end{bmatrix}^T \begin{bmatrix}J_{r,\varepsilon} & J_{r,\sigma}\\ J_{i,\varepsilon} & J_{i,\sigma}\end{bmatrix} + \alpha I\right)^{-1} \begin{bmatrix}J_{r,\varepsilon} & J_{r,\sigma}\\ J_{i,\varepsilon} & J_{i,\sigma}\end{bmatrix}^T \begin{bmatrix}\Delta C_r\\ \Delta C_i\end{bmatrix} \quad \textbf{(7.6)}$$

Where I is the identity matrix and α is the regulation factor. Through this equation, both the real and imaginary of permittivity can be obtained.

7.3 Results

7.3.1 Simulation of the Capacitance Measurements

As a time-difference imaging method, ECT needs two sets of capacitance: C_b, measurements of background scenario in **Figure 7.1(a)** and C_s, measurement of sample scenario **Figure 7.1(b)**. The relative permittivity of the water is set as $\varepsilon_{water} = 80$, and the conductivity is increased from 0 to 1 S/m. Frequency of the excitation voltage on the sensor is set at $f = 1.25$ MHz. A 12 external-electrode ECT device was considered with 66 independent measurements. An insulator layer of 0.5 cm, *i.e.*, the wall of the sensor, was considered with relative permittivity $\varepsilon_{wall} = 3$. The air sample is a circular region in diameter of 6 cm centred at (0, 3) cm. The simulation is to compute these two sets of capacitances through forward modelling. To obtain an accurate forward model, the finite element method bases on a dense mesh of 6552 elements, shown in **Figure 7.2(a)**.

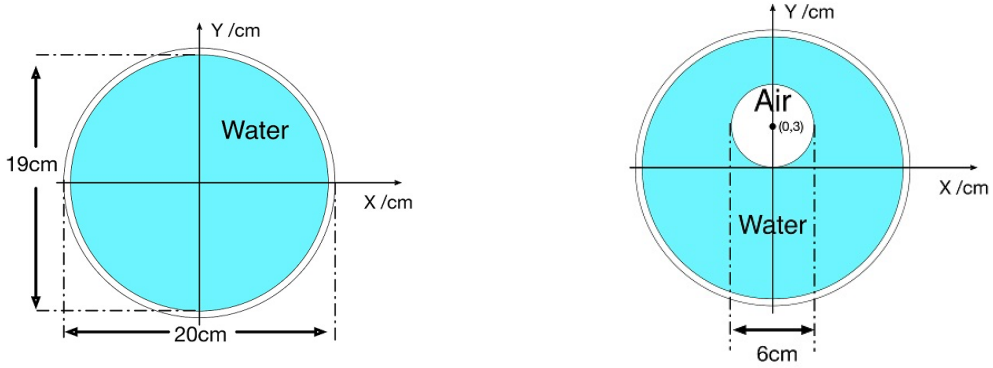

(a)Background: water filled sensor **(b)Sample: Air in water**

Figure 7.1: The dimensions of the ECT tank and the air sample.

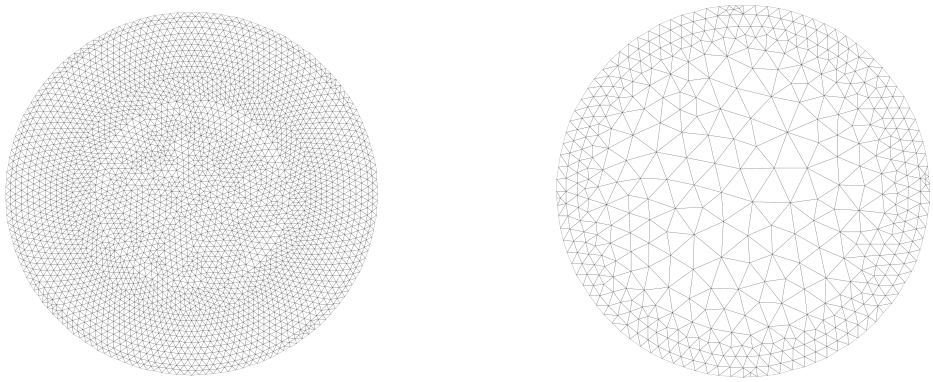

(a) Mesh of 6552 elements **(b) Mesh of 920 elements**

Figure 7.2: The FEM meshes: **(a)** the dense mesh for forward model simulation; **(b)** the coarse mesh for inverse problem solver.

To clearly indicate the trend of the capacitance with increasing conductivity of background, both the real and imaginary parts of background and sample scenarios are plotted separately.

In **Table 7.1**, the 66 inter-capacitance of every two electrodes are plotted. In the row of the background measurement, C_b, the permittivity/conductivity distribution is homogenous within the sensor. Therefore, the capacitance between the pairs of electrodes with equal spacing have the same magnitude and their plots overlap completely, then only six curves are shown, they stand for the capacitance between every neighbouring electrodes, every other electrodes, every three electrode *etc.*, till the opposite electrodes (every six electrodes). In the row of the sample measurement, C_s, the sample of air is added, which makes the electrical property distribution inhomogeneous. As a result, the 6 curves start to split.

To have a better understanding of the trend of complex capacitance, in **Table 7.2**, the 2-norm value of each set of 66 capacitance is plotted to describe the trend of the capacitance change *vs* increasing conductivity.

Table 7.1: Real and imaginary part of every single inter-capacitance of any two electrodes.

Capacitance	Real part	Imaginary part
C_b	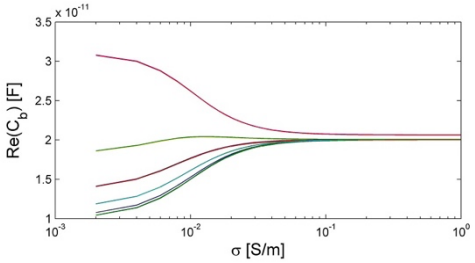	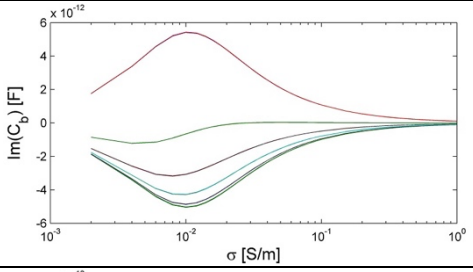
C_s	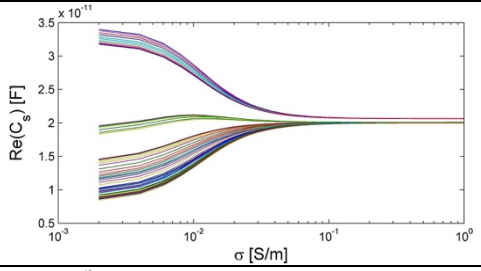	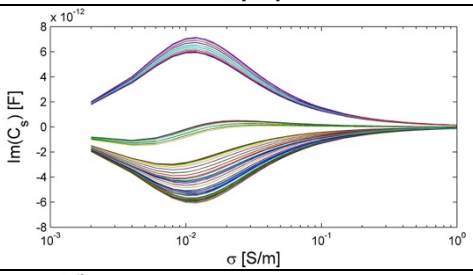
C_s - C_b	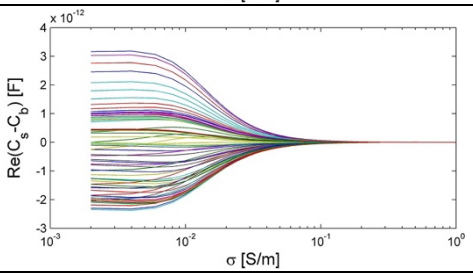	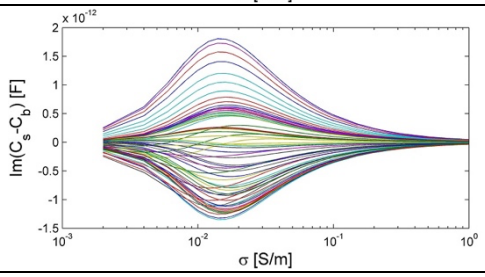

Table 7.2: 2-norm value of real and imaginary part of each set of capacitance over one conductivity.

Capacitance	Real part	Imaginary part
C_b	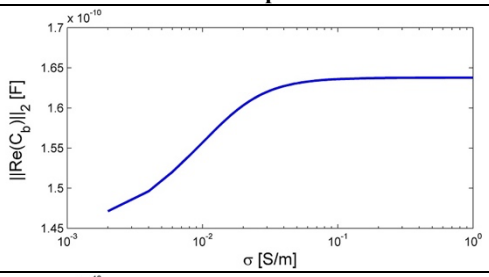	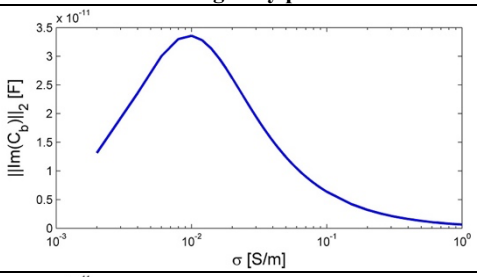
C_s	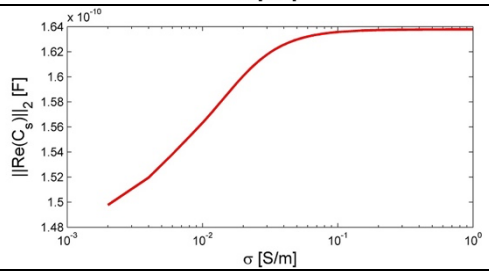	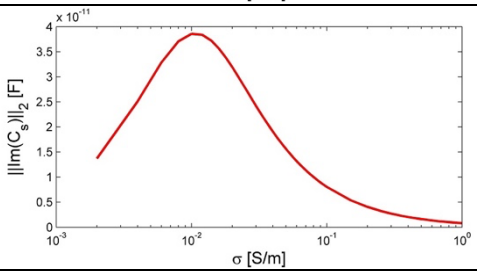

C_s - C_b	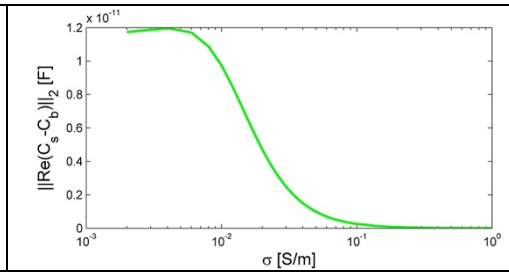	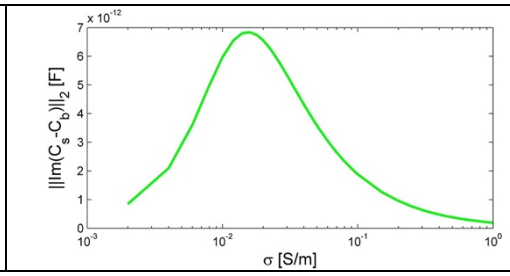

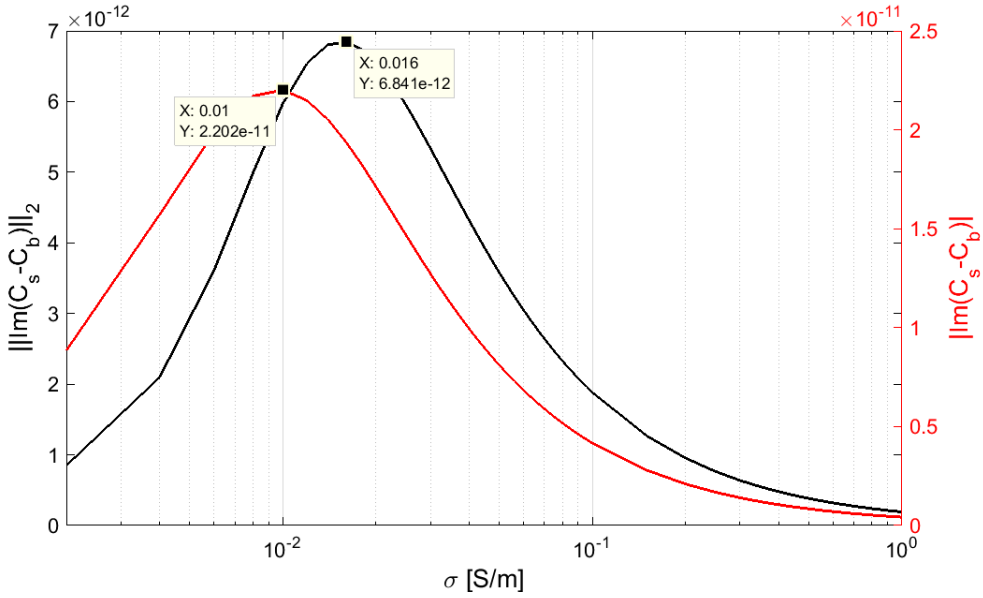

Figure 7.3: Comparison in imaginary part of the capacitance: 2-D simulation and 1-D analysis.

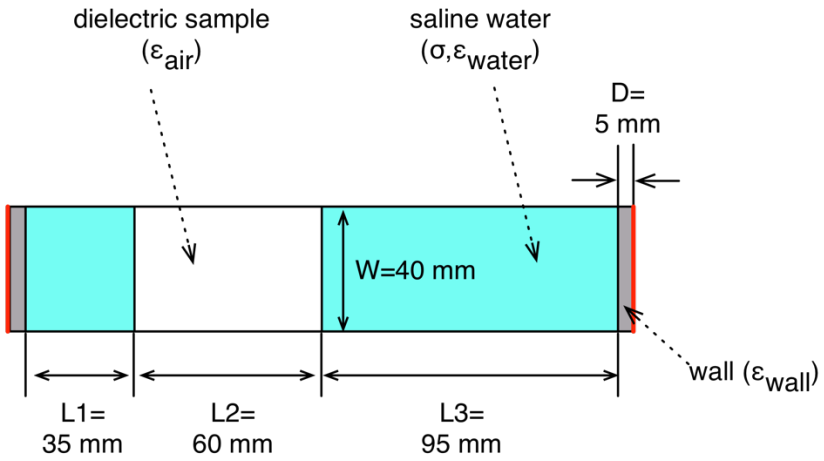

Figure 7.4: 1-dimensional analytical model.

In Table 7.2 for the real part of the difference, the value becomes relatively small when the conductivity is higher than 0.1 S/m. The magnitude of the imaginary part reaches a peak around $\sigma = 0.016$ S/m then declines, as the black line shown in **Figure 7.3**. To have a better understanding of this peak value, we downgrade the 2-D problem to a one dimensional model and use parallel electrodes to calculate the complex capacitance, as shown in **Figure 7.4**.The Size of the electrode (the red line in **Figure 7.4**) is the same as the 2-D model, since it is not a 3-D model, the length of the electrodes is considered as a unit length. By increasing the conductivity σ in equation **(7.7)**, the red line in **Figure 7.3** is obtained.

$$C_s - C_b = \frac{1}{\frac{2}{\varepsilon_{wall}A/D} + \frac{j\omega}{(\sigma + j\omega\varepsilon_{water})A}\left(\frac{1}{L_1} + \frac{1}{L_3}\right) + \frac{2}{\varepsilon_{air}A/L_2}} - \frac{1}{\frac{2}{\varepsilon_{wall}A/D} + \frac{j\omega}{(\sigma + j\omega\varepsilon_{water})A/(L_1 + L_2 + L_3)}} \quad \textbf{(7.7)}$$

Comparing the plots in **Figure 7.3**, the peak value of 1-D model locates at $\sigma = 0.010$ S/m, which is still not the same as $\sigma = 0.016$ S/m in the 2-D simulation, since the complexity of the 2-D geometric distribution makes the this difference. But it shows that both 2-D and 1-D calculation have a similar trend with increasing conductivity of water.

From this simulation, the measurement of complex capacitance tends to decrease, when the conductivity increases. Theoretically, the conductivity makes the added sample “invisible” from measurement reading in both real and imaginary parts.

7.3.2 Complex Permittivity Reconstruction

In the consideration of the experiment speed, the sensing region is divided into a coarse mesh of 920 elements as shown in **Figure 7.2(b)** for faster image reconstruction. The real and imaginary parts of change in complex permittivity distribution are calculated by modified

Tikhonov regularization according to equation **(7.6)** and are plotted separately in **Table 7.4**. The value of the imaginary part of change in complex permittivity, $\Delta\varepsilon_i$, is converted into the format of conductivity by multiplying the angular frequency, $2\pi f$.

To demonstrate the reliability of the reconstruction, we add noise onto the capacitances to simulate the inaccuracy in measurement. The noise added affects both the magnitude and the phase angle of the complex capacitances. For an impedance analyser, the accuracy of the phase angle measurement normally equals 1% of the one on the magnitude, for example the 4990A impedance analyser from Keysight Technologies [17]. The noisy capacitance is set as the equation below:

$$C = |C|\angle\theta \tag{7.8}$$

$$C_{noise} = (1+e)|C|\angle(1+\frac{e}{100})\theta \tag{7.9}$$

$$-E < \text{random}(e) < E \tag{7.10}$$

Where C is the noise-free capacitance between one pair of electrodes, θ is the phase angle of C and e is the noise randomly generated and within the controlled level of E. The noise level is chosen at E=2.

Table 7.3: Image reconstructed from simulated data.

		$\Delta\varepsilon$		$\Delta\sigma$	
	Real distribution	**Noise free**	**2% free**	**Noise free**	**2% free**
One sample	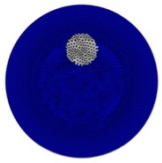	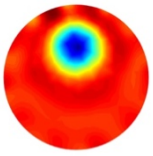	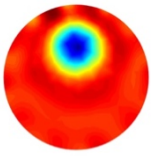	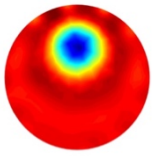	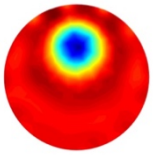

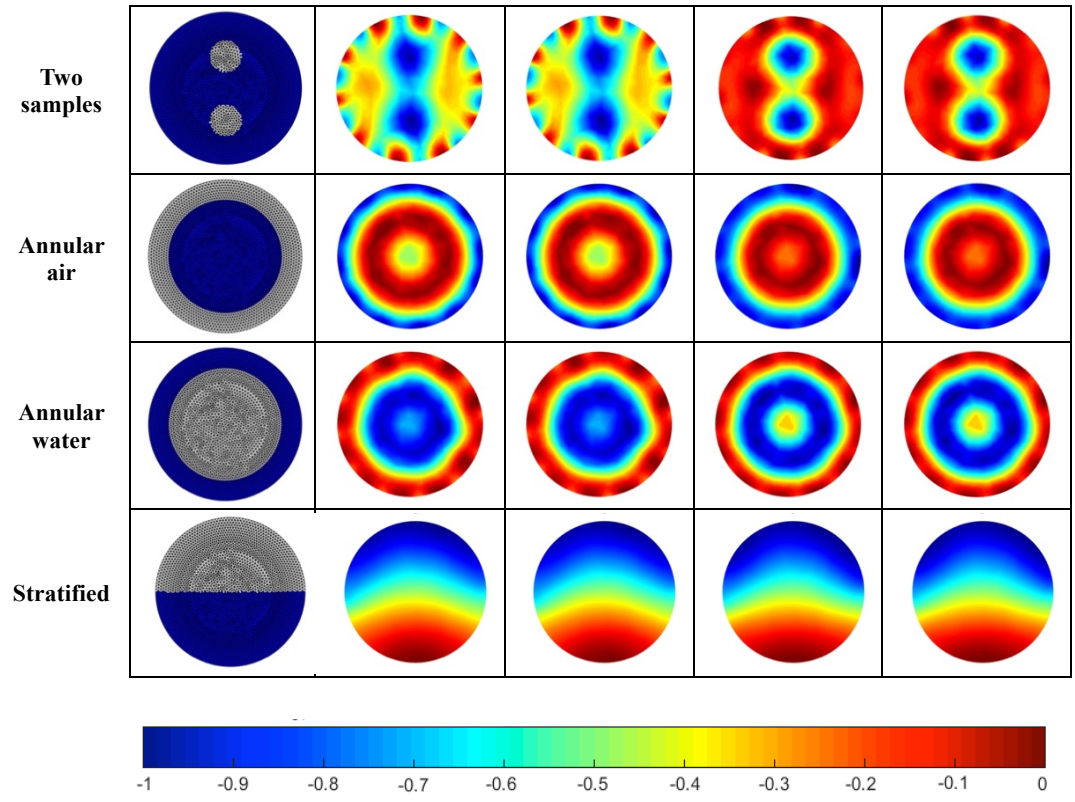

Table 7.3 shows the simulation results of different distributions. In the column of "Real Distribution", the blue region stands for water of relative permittivity of 80 and conductivity of 0.01 S/m; the white region stands for air of relative permittivity of 1 and conductivity of 0. The background data is taken when the sensor is filled with conductive water, so air sample added will result in a drop on permittivity and conductivity distribution on the area of air exists. Thus the reconstructed distribution is in negative value. Except for imaging several different scenarios of fixed conductivity, the same scenario of different conductivity is also worth studying. One circular sample of air adding into conductive water is studied by increasing the conductivity of water. The results are reconstructed in **Table 7.4**

When the capacitance data used is noise-free (the plots in the second and forth column of **Table 7.4),** the reconstruction of either permittivity or conductivity is stable, which distinguishes air (low-permittivity and non-conductivity) from water in the sensor. However when the

conductivity is higher than 0.26 S/m, the permittivity plot starts decaying. When the data contains noise (2%), this causes the increasing instability in reconstructions (the plots in the third and fifth column of **Table 7.4**). With simulations of a pre-set distribution of ε and σ, we can tell the accuracy of the reconstruction directly by the images. However, for a real test of unknown distribution, the unpredictable noise in the measurements result in the inaccuracy of the images. Therefore, a parameter is proposed to measure the stability of calculated distribution of both permittivity and conductivity. The value α in red shown in the tables is the regularisation factor applied to the Tikhonov algorithm.

Set the conductivity of the background at σ, then solve the inverse problem for N times under different random noise within the same level. And we got N sets of the distribution of the electric permittivity change, $\Delta\varepsilon_n$. Then normalise $\Delta\varepsilon_n$ to the range from 0 to1, as shown in equation **(7.11)**:

$$x_n = \frac{\Delta\varepsilon_n - \min(\Delta\varepsilon_n)}{\max(\Delta\varepsilon_n) - \min(\Delta\varepsilon_n)} \qquad for\ n = 1,2,\cdots,N \tag{7.11}$$

Then we calculate the correlation coefficients, $Corr_n$, between $x_n$and x_{n+1}:

$$Corr_n = \frac{\sum_{n=1}^{N}(x_{n+1} - \overline{x_{n+1}})\,((x_n - \overline{x_n}))}{\sqrt{\sum_{n=1}^{N}(x_{n+1} - \overline{x_{n+1}})^2}\sqrt{\sum_{n=1}^{N}(x_n - \overline{x_n})^2}} \tag{7.12}$$

As a result, *(N-1)* correlation coefficients obtained and the mean value of them is the proposed stability parameter. The stability parameters for the simulated data of different conductivity means the reliability of the reconstructed images on the similar real experiments, so we call it the reliability parameter, ***R***.

$$\boldsymbol{R} = \frac{1}{N-1} * \sum_{n=1}^{N-1} Corr_n \tag{7.13}$$

In this experiment, *N* equals 100 to make sure enough random noise for data samplling. We calculate the reliability parameters for the conductivity from 0.001 to 0.6 S/m and the plots of calculated conductivity and permittivity distributionsare shown below.

Table 7.4: Reconstruction of calculated $\Delta\boldsymbol{\varepsilon}$ and $\Delta\boldsymbol{\sigma}$ distribution.

$\boldsymbol{\sigma}$ $[\boldsymbol{S/m}]$	$\Delta\boldsymbol{\varepsilon}$		$\Delta\boldsymbol{\sigma}$	
	Noise-free	**2% Noise**	**Noise-free**	**2% Noise**
0.001 α=1e-7	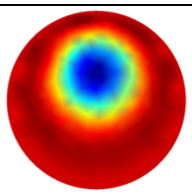	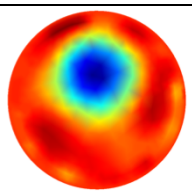	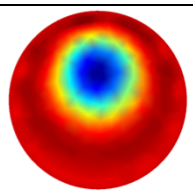	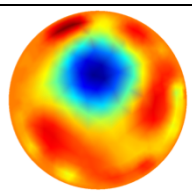
0.01 α=1e-8	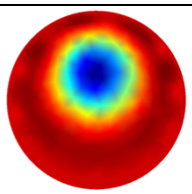	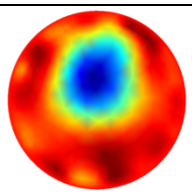	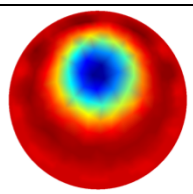	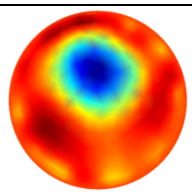
0.015 α=5e-9	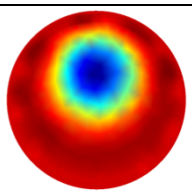	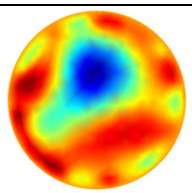	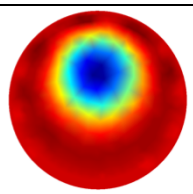	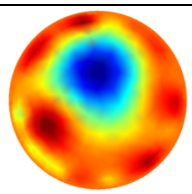
0.02 α=5e-9	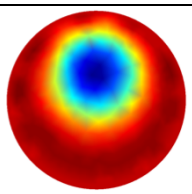	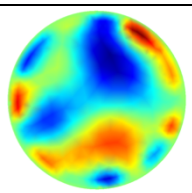	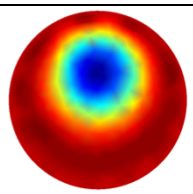	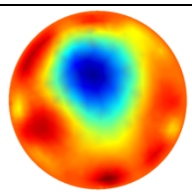
0.1 α=1e-11	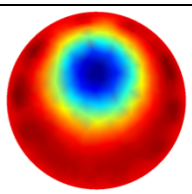	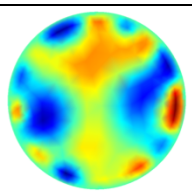	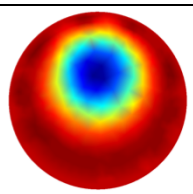	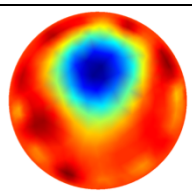
0.26 α=2.5e-13	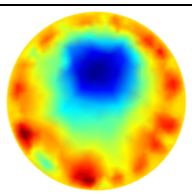	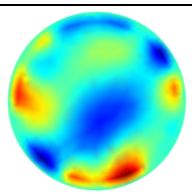	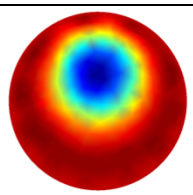	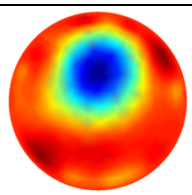
0.6 α=1e-14	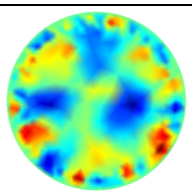	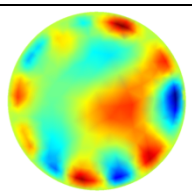	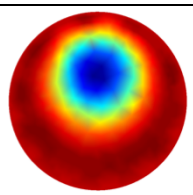	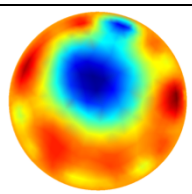

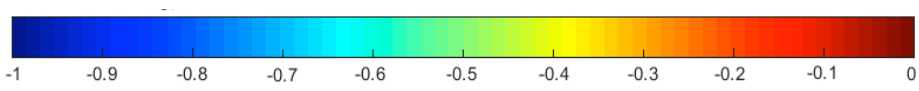

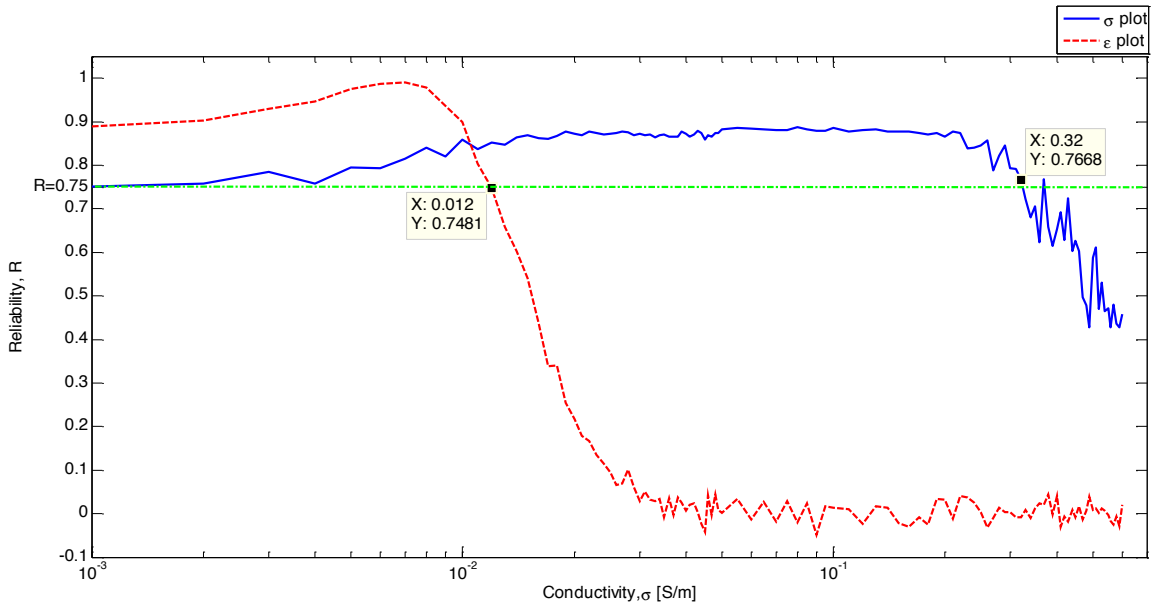

Figure 7.5: Reliability values of the noisy data for increasing conductivity.

From our experimental observation in this case, we found that above the green dashed line, *i.e.*, ***R>0.75***, the reconstructed images are relatively reliable. In other words, in the case of this simulation scenario, when the conductivity is higher than 0.32 S/m and 0.012 S/m, the σ plot and ε plot are not reliable respectively.

The results indicate that simultaneous reconstruction of both the permittivity and conductivity is feasible but limited to a small range of conductivity. In this section, the simulation model incorporates an air inclusion in the water background. This means that the admittance data simulated between the electrodes contains information about the changes in both permittivity and conductivity due to the air. Two factors changing increases the complexity of verifying this simultaneous reconstruction. To verify this method, two hypothetical inclusions are proposed in the next section, and the effect of the frequency is investigated.

7.3.3 Multiple Frequency ECT

In this section the effect of changes in permittivity or conductivity distribution on the

simultaneous reconstruction is investigated. A sample with high conductivity but low permittivity (like "conductive gas") is used to test the permittivity (ε) plot and a sample of low conductivity but high permittivity (such as deionised water) is used to test the conductivity (σ) plot. The size and location information is presented in **Table 7.5.** The simulations is done with 5 frequencies: 125 kHz, 625 kHz, 1.25 MHz, 6.25 MHz and 12.5 MHz. The background measurement is taken when the sensing region is filled with only sample 3.

Table 7.5: Three cases of different electric property and positions for simulations.

No. of the sample	Radius and location	Relative permittivity	Conductivity (S/m)
1 (Grey)	R=3 cm centered at(0,4) cm	1	0.05
2 (Green)	R=3 cm centered at(0,-4) cm	80	0
3 (Blue)	R=9.5 cm centered at (0,0) cm	80	0.05

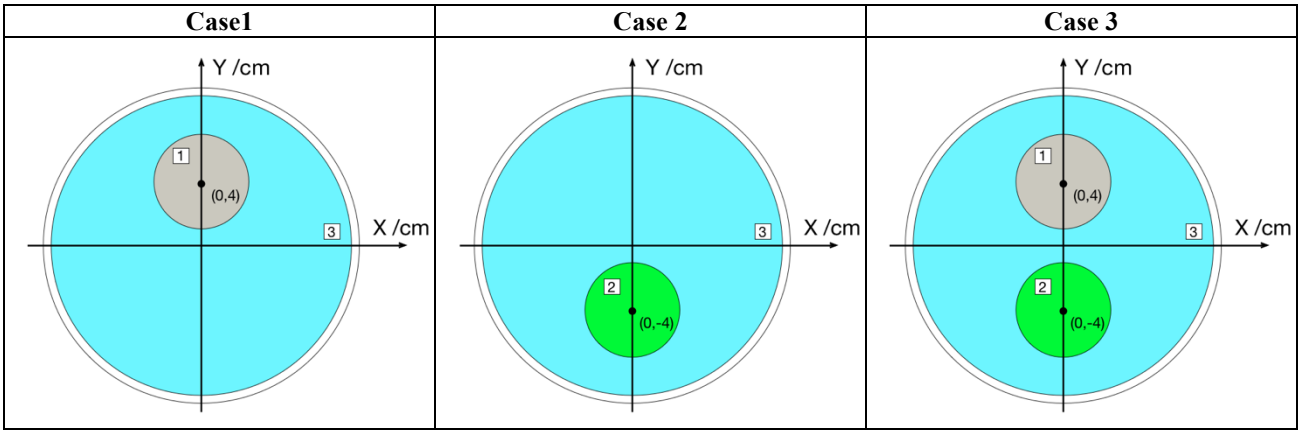

Under different frequency, the measurement of capacitance is influenced by adding sample to different extent. The 2-norm values of the noise-free capacitance difference, ΔC, are listed in **Table 7.6** and the ones with 2% noise, ΔC_e, are in **Table 7.7**.

Table 7.6: The change in noise-free capacitance difference in Case 1, 2& 3.

Case	ΔC	125 kHz	625 kHz	1.25 MHz	6.25 MHz	12.5 MHz
1	$\|Re(\Delta C)\|_2$	1.933e-15	4.751e-14	1.804e-13	1.109e-12	1.295e-12
	$\|Im(\Delta C)\|_2$	5.744e-17	7.091e-15	5.457e-14	2.807e-12	6.096e-12
2	$\|Re(\Delta C)\|_2$	2.262e-14	5.454e-13	1.960e-12	7.256e-12	3.255e-12
	$\|Im(\Delta C)\|_2$	4.183e-13	1.984e-12	3.376e-12	2.264e-12	3.970e-12
3	$\|Re(\Delta C)\|_2$	2.133e-14	5.144e-13	1.851e-12	7.159e-12	4.261e-12
	$\|Im(\Delta C)\|_2$	4.183e-13	1.991e-12	3.429e-12	2.464e-12	5.739e-12

Table 7.7: The change in capacitance difference with 2% noise in Case 1, 2& 3.

Case	ΔC_e	125 kHz	625 kHz	1.25 MHz	6.25 MHz	12.5 MHz
1	$\|Re(\Delta C_e)\|_2$	2.455e-12	2.678e-12	2.603e-12	2.656e-12	2.797e-12
	$\|Im(\Delta C_e)\|_2$	1.969e-14	1.010e-13	2.015e-13	2.884e-12	6.116e-12
2	$\|Re(\Delta C_e)\|_2$	2.560e-12	2.517e-12	3.177e-12	7.446e-12	4.080e-12
	$\|Im(\Delta C_e)\|_2$	4.100e-13	1.994e-12	3.384e-12	2.313e-12	3.879e-12
3	$\|Re(\Delta C_e)\|_2$	2.584e-12	2.487e-12	3.126e-12	7.477e-12	4.827e-12
	$\|Im(\Delta C_e)\|_2$	4.170e-13	2.001e-12	3.418e-12	2.515e-12	5.724e-12

The 2% of noise will have an impact on the capacitance difference shown above. And it can be quantified by the change rate between the numbers in **Table 7.6** and **Table 7.7**. The change rate is defined as equation below and filled in **Table 7.8**.

$$Change\ rate = \frac{\|\boldsymbol{Re}(\Delta \boldsymbol{C_e})\|_2}{\|\boldsymbol{Re}(\Delta \boldsymbol{C})\|_2} - 1 \quad or \quad \frac{\|\boldsymbol{Im}(\Delta \boldsymbol{C_e})\|_2}{\|\boldsymbol{Im}(\Delta \boldsymbol{C})\|_2} - 1 \tag{7.14}$$

These CRs demonstrate that in all the three cases the real part of the capacitance difference is affected by the noises significantly in lower frequency as well. The imaginary part is immune to this 2% noise for all frequencies for **Case 2** and **3**.

Table 7.8: The change rate between ΔC and ΔC_e .

Case	Change rate	125 kHz	625 kHz	1.25 MHz	6.25 MHz	12.5 MHz
1	Real	1269.046	55.367	13.429	1.395	1.160
	Imaginary	341.792	13.243	2.692	0.027	0.003
2	Real	112.174	3.614	0.621	0.026	0.253
	Imaginary	-0.019	0.005	0.002	0.021	-0.023
3	Real	120.143	3.834	0.689	0.044	0.133
	Imaginary	-0.003	0.005	-0.003	0.021	-0.003

Then in **Table 7.9** and **Table 7.10**, the reconstructions of $\Delta\varepsilon$ and $\Delta\sigma$ change based on the capacitance with or without noise are shown.

Table 7.9: Reconstruction of $\Delta\boldsymbol{\varepsilon}$ and $\Delta\boldsymbol{\sigma}$ distribution in Case 1&2.

Frequency	Noise level	Case 1		Case 2	
		$\Delta\varepsilon$	$\Delta\sigma$	$\Delta\varepsilon$	$\Delta\sigma$
125kHz α=1e-13	0	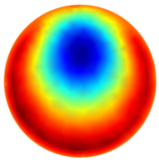	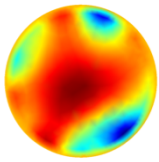	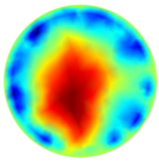	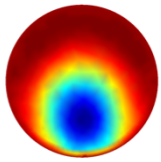
	2%	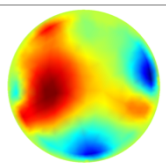	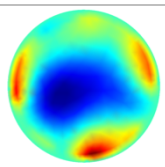	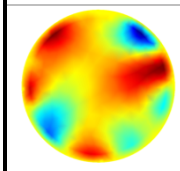	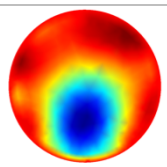
625kHz α=1e-11	0	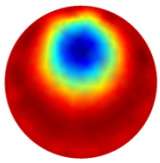	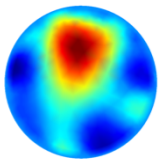	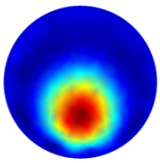	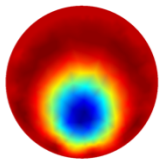
	2%	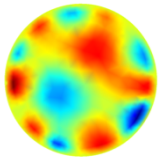	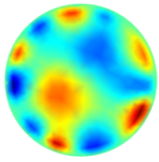	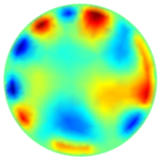	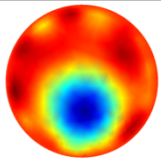
1.25MHz α=1e-10	0	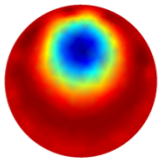	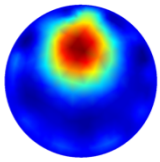	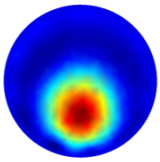	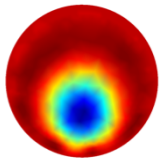

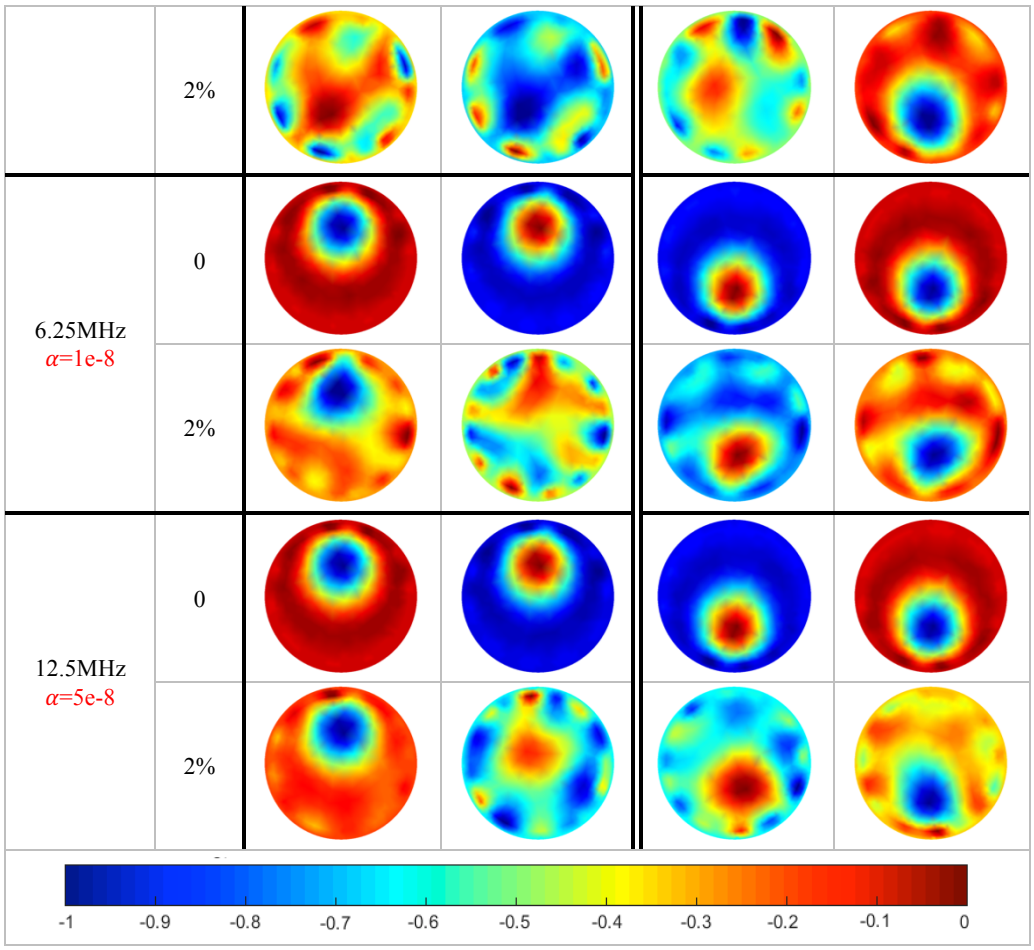

Table 7.10: Reconstruction of $\Delta\boldsymbol{\varepsilon}$ and $\Delta\boldsymbol{\sigma}$ distribution in Case 3.

Frequency	Noise level	Case 3	
		$\Delta\varepsilon$	$\Delta\sigma$
125kHz α=1e-13	0	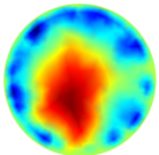	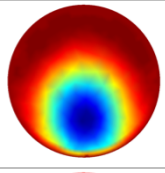
	2%	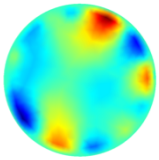	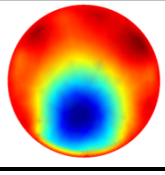

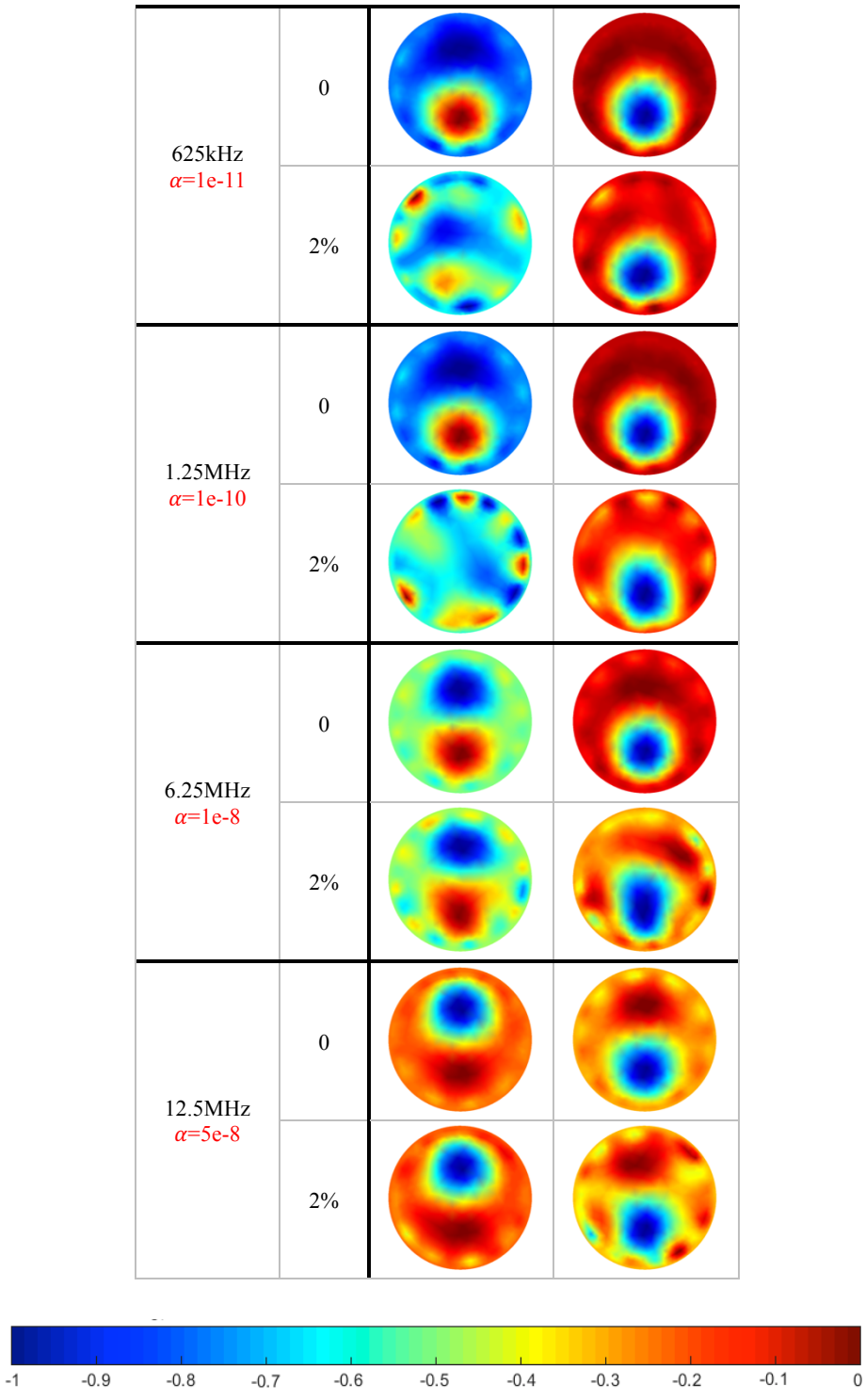

To give a clear view of the reliability of the images in tables above, the same evaluation process as in **section 7.3.2** was conducted on the data with 2% noise. The reliability parameter of different frequencies and cases is plotted below:

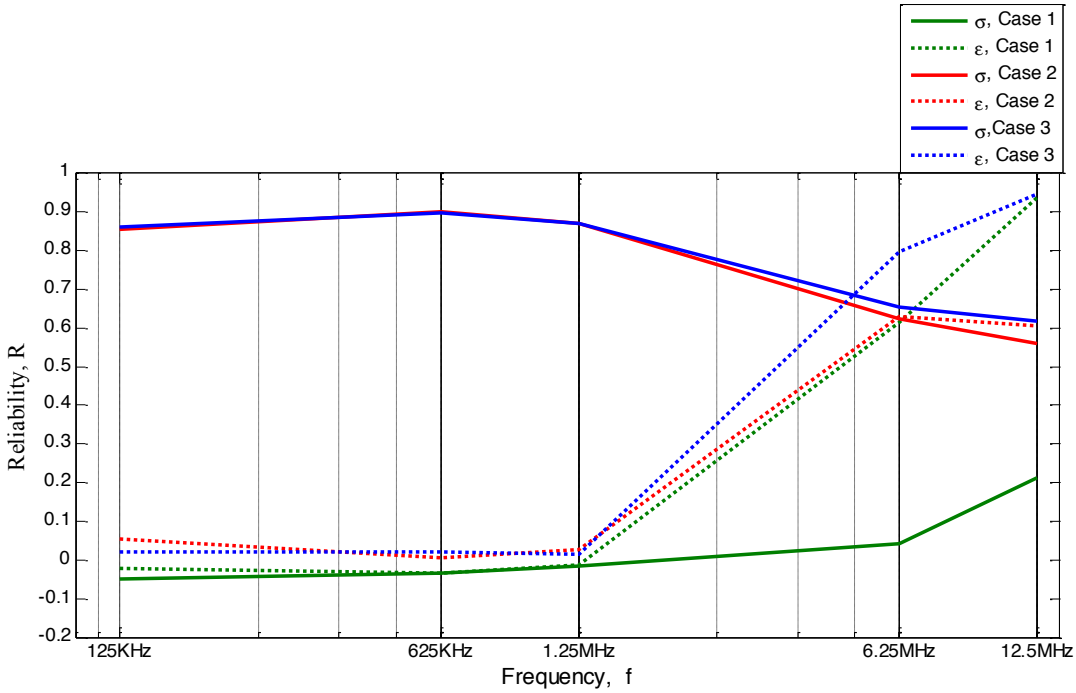

Figure 7.6: Reliability plot of the noisy data along the increasing conductivity.

1. In Case 1, the noise-free data illustrates that the permittivity change, which results from replacing conductive water with a "conductive gas", has more impact on the real part of ΔC in the frequency range from 125 kHz to 1.25 MHz, *i.e.*, the real part is much bigger than the imaginary part. Within this range the noise makes a significant impact on both real and imaginary parts of ΔC, as shown by the images in **Table 7.9**. When the frequency keeps increasing, the imaginary part of the ΔC becomes bigger than the real part, and the effect of noise on the value of ΔC becomes minor. As shown in the rows 6.25 MHz and 12.5 MHz in **Table 7.9**, the ε images of the noisy data performs similarly to the noise-free data, and the reliability of it increases (the green dot line in **Figure 7.6**).

2. In Case 2, as frequency grows, influence on the real part of ΔC from the noise trends smaller, while the imaginary part of ΔC is immune to the noise, and has only a very small perturbation. From the reconstruction in **Table 7.9**, a reliable performance over

noise and different frequencies of the σ images is observed (the red solid line in **Figure 7.6**).

3. In Case 3, both permittivity and conductivity affects the measurements simultaneously. However the measurements of the frequencies from 125 kHz to 1.25 MHz are close to the value in Case 2, which means the conductivity difference from the deionised water to conductive water has a dominant impact, therefore the images in **Table 7.10** is similar to Case 2 at the same frequency range. Thereafter, at higher frequency the impact on capacitance from "conductive gas" increases and in **Table 7.10**, the blue phantom on images of both ε and σ illustrates the two inclusions respectively. And the reliability of the images are plotted as the blue lines in **Figure 7.6.**

In **Table 7.6** and **Table 7.8**, a small capacitance difference of noise free scenario in low frequency is significantly influenced by the added noise. Therefore in Case 1, where a small capacitance difference is only caused by a regional permittivity change, the reconstruction failed due to the added noise. While in Case 2, the impacts from the regional conductivity change is much bigger and not sensitive to the noise. For the same size of these two samples taking over the place of the background water, the magnitude of the local impacts can only be the same when the change in permittivity equals the change in conductivity divided by angular frequency:

$$|\varepsilon_{water} - \varepsilon_{air}| = \left|\frac{\sigma_{water}}{j2\pi f}\right| \quad \textbf{(7.15)}$$

Where ε_{water} and σ_{water} are the permittivity and conductivity of water, and ε_{air} is the permittivity of air. In our cases, as the setting in **Table 7.5**, only when frequency equals $f = \left|\frac{\sigma_{water}}{2\pi(\varepsilon_{water}-\varepsilon_{air})}\right| = 11.377$ MHz, the two type of samples have the same magnitude of influence. This explains that in case 3, when frequency higher than the 6.25 MHz, the permittivity image starts working, since the weighting of permittivity change's impact is not negligible compared

with conductivity change.

7.4 Discussion

Traditional ECT has been used as a method to imaging permittivity distribution of dielectric samples for a long time. This chapter presented an in depth evaluation of using the contactless method to monitor the electric property change, and to reconstruct the permittivity and conductivity in one go. Both real and imaginary parts of the complex permittivity are investigated through modelling. In **section 7.3.3**, the hypothetical samples provides a preliminary understanding about the influence on measurements and reconstruction from permittivity change and conductivity change. In the real experiment, such as oil/gas/water phase flow imaging, the low permittivity components are always low conductivity. Theoretically, the simultaneous reconstruction provides more information of both permittivity and conductivity distribution from sets of admittances (complex value) data. From the simulations of the conductive water background, we found that the conductivity plots have very reliable performance in showing the low-conductive inclusion, even though the image of permittivity fails. This means that the conductivity plots can be used as prior information for iterative algorithms.

The conductivity and frequency jointly affects the measurement of the complex capacitance as expressed in equation **(6.1)** applying higher excitation frequency to ECT measurement would help to generate better images of both ε and σ distribution. Particularly in the case of the non-conductive inclusions staying in the conductive background, increasing frequency of excitation signal has the same result of decreasing the conductivity of the background. More experimental work on different frequencies will be carried out based on an impedance analyser, instead of a purely capacitance measurement unit. Therefore, the feasibility of the multi-frequency complex admittance ECT method will be tested in future.

7.5 Summary

By using capacitance measurements between the electrodes at the periphery of flow pipe, ECT visualises the permittivity distribution of multi-phase flow. This is useful for cases such as gas-oil or solid-gas flows, where the inclusions are normally dielectric or low conductivity. For flows with a conductive medium, such as conductive water, the conductivity will affect the capacitance measurements. The forward model and inverse solver of conventional ECT also cannot analyse this effect correctly from the measurements, so ECT fails to work. If the measurements for ECT are the admittance including both capacitance and resistance, with a complex-value sensitivity map, a simultaneous reconstruction of permittivity and conductivity is possible as proposed in this chapter. A realistic noise model presented to evaluate how each of the admittance components in a variety of frequencies contributes to imaging permittivity and conductivity. The results of this chapter demonstrate a much greater potential for ECT as a far more versatile imaging device than it is currently perceived as. The contactless nature of ECT makes this device potentially suitable for many new application areas such as medical imaging and process monitoring with a conductive medium. Unifying modelling work presented here will allow a number of classes of electrical imaging systems to be analysed.

Chapter 8 **Conclusions**

8.1 Summary

This thesis presents new ideas and methods which allows further expansion of using ECT for materials with electrical conductivity. A combined MIT-ECT may be needed for imaging of a mixture of grounded metals and dielectric samples. A floating metallic sample is reconstructed as a high-permittivity illusion in a capacitance measurement. This proves a feasibility of imaging metal by ECT at the same time inability to distinguish metallic samples from dielectric ones. A grounded metallic sample fails ECT imaging, prior information about the location of metallic samples are in need to improve the forward model of ECT to account for grounded conductors, therefore MIT is introduced to find the metallic components which can then improve the ECT reconstruction. For multiphase flow imaging, the ability of ECT imaging dielectric materials has been widely studied. While the existence of conductive water is inevitable in monitoring oil-gas-water flow. If the conductive water takes only a small part of the sensing region, where gas is still the background medium, and then the conductivity of the water would not affect the capacitance measurement and reconstructed images. However, if the conductive water fills the sensor as a background medium to hold the rest phase flows of gas and oil, its conductivity substantially reduces the ability of ECT to calculate the permittivity distribution. In the case of gas background, MIT does not significantly improve the quality of ECT reconstruction of oil and water flows, but helps to distinguish the conductive water from the oil. In the case of conductive water background, an initial image of conductivity distribution from MIT strongly increase the capability of ECT imaging the gas and oil inclusions inside the water. As such, the dual-modality of MIT-ECT solves more problems where the single ECT cannot. However from the analysis on capacitance measurements of increasing conductivity, the frequency of measuring signal seems to provide a potential solution for ECT imaging in conductive medium. To explore the impact of conductivity, frequency and permittivity of the material in ECT imaging, ECCT is proposed to solve this problems as a single modality.

Currently this idea is still based on the simulation only, however the promising results shows ability of ECCT to image the distribution of not only the permittivity but also the conductivity.

8.2 Limitations and Future Works

8.2.1 Distinguish Metallic Samples from Dielectric Sample

In **Chapter 4**, ECT images both metallic samples and the dielectric samples, however it is not capable to distinguish one from the other. But this can be solved by using MIT, which is not sensitive to the dielectric component. A similar process is shown in **Chapter 5** or **section 6.4**.

8.2.2 The Reference Measurement of ECT in the Dual-Modality

Normally, the conductive material always has an impact on in electrical capacitance measurement. For metallic samples, the equal-potential on the surface distorts the electric fields and increases the difficulty of ECT imaging. For conductive water in multiphase flow, besides the conductivity of the water, its inherently high permittivity makes the problem of imaging inside of water more non-linear. The idea of applying MIT to both high and low conductive scenarios is that MIT can sense and visualize the region of conductive material, whose unique information can allow for a better reference for ECT reconstruction process. But in this thesis, only the sensitivity map has been modified based on the MIT information, if the background measurement can also be compensated by this prior information through ECT forward simulation, this could make the inverse problem more linearized. In **Chapter 5** & **Chapter 6**, when MIT is introduced as a sequential dual modality, the process speed slows down for both measuring and post-process of MIT results. For the water-background scenario, even with the help of MIT, ECT still cannot distinguish the gas from oil, which are of low permittivity compared with water.

8.2.3 Complex-value Measurement of ECT

All ECT devices are working based on capacitance measurement in single frequency excitation mode. This hardware limits our exploration of using the contactless electrodes to imaging both conductivity and permittivity distribution. Future development of the measurement unit would help us to prove the concept of the simultaneous reconstructions for conductivity and permittivity. The information from complex ECT could be hybrid by itself: the clear conductivity reconstruction in low excitation frequency can help improve the permittivity distribution in forward model; and similarly, permittivity reconstruction would help conductivity imaging in high-frequency signal.

8.3 Future plans

This work aimed to propose contactless electrical tomography that is applicable to meet a wider range of monitoring requirements. The hybrid MIT-ECT provides solutions for the grounded metal and potentially for the conductive-water-background multiphase monitoring, where the current hardware of MIT in our laboratory limits the ability of imaging the very low conductivity ($\sigma < 0.5$ S/m). As a single modality, ECT using complex-value measurement is able to simultaneously image both the conductivity and permittivity distribution that is demonstrated with appropriately modelled noisy synthetic data. The hope is that this work extensively improve understanding of the ECT system under dielectric and conductive mixture materials. This will open up a number of new application area for ECT imaging. Future work can focus on metal flow imaging using ECT, dynamical three phase flow imaging using contactless hybrid imaging presented here.

Publications

Journal papers:

Zhang, M., & Soleimani, M. (2016). Simultaneous reconstruction of permittivity and conductivity using multi-frequency admittance measurement in electrical capacitance tomography. *Measurement Science and Technology*, *27*(2), 025405.

Zhang, M., Ma, L., & Soleimani, M. (2015). Dual modality ECT–MIT multi-phase flow imaging. *Flow Measurement and Instrumentation*, *46*, 240-254.

Al Hosani, E., Zhang, M., & Soleimani, M. (2015). A Limited Region Electrical Capacitance Tomography for Detection of Deposits in Pipelines. *Sensors Journal, IEEE*, *15*(11), 6089-6099.

Zhang, M., & Soleimani, M. (2015). Imaging floating metals and dielectric objects using electrical capacitance tomography. *Measurement*, *74*, 143-149.

Zhang, M., Ma, L., & Soleimani, M. (2014). Magnetic induction tomography guided electrical capacitance tomography imaging with grounded conductors. *Measurement*, *53*, 171-181.

Conference or Workshop Items

Zhang, M., & Soleimani, M. (2015). Complex admittance measurements in ECT for conductivity and permittivity imaging: a theoretical evaluation. In *7th International Symposium on Process Tomography (ISPT 7)*. *2015-09-01 - 2015-09-03*, Dresden, Germany.

Zhang, M., Ma, L., & Soleimani, M. (2014). Dual modality ECT-MIT three-phase flow imaging. In *5th International Workshop on Process Tomography (IWPT-5), 2014-09-16 - 2014-09-18*. Jeju, Korea.

Zhang, M., & Soleimani, M. (2014). Planar array electrical capacitance tomography for high permittivity flow imaging. In *5th International Workshop on Process Tomography (IWPT-5), 2014-09-16 - 2014-09-18*. Jeju, Korea.

Zhang, M., Ma, L., Ye, Z., Yang, C. L., Wei, H. Y., Banasiak, R., & Soleimani, M. (2013). Near subsurface 3D imaging using planar array: EIT, ECT, MIT. In *7th World Congress in Industrial Process Tomography (WCIPT7)*. *2013-09-02 - 2013-09-05*, Krakow, Poland

Reference

1. Cheney, M., D. Isaacson, and J.C. Newell, *Electrical impedance tomography.* SIAM review, 1999. **41**(1): p. 85-101.

2. Brown, B., *Electrical impedance tomography (EIT): a review.* Journal of medical engineering & technology, 2003. **27**(3): p. 97-108.

3. Brown, B.H., *Medical impedance tomography and process impedance tomography: a brief review.* Measurement Science and Technology, 2001. **12**(8): p. 991.

4. Adler, A., M.B. Amato, J.H. Arnold, R. Bayford, M. Bodenstein, S.H. Böhm, B.H. Brown, I. Frerichs, O. Stenqvist, and N. Weiler, *Whither lung EIT: Where are we, where do we want to go and what do we need to get there?* Physiological measurement, 2012. **33**(5): p. 679.

5. Saulnier, G.J., R.S. Blue, J.C. Newell, D. Isaacson, and P.M. Edic, *Electrical impedance tomography.* Signal Processing Magazine, IEEE, 2001. **18**(6): p. 31-43.

6. Zou, Y. and Z. Guo, *A review of electrical impedance techniques for breast cancer detection.* Medical Engineering & Physics, 2003. **25**(2): p. 79-90.

7. Adler, A., R. Amyot, R. Guardo, J. Bates, and Y. Berthiaume, *Monitoring changes in lung air and liquid volumes with electrical impedance tomography.* Journal of Applied Physiology, 1997. **83**(5): p. 1762-1767.

8. Adler, A., R. Guardo, and Y. Berthiaume, *Impedance imaging of lung ventilation: do we need to account for chest expansion?* Biomedical Engineering, IEEE Transactions on, 1996. **43**(4): p. 414-420.

9. Wang, M., *Seeing a new dimension—The past decade's developments On electrical impedance tomography.* Progress in natural science, 2005. **15**(S1): p. 1-13.

10. George, D.L., J.R. Torczynski, K.A. Shollenberger, T.J. O'Hern, and S.L. Ceccio, *Validation of electrical-impedance tomography for measurements of material distribution in two-phase flows.* International Journal of Multiphase Flow, 2000. **26**(4): p. 549-581.

11. Heikkinen, L., J. Kourunen, T. Savolainen, P. Vauhkonen, J. Kaipio, and M. Vauhkonen, *Real time three-dimensional electrical impedance tomography applied in*

multiphase flow imaging. Measurement Science and Technology, 2006. **17**(8): p. 2083.

12. Jia, J., M. Wang, Y. Faraj, and Q. Wang, *Online conductivity calibration methods for EIT gas/oil in water flow measurement.* Flow Measurement and Instrumentation, 2015.

13. Griffiths, H., *Magnetic induction tomography.* Measurement Science & Technology, 2001. **12**(8): p. 1126-1131.

14. Griffiths, H., W. Stewart, and W. Gough, *Magnetic induction tomography: a measuring system for biological tissues.* Annals Of The New York Academy Of Sciences, 1999. **873**(1): p. 335-345.

15. Jin, G., J. Sun, M. Qin, Q. Tang, L. Xu, X. Ning, J. Xu, X. Pu, and M. Chen, *A new method for detecting cerebral hemorrhage in rabbits by magnetic inductive phase shift.* Biosensors and Bioelectronics, 2014. **52**: p. 374-378.

16. Merwa, R., K. Hollaus, O. Biró, and H. Scharfetter, *Detection of brain oedema using magnetic induction tomography: a feasibility study of the likely sensitivity and detectability.* Physiological measurement, 2004. **25**(1): p. 347.

17. Scharfetter, H., P. Riu, M. Populo, and J. Rosell, *Sensitivity maps for low-contrast perturbations within conducting background in magnetic induction tomography.* Physiological measurement, 2002. **23**(1): p. 195.

18. Ma, L., H.-Y. Wei, and M. Soleimani, *Pipelines inspection using magnetic induction tomography based on a narrowband pass filtering method.* Progress In Electromagnetics Research M, 2012. **23**: p. 65-78.

19. Wei, H.-Y. and M. Soleimani, *Two-phase low conductivity flow imaging using magnetic induction tomography.* Progress In Electromagnetics Research, 2012. **131**: p. 99-115.

20. Ma, L., A. Hunt, and M. Soleimani, *Experimental evaluation of conductive flow imaging using magnetic induction tomography.* International Journal of Multiphase Flow, 2015. **72**(0): p. 198-209.

21. Evangelidis, M., L. Ma, and M. Soleimani, *High definition electrical capacitance tomography for pipeline inspection.* Progress In Electromagnetics Research, 2013. **141**.

22. Xie, C.G., S.M. Huang, B.S. Hoyle, R. Thorn, C. Lenn, D. Snowden, and M.S. Beck, *Electrical capacitance tomography for flow imaging: system model for development*

of image reconstruction algorithms and design of primary sensors. Iee Proceedings-G Circuits Devices and Systems, 1992. **139**(1): p. 89-98.

23. Huang, Z., B. Wang, and H. Li, *Application of electrical capacitance tomography to the void fraction measurement of two-phase flow.* Instrumentation and Measurement, IEEE Transactions on, 2003. **52**(1): p. 7-12.

24. Tapp, H., A. Peyton, E. Kemsley, and R. Wilson, *Chemical engineering applications of electrical process tomography.* Sensors and Actuators B: Chemical, 2003. **92**(1): p. 17-24.

25. Jing, L., S. Liu, L. Zhihong, and S. Meng, *An image reconstruction algorithm based on the extended Tikhonov regularization method for electrical capacitance tomography.* Measurement, 2009. **42**(3): p. 368-376.

26. Liu, S., W. Yang, H. Wang, F. Jiang, and Y. Su, *Investigation of square fluidized beds using capacitance tomography: preliminary results.* Measurement Science and Technology, 2001. **12**(8): p. 1120.

27. Warsito, W. and L.S. Fan, *3D-ECT velocimetry for flow structure quantification of gas-liquid-solid fluidized beds.* Canadian Journal of Chemical Engineering, 2003. **81**(3-4): p. 875-884.

28. Warsito, W. and L.S. Fan, *Dynamics of spiral bubble plume motion in the entrance region of bubble columns and three-phase fluidized beds using 3D ECT.* Chemical Engineering Science, 2005. **60**(22): p. 6073-6084.

29. Huang, S., R. Green, A. Plaskowski, and M. Beck, *Conductivity effects on capacitance measurements of two-component fluids using the charge transfer method.* Journal of Physics E: Scientific Instruments, 1988. **21**(6): p. 539.

30. Stott, A., R. Green, and K. Seraji, *Comparison of the use of internal and external electrodes for the measurement of the capacitance and conductance of fluids in pipes.* Journal of Physics E: Scientific Instruments, 1985. **18**(7): p. 587.

31. Jeanmeure, L.F.C., T. Dyakowski, W.B.J. Zimmerman, and W. Clark, *Direct flow-pattern identification using electrical capacitance tomography.* Experimental Thermal and Fluid Science, 2002. **26**(6-7): p. 763-773.

32. Jaworski, A.J. and T. Dyakowski, *Application of electrical capacitance tomography for measurement of gas-solids flow characteristics in a pneumatic conveying system.* Measurement Science & Technology, 2001. **12**(8): p. 1109-1119.

33. Ismail, I., J.C. Gamio, S.F.A. Bukhari, and W.Q. Yang, *Tomography for multi-phase flow measurement in the oil industry.* Flow Measurement and Instrumentation, 2005. **16**(2-3): p. 145-155.

34. Wang, B., Y. Hu, H. Ji, Z. Huang, and H. Li, *A Novel Electrical Resistance Tomography System Based on C4D Technique.* Instrumentation and Measurement, IEEE Transactions on, 2013. **62**(5): p. 1017-1024.

35. Wang, B., W. Tan, Z. Huang, H. Ji, and H. Li, *Image reconstruction algorithm for capacitively coupled electrical resistance tomography.* Flow Measurement and Instrumentation, 2014. **40**(0): p. 216-222.

36. Wang, B., W. Zhang, Z. Huang, H. Ji, and H. Li, *Modeling and optimal design of sensor for capacitively coupled electrical resistance tomography system.* Flow Measurement and Instrumentation, 2013. **31**(0): p. 3-9.

37. Li, Y., W. Yang, C.-g. Xie, S. Huang, Z. Wu, D. Tsamakis, and C. Lenn, *Gas/oil/water flow measurement by electrical capacitance tomography.* Measurement Science & Technology, 2013. **24**(7).

38. Huang, S., C. Xie, M. Beck, R. Thorn, and D. Snowden, *Design of sensor electronics for electrical capacitance tomography.* IEE Proceedings G (Circuits, Devices and Systems), 1992. **139**(1): p. 83-88.

39. Huang, S., A. Plaskowski, C. Xie, and M. Beck, *Capacitance-based tomographic flow imaging system.* Electronics letters, 1988. **24**(7): p. 418-419.

40. Yang, W. and T. York, *New AC-based capacitance tomography system.* IEE Proceedings-Science, Measurement and Technology, 1999. **146**(1): p. 47-53.

41. Yang, W.Q., *Hardware design of electrical capacitance tomography systems.* Measurement Science & Technology, 1996. **7**(3).

42. Yang, W.Q., M.S. Beck, and M. Byars, *Electrical capacitance tomography- from design to applications.* Measurement & Control, 1995. **28**(9): p. 261-266.

43. Yang, W.Q., D.M. Spink, J.C. Gamio, and M.S. Beck, *Sensitivity distributions of capacitance tomography sensors with parallel field excitation.* Measurement Science & Technology, 1997. **8**(5): p. 562-569.

44. Cui, Z., H. Wang, Z. Chen, Y. Xu, and W. Yang, *A high-performance digital system for electrical capacitance tomography.* Measurement Science and Technology, 2011. **22**(5): p. 055503.

45. Byars, M. *Process Tomography Ltd Electrical Capacitance Tomography System Type PTL300E*. 9 Dec 2014 [cited 2015 5 May]; Available from: http://www.tomography.com/pdf/ptl300E.pdf.

46. Ma, L., *Magnetic Induction Tomography for Non-destructive Evaluation and Process Tomography*. 2014, University of Bath.

47. Wei, H.-Y. and M. Soleimani, *Theoretical and experimental evaluation of rotational magnetic induction tomography.* Instrumentation and Measurement, IEEE Transactions on, 2012. **61**(12): p. 3324-3331.

48. Wei, H.-Y. and M. Soleimani, *A Magnetic Induction Tomography System for Prospective Industrial Processing Applications.* Chinese Journal of Chemical Engineering, 2012. **20**(2): p. 406-410.

49. Wei, H.-Y. and M. Soleimani, *Hardware and software design for a National Instrument-based magnetic induction tomography system for prospective biomedical applications.* Physiological measurement, 2012. **33**(5): p. 863.

50. Kip, A.F., *Fundamentals of Electricity and Magnetism*. 1969: McGraw-Hill Education.

51. Banasiak, R., R. Wajman, and M. Soleimani, *An efficient nodal Jacobian method for 3D electrical capacitance tomography image reconstruction.* Insight-Non-Destructive Testing and Condition Monitoring, 2009. **51**(1): p. 36-38.

52. Vauhkonen, P.J., M. Vauhkonen, T. Savolainen, and J.P. Kaipio, *Three-dimensional electrical impedance tomography based on the complete electrode model.* Ieee Transactions on Biomedical Engineering, 1999. **46**(9): p. 1150-1160.

53. Rimpilainen, V., S. Poutiainen, L.M. Heikkinen, T. Savolainen, M. Vauhkonen, and J. Ketolainen, *Electrical capacitance tomography as a monitoring tool for high-shear mixing and granulation.* Chemical Engineering Science, 2011. **66**(18): p. 4090-4100.

54. Yang, W.Q., *Calibration of capacitance tomography systems: A new method for setting system measurement range.* Measurement Science & Technology, 1996. **7**(6): p. 863-867.

55. Soleimani, M. and W.R.B. Lionheart, *Nonlinear image reconstruction for electrical capacitance tomography using experimental data.* Measurement Science & Technology, 2005. **16**(10): p. 1987-1996.

56. Dyck, D.N., D.A. Lowther, and E.M. Freeman, *A method of computing the sensitivity of electromagnetic quantities to changes in materials and sources.* Ieee Transactions on Magnetics, 1994. **30**(5): p. 3415-3418.

57. Somersalo, E., D. Isaacson, and M. Cheney, *A linearized inverse boundary-value problem for maxwell equations.* Journal of Computational and Applied Mathematics, 1992. **42**(1): p. 123-136.

58. Bíró, O., *Edge element formulations of eddy current problems.* Computer methods in applied mechanics and engineering, 1999. **169**(3): p. 391-405.

59. Biro, O. and K. Preis, *An edge finite element eddy current formulation using a reduced magnetic and a current vector potential.* Magnetics, IEEE Transactions on, 2000. **36**(5): p. 3128-3130.

60. Yang, W.Q., D.M. Spink, T.A. York, and H. McCann, *An image-reconstruction algorithm based on Landweber's iteration method for electrical-capacitance tomography.* Measurement Science & Technology, 1999. **10**(11): p. 1065-1069.

61. Vauhkonen, M., *Electrical impedance tomography and prior information.* 1997.

62. Peng, L.H., H. Merkus, and B. Scarlett, *Using regularization methods for image reconstruction of electrical capacitance tomography.* Particle & Particle Systems Characterization, 2000. **17**(3): p. 96-104.

63. Jinchuang, Z., F. Wenli, L. Taoshen, and W. Shi, *An image reconstruction algorithm based on a revised regularization method for electrical capacitance tomography.* Measurement Science and Technology, 2002. **13**(4): p. 638.

64. Zhao, J.C., W.L. Fu, T.S. Li, and S. Wang, *An image reconstruction algorithm based on a revised regularization method for electrical capacitance tomography.* Measurement Science & Technology, 2002. **13**(4): p. 638-640.

65. Soleimani, M., P.K. Yalavarthy, and H. Dehghani, *Helmholtz-Type Regularization Method for Permittivity Reconstruction Using Experimental Phantom Data of Electrical Capacitance Tomography.* Ieee Transactions on Instrumentation and Measurement, 2010. **59**(1): p. 78-83.

66. Yang, W.Q. and L.H. Peng, *Image reconstruction algorithms for electrical capacitance tomography.* Measurement Science & Technology, 2003. **14**(1): p. R1-R13.

67. Liu, S., L. Fu, and W. Yang, *Optimization of an iterative image reconstruction algorithm for electrical capacitance tomography.* Measurement Science and Technology, 1999. **10**(7): p. L37.

68. Yorkey, T.J., J.G. Webster, and W.J. Tompkins, *Comparing reconstruction algorithms for electrical impedance tomography.* Biomedical Engineering, IEEE Transactions on, 1987(11): p. 843-852.

69. Ortega, J.M. and W.C. Rheinboldt, *Iterative solution of nonlinear equations in several variables*. 2000: Siam.

70. Soleimani, M., M. Vauhkonen, W. Yang, A. Peyton, B.S. Kim, and X. Ma, *Dynamic imaging in electrical capacitance tomography and electromagnetic induction tomography using a Kalman filter.* Measurement Science & Technology, 2007. **18**(11): p. 3287-3294.

71. Zhang, M., L. Ma, and M. Soleimani, *Magnetic induction tomography guided electrical capacitance tomography imaging with grounded conductors.* Measurement, 2014. **53**(0): p. 171-181.

72. Dixiang, C., H. Xiaohui, and Y. Wuqiang, *Design of a security screening system with a capacitance sensor matrix operating in single-electrode mode.* Measurement Science and Technology, 2011. **22**(11): p. 114026.

73. Hyenkyun, W., K. Sungwhan, S. Jin Keun, L. William, and W. Eung Je, *A direct tracking method for a grounded conductor inside a pipeline from capacitance measurements.* Inverse Problems, 2006. **22**(2): p. 481.

74. de Fornel, P., J.M. Lourtioz, D. Pagnoux, H. Benisty, V. Berger, J.M. Gerard, D. Maystre, and A. Tchelnokov, *Photonic Crystals: Towards Nanoscale Photonic Devices*. 2008: Springer.

75. Huang, S.M., R.G. Green, A.B. Plaskowski, and M.S. Beck, *Conductivity effects on capacitance measurements of two-component fluids using the charge transfer method.* Journal of Physics E: Scientific Instruments, 1988. **21**(6): p. 539.

76. Gonzalez-Nakazawa, A., J.C. Gamio, and W. Yang, *Transient processes and noise in a tomography system: An analytical case study.* Sensors Journal, IEEE, 2005. **5**(2): p. 321-329.

77. Heikkinen, L., M. Vauhkonen, T. Savolainen, and J. Kaipio, *Modelling of internal structures and electrodes in electrical process tomography.* Measurement Science and Technology, 2001. **12**(8): p. 1012.

78. Qiu, C., B. Hoyle, and F. Podd, *Engineering and application of a dual-modality process tomography system.* Flow Measurement and Instrumentation, 2007. **18**(5): p. 247-254.

79. Wang, B., Z. Huang, and H. Li. *Design of high-speed ECT and ERT system*. in *Journal of Physics: Conference Series*. 2009. IOP Publishing.

80. Nowakowski, J., E. Hammer, D. Sankowski, D. Styra, R.a. Wajman, R. Banasiak, and A. Romanowski, *Multimodality measurement data fusion in image reconstruction for multiphase flow measurements.* Automatyka/Akademia Górniczo-Hutnicza im. Stanisława Staszica w Krakowie, 2010. **14**: p. 731-739.

81. Yin, X., D.A. Hutchins, G.G. Diamond, and P. Purnell, *Non-destructive evaluation of concrete using a capacitive imaging technique: Preliminary modelling and experiments.* Cement and Concrete Research, 2010. **40**(12): p. 1734-1743.

82. Adler, A., J.H. Arnold, R. Bayford, A. Borsic, B. Brown, P. Dixon, T.J. Faes, I. Frerichs, H. Gagnon, and Y. Gärber, *GREIT: a unified approach to 2D linear EIT reconstruction of lung images.* Physiological measurement, 2009. **30**(6): p. S35.

83. Yang, W.Q., *Modelling of capacitance tomography sensors.* Iee Proceedings-Science Measurement and Technology, 1997. **144**(5): p. 203-208.

84. Korjenevsky, A., V. Cherepenin, and S. Sapetsky, *Magnetic induction tomography: experimental realization.* Physiological Measurement, 2000. **21**(1): p. 89-94.

85. Thorn, R., G.A. Johansen, and B.T. Hjertaker, *Three-phase flow measurement in the petroleum industry.* Measurement Science and Technology, 2013. **24**(1): p. 012003.

86. Deng, X. and W. Yang, *Fusion research of electrical tomography with other sensors for two-phase flow measurement.* Measurement Science Review, 2012. **12**(2): p. 62-67.

87. Chaminda, P., Y. Ru, V. Sondre, C.M. Morten, and M. Saba, *Electrical capacitance tomography (ECT) and gamma radiation meter for comparison with and validation and tuning of computational fluid dynamics (CFD) modeling of multiphase flow.* Measurement Science and Technology, 2014. **25**(7): p. 075404.

88. Hjertaker, B.T., R. Maad, and G.A. Johansen, *Dual-mode capacitance and gamma-ray tomography using the Landweber reconstruction algorithm.* Measurement Science and Technology, 2011. **22**(10): p. 104002.

89. Nowakowski, J., E. Hammer, D. Sankowski, D. Styra, R.a. Wajman, R. Banasiak, and A. Romanowski, *New concept of ECT/ERT/GRT tomography for multiphase flow*

measurements. Automatyka/Akademia Górniczo-Hutnicza im. Stanisława Staszica w Krakowie, 2010. **14**: p. 741-747.

90. Hjertaker, B.T., S.-A. Tjugum, E. Hammer, and G.A. Johansen, *Multimodality tomography for multiphase hydrocarbon flow measurements.* Sensors Journal, IEEE, 2005. **5**(2): p. 153-160.

91. Soleimani, M., *Computational aspects of low frequency electrical and electromagnetic tomography: A review study.* International Journal of Numerical Analysis and Modeling, 2008. **5**(3): p. 407-440.

92. Peyman, A., C. Gabriel, and E.H. Grant, *Complex permittivity of sodium chloride solutions at microwave frequencies.* Bioelectromagnetics, 2007. **28**(4): p. 264-274.

93. Watson, S., R.J. Williams, W. Gough, and H. Griffiths, *A magnetic induction tomography system for samples with conductivities below 10 S m −1.* Measurement Science and Technology, 2008. **19**(4): p. 045501.

94. Griffiths, H., W. Gough, S. Watson, and R. Williams, *Residual capacitive coupling and the measurement of permittivity in magnetic induction tomography.* Physiological measurement, 2007. **28**(7): p. S301.

95. Korjenevsky, A. and T. Tuykin, *Experimental demonstration of electric field tomography.* Physiological measurement, 2010. **31**(8): p. S127.

96. Yang, C.L., A. Mohammed, Y. Mohamadou, T.I. Oh, and M. Soleimani, *Complex conductivity reconstruction in multiple frequency electrical impedance tomography for fabric-based pressure sensor.* Sensor Review, 2015. **35**(1): p. 85-97.

97. Liao, A. and Q. Zhou, *Application of ECT and relative change ratio of capacitances in probing anomalous objects in water.* Flow Measurement and Instrumentation, 2015. **45**(0): p. 7-17.

98. Li, Y. and M. Soleimani, *Imaging conductive materials with high frequency electrical capacitance tomography.* Measurement, 2013. **46**(9): p. 3355-3361.

99. Newill, P., D. Karadaglić, F. Podd, B. Grieve, and T. York, *Electrical impedance imaging of water distribution in the root zone.* Measurement Science and Technology, 2014. **25**(5): p. 055110.